NORTHWESTERN UNIVERSITY

Quantum Dot Infrared Photodetectors Operating at Room Temperature: Modeling, Experiments and Analysis

A DISSERTATION

SUBMITTED TO THE GRADUATE SCHOOL IN PARTIAL FULFILLMENT OF THE REQUIREMENTS

for the degree

DOCTOR OF PHILOSOPHY

Field of Electrical and Computer Engineering

By

Ho-Chul Lim

EVANSTON, ILLINOIS

December 2007

Abstract

Quantum Dot Infrared Photodetectors Operating at Room Temperature: Modeling, Experiments and Analysis

Ho-Chul Lim

The important application for the infrared photodetectors is mainly thermal imaging by focal plane arrays (FPAs) for military and commercial purposes. So far, most mid-wavelength infrared (MWIR) and long-wavelength infrared (LWIR) FPAs are based either on HgCdTe (MCT) or quantum well infrared photodetectors (QWIPs). Even though those technologies are well developed and have the state of the art performances, they have intrinsic weaknesses which are difficult to be overcome. Many researchers have searched new infrared photodetectors. One of the promising technologies is quantum dot infrared photodetectors (QDIP) based on self-assembled quantum dots. Self-assembled quantum dot is the very nanotechnology which is based on the novel physical phenomena and shows the possibility of promising new device concept.

The objective of this work is to develop high performance and high operation temperature quantum dot infrared photodetectors based on high quality self assembled

(Ga)InAs quantum dots on InP and GaAs substrates grown by low-pressure metal organic chemical vapor deposition.

At first, the unique physical properties of quantum dots will be discussed in terms of density of state, discrete energy levels and finally novel property “phonon bottleneck”. And the method of fabrication of quantum dots and device structures and test procedures will be reviewed.

At second, in order to understand the device design rules, the modeling of the important parameters will be developed. The parameters which will be discussed are energy levels, oscillator strengths of the transitions, responsivity, dark current, noise, gain and detectivity. The detailed analyses on one of InGaAs QD/InGaP/GaAs MWIR-QDIPs will be given to elucidate the physical understandings and give the direction for the improvement of the devices.

At third, MWIR-QDIP structures based on the InAs/InP systems will be discussed. Especially the focus on the growth of the InAs quantum dots on various matrix layers on InP substrate will be made. At 77 K, the photoresponse showed the peak wavelength around 5 μm. The highest detectivity was 2.0×10^{9} cm·$Hz^{1/2}$ /W.

Finally, the hybridization of the InAs quantum dot and the $In_{0.53}Ga_{0.47}As$ quantum well was realized in InAs/InGaAs/InAlAs/InP system. The resulting device structure which is named as quantum dot-quantum well infrared photodetector (QDWIP) had high-performance and high operation temperature up to room temperature. The peak detection wavelength was observed at 4.1 μm. The peak responsivity and the specific detectivity at 120 K were 667 mA/W and 2.8×10^{11} cm$Hz^{1/2}$/W respectively. Low dark current density

and a high quantum efficiency of 35 % were obtained in this device. We will discuss how the quantum efficiency can be improved through quantum dot engineering.

Acknowledgments

I would like to thank my advisor Professor Razeghi for her guide, support and enthusiasm for this work. Without her, this work would be impossible. I would also like to thank all the members of my committee for their willingness to participate in my Ph. D. final exam: Professor Alan Sahakian, Professor Matthew Grayson, Professor Hooman Mohseni and Professor Lawrence Henschen.

I thank all the present and former members of the Center for Quantum Devices who have been very helpful and improving my understanding and knowledge of the research.

I would like to thank my wife Jihyun and my daughter Chloe and my families for their love, support and faith in me.

Finally I thank God for being with me all the time.

Table of Contents

List of Figures

List of Tables

1 Introduction

The important application for the infrared photodetectors is mainly thermal imaging by focal plane arrays (FPAs) for military and commercial purposes. Many researchers have focused on the MCT (mercury cadmium telluride), QWIP (quantum infrared photodetector) or type II superlattice (SL) photodetector in order to develop the infrared photodetector with better performances. In case of QWIP and type II SL, the quantum wells and superlattices act as photosensitive region which absorb the infrared light and generate the photocurrent.

But one-dimensional confinement of carriers in quantum wells and the superlattices, with the resultant discretization of the energy structure, is not only approach to infrared photodetector based on the quantum structure. Carrier confinement in all three dimensions can be also used. This can be realized via semiconductor nanostructures known as quantum dots. The beginning of the interest in quantum dot research can be traced back to a suggestion by Arakawa and Sakaki[1] in 1982 that the performance of semiconductor laser could be improved by reducing the dimensionality of the active regions of these devices. Initial efforts at reducing the dimensionality of the active regions were focused on using ultrafine lithography coupled with wet or dry etching to form three dimensional structures. It was soon realized, however, that this approach introduced defects that greatly limited the performance of such quantum dots. In 1993, the first epitaxial growth of defect-free quantum dot nanostructures was achieved by using Molecular Beam Epitaxy (MBE)[2]. Most of the practical quantum dot structures today are grown by either MBE or MOCVD (Metalorganic Chemical Vapor Deposition).

Under certain growth conditions, when the thickness of the thin film with the larger lattice constant than that of the substrate exceeds a certain critical thickness, the compressive strain within the film is relieved by the formation of coherent island. These islands are quantum dots. Coherent quantum dots are generally formed only when the growth proceeds in what is known as Stranski-Krastanow growth mode.

Quantum dot infrared photodetectors (QDIPs), whose active region is composed of quantum dots layers separated by the barriers, show the potential advantages over current technology such as quantum well infrared photodetectors. First the intersubband absorption can be allowed at normal incidence. In QWIPs, the transitions, which are caused by the light polarized perpendicular to the growth direction, are normally allowed due to absorption selection rules. The selection rules in QDIPs are different and normal incidence absorption has been observed. Second thermal generation of electrons is significantly reduced due to the energy quantization in all three dimensions. Generation of LO phonons are prohibited because it is difficult for the energy level spacing of a quantum dot to be equal to that of the phonon. This prohibition does not apply to the quantum wells, since the levels are quantized only in the growth direction and a continuum exists in the other two directions. This can lower the dark current and higher photoconductive gain which leads to higher detectivity.

Currently, the realization of quantum dot infrared photodetectors with the advantages mentioned above has not still come true before our research. But QDIPs which will be discussed shows the possibility to achieve such advantages. It is important to understand the device mechanism by theoretical modeling and analysis of the devices which give us a direction to improvement of the devices.

2 Overview of Infrared Radiation and Semiconductor Detectors

2.1 Introduction to Infrared Radiation

Infrared (IR) radiation is a form of radiated electromagnetic energy, obeying the same laws as those for visible light, radio waves, and x-rays. In fact, its only fundamental difference from those forms of electromagnetic radiation is its wavelength. This is shown in the chart of the electromagnetic spectrum in Figure 2.1. The borderlines between visible, infrared, far-infrared, and millimeter waves are not absolute.

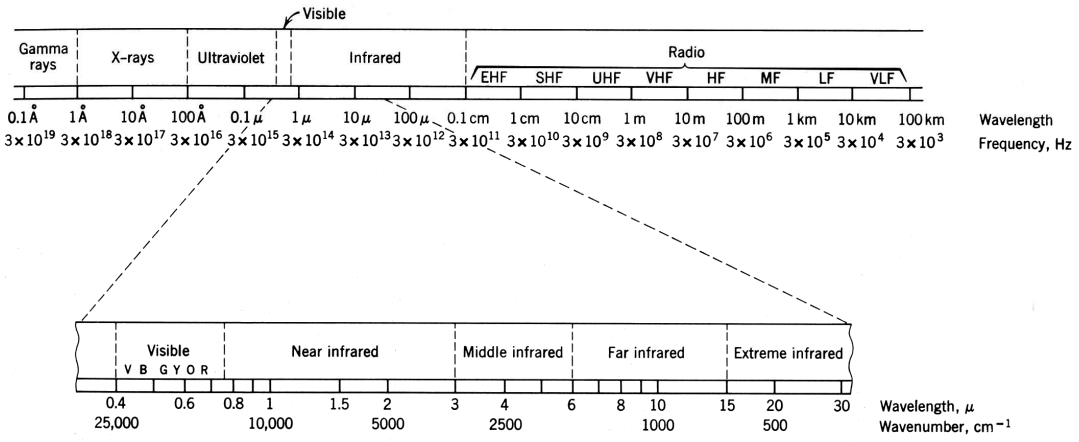

Figure 2.1. Electromagnetic spectrum, shown below is an expanded view of the infrared wavelength region[3].

These areas of the spectrum have been segregated primarily for convenience in discussions. But most IR detectors in our discussion take advantage of two atmospheric windows which are spectral regions that transmit well; the 3 to 5 μm window, and the 8 to 12 μm window. The 3 to 5 μm window is called as Mid-Wavelength Infrared (MWIR). On the other hand the 8 to 12 μm

window is called as Long-Wavelength Infrared (LWIR). Thus we could include the 3 to 12 μm region as the primary IR region.

Heat is transferred in three ways: radiated (electromagnetic radiation), conducted (as though a hot piece of metal), and convected (through warm air circulating in a room). Radiation transfer is important because IR detectors will measure the radiant transfer of heat or photons. Warm objects radiate more IR power than do cooler ones, but all objects give off some power in the infrared. Room-temperature objects and even ice cubes emit some IR. Blackbody radiation versus temperature plot is shown in Figure 2.2. It is this relationship between temperature and the distribution of emission wavelength that was first accurately described empirically by Planck in 1900. The consequence of Planck's Law was that energy is not continuous, but rather has discrete values or quanta. This initiated the development of quantum physics.

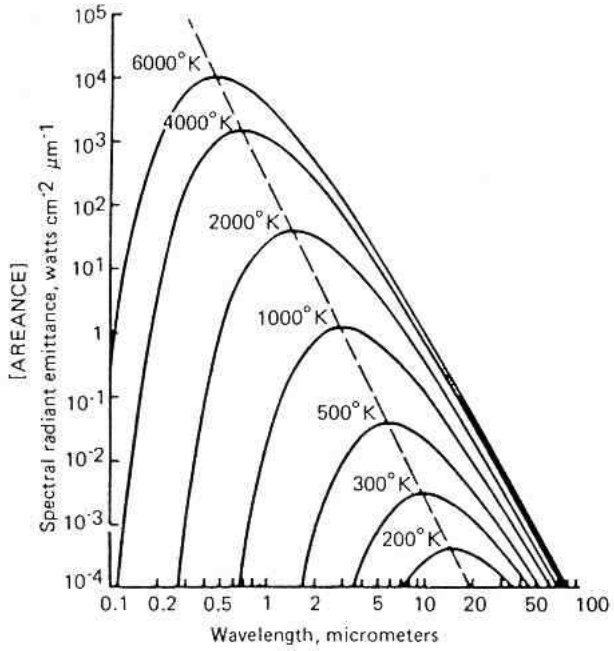

Figure 2.2. Radiant emittance of a blackbody versus blackbody temperature[4].

Today, it is understood that every object emits radiation proportional to its temperature because of atomic oscillations. Most simply, the hotter the object, the faster the frequency of the atoms oscillations and therefore the higher the frequency of radiation emitted by the object.

2.2 Infrared Photon Detector

IR detectors fall into two broad categories, namely photon and thermal. But we will discuss only photon detectors. A transducer is a device that converts one type of signal to another. We can think of the IR detector as a transducer that converts infrared to electrical signals. The incoming radiation and the electrical signal generated are both described in terms of wavelength, frequencies, power, and spectral distribution. One thing to be careful of is to make a distinction between the input (IR) signal, with its wavelengths, frequencies, and power, and the output (electrical) signal, with its wavelengths, frequencies, and power. The infrared wavelengths have values of a few micrometers, with frequencies of about 10^{14} Hz. The electrical signals generated by infrared photon detectors are interesting only at low frequencies from dc up to a megahertz or less.

2.2.1 Detector Parameters

Before beginning the discussion of detectors, the parameters that describe how well the detectors perform will be discussed. Even though we need define these parameters in terms of the detector outputs and the radiometric inputs and other test condition for the specific detector. Here the definitions of detector parameters will be discussed.

Responsivity

The basic function of a detector is to convert radiant input to an output signal of some convenient type such as electrical signal either a current or a voltage. The responsivity (R) is the ratio between the output signal and the radiant input. In order to define the radiant input, the incidence E can be defined. The incidence is the flux density at a detector, exposed either in watts per square centimeter (W/cm^2) or photons per second per square centimeter [photons/($cm^2 \cdot s$)]. The radiant input is the product of the incidence and the detector area A_d. Responsivity is an important parameter for a detector. It allows users to determine ahead of time how sensitive a measuring circuit they will require to see the expected output, or how much amplifier gain they need to get the signal levels up to a satisfactory level. It is most common to express the output signal in volts or currents and the IR input in watts, so the usual units of responsivity are volts/watt (V/W) or ampere/watts (A/W).

Noise

Noise refers to an electrical output rather than the desired signal. Some noise sources are fundamental and cannot be avoided. The reasons are following. Photons do not arrive at an absolutely constant rate. Second, atoms in the detector vibrate slightly, even at low temperature. Third, electrons move randomly within the detector. Since noise is a random deviation from the average signal output, some convention is required to decide how to assign a signal number to a given noise pattern. The usual definition is the root-mean-square (rms) deviation.

Detectivity

The most commonly used parameter to characterize the minimum power a sensor can detect is the specific detectivity. The specific detectivity (D^*) is the signal to noise ratio that would result if the performance of a detector were scaled to a detector of standard size, under standard test conditions.

$$D^* = \frac{responsivity \times \sqrt{area}}{noise/\sqrt{f}} \qquad \text{Eq (2.1)}$$

The units of D^* are $cm \cdot Hz^{1/2}/W$. The specific detectivity is useful in predicting signal to noise ratio that can be expected in a given test environment.

2.2.2 Applications of Infrared detectors

Referring back to Figure 2.2, it is apparent that all but the hottest objects have peak emission wavelengths in the infrared. This is one reason infrared lasers and detectors have countless numbers of applications. Applications using infrared lasers and detectors can be classified into three groups of users having different requirements: industrial, military, and medical. A number of these applications are described in detail to provide background for the operating characteristics required by each application.

The heat signature of the fighter planes and missiles have made the infrared seeker one of the best choices for the target detection systems[5,6]. Several new military applications are using coupled infrared detectors and emitters. One Example of such systems is smart bombs, which follow the infrared reflection of the target illuminated by an infrared laser tracking system. Another example is the infrared active countermeasure systems, using an infrared laser beam to jam the seeker of a missile by actively reading its chopper signal and tuning the jamming laser

beam to the chopper pattern. Both of these applications take advantage of the two infrared atmospheric transmission windows: between 3-5 μm and 8-12 μm. Shown in Figure 2.3 is the transmission of the atmosphere at sea level. In the atmospheric transmission windows, infrared light can propagate with very little attenuation, thereby requiring only a small amount of power to travel a long distance.

Infrared thermal imaging has found many industrial applications especially in non-destructive testing and inspection techniques[7]. Fast and easy detection of hidden cracks and non-uniformity is one of the examples of this technique which is based on the change of thermal resistance of the fractured area. This technique has been successfully used for the detection of hidden cracks under the airport runways and detection of knots in the wood industry[8]. Infrared spectroscopy is also widely used in many industries for continuous monitoring of chemical quality and process control[9].

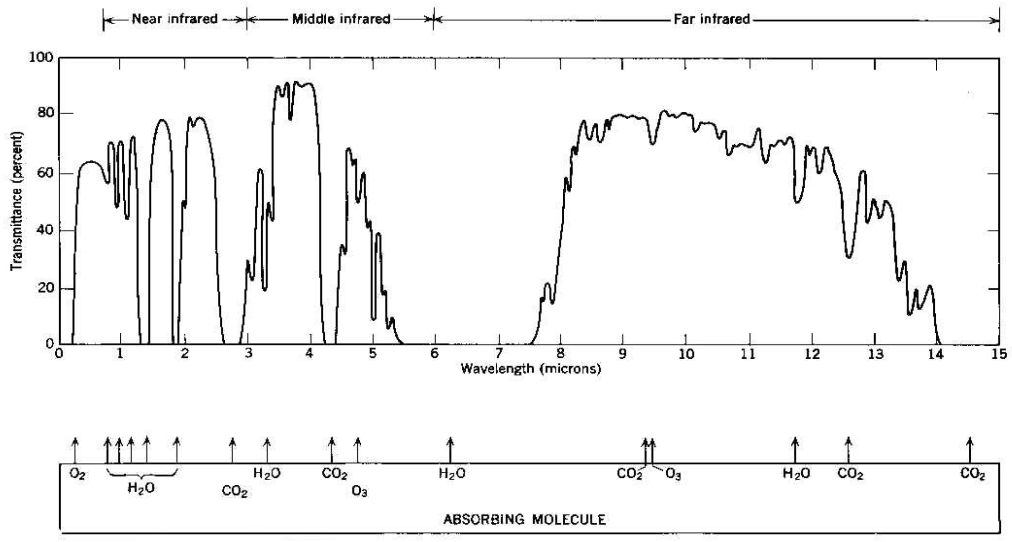

Figure 2.3. Atmospheric transmission versus wavelength. The atmospheric transmission windows are between 3-5 μm and 8-12 μm[3].

Infrared detectors have also found many medical applications, based on the facts that many kinds of malfunctions and abnormal situations can change the blood flow pattern in the tissues which leads to a change in their temperature characteristics. Therefore, thermal imaging has provided a relatively reliable and safe method for early diagnosis of breast cancer[10], dental[11] and thyroid diseases[12]. Several new noninvasive techniques have been developed in recent years due to the rapid improvement of the infrared detectors and emitters. Non-invasive measurement of the oxygen level in the organs during surgery[13] and blood sugar monitoring[14] are examples of these recently available methods, which are based on the infrared spectroscopy techniques.

Besides these applications, the low absorption rate in the atmospheric 3-5μm and 8-12μm windows makes the infrared detectors an attractive choice for many other applications such as range finding, LIDARs, remote sensing, and free space communication.

2.2.3 Types of Photon detectors

In photon detectors, the radiation is absorbed within the material by interaction with electrons which are either free electrons or electrons bound to lattice atoms or impurity atoms. When these electrons are excited to conduction states, a photovoltage or photocurrent results.

1) Extrinsic semiconductor photon detectors

These are photoconductor-type detector made from the intrinsic semiconductor materials silicon or germanium. Although the energy gap (E_g) between the conduction and valence bands in Si or Ge is too large for infrared absorption, the addition of impurities creates allowed levels E_i within the energy gap, as show in Figure 2.4.

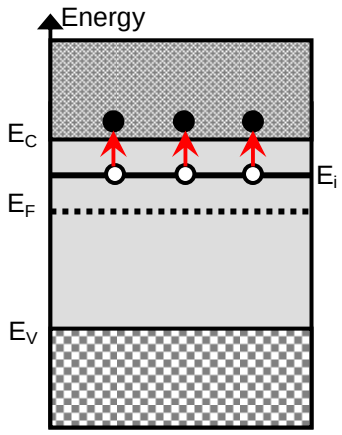

Figure 2.4. Band diagram of a conventional extrinsic infrared photodetector.

The absorption of photons with energy greater than E_C-E_i (activation energy) makes an electron pass from an impurity level to the conduction band. This process increases the number of electrons in the conduction band and the result is photoconduction. One of the examples of the extrinsic detectors is Si with Ga impurity. Its activation energy is 0.0723 eV, which results in a relative spectral response cutoff of 18 μm. In order to distinguish between photo-excited carriers and thermally excited carriers, the average thermal energy, k_BT, of impurity electrons must be cooled to much less than its activation energy. For Si:Ga detectors, it corresponds to an operating temperature of 30K.

2) Intrinsic semiconductor photon detectors

These detectors can be photoconductors or photovoltaic detectors. In order to produce absorption, the energy of the incident photon must be greater that the width of the energy gap. The excited electron can then pass from the valence band into the conduction band and this contributes to the conductivity.

Since the spectral response of an intrinsic photon detector is determined by the energy gap that exists between the conduction and valence bands, the use of the ternary alloy materials whose bandgaps can be varied by tailoring the alloy constitutes have been developed. The most common alloy systems are $Hg_{1-x}Cd_xTe$ (mercury cadmium telluride or MCT), $InAs_xSb_{1-x}$ (indium arsenide antimonide), $InSb_xBi_{1-x}$ (indium antimonide bismuth) etc. But MCT is most well developed and has best performances compared to other detectors in terms of the quantum efficiency and detectivity.

3) Quantum wells and superlattice detectors

Since the initial proposal by Esaki and Tsu[15] and the advent of MBE, the interest in semiconductor superlattices (SLs) and quantum well structures has increased continuously over the years, driven by technological challenges, new physical concepts and phenomena as well as promising applications. A new class of materials and heterojunctions with unique electronic and optical properties has been developed. One of the infrared detectors based on semiconductor supperlattices is Type-II superlattice photodetector[16]. Type-II structures allow the electronic band structure to be engineered by simply changing the thickness or composition of the constituent layers. Therefore, the Auger recombination rate and other losses can be reduced thus reducing the threshold current density and increasing the maximum operation temperature. The detecting wavelength of type-II detectors can be adjusted to a wide range, by simply changing the thickness of the layers. Type-II detectors also have advantages of excellent carrier confinement, suppression of Auger loss, and large gain. The disadvantages of these detectors are inherent in the structure. One is the complexity of the structure. Each layer in the superlattice is

around tens of subnanometer thick and so the active region usually consists of approximately hundreds of layers.

On the other hand, quantum well infrared photodetectors (QWIPs) are based on the quantum well structures in the active region of the devices. These detectors rely on the optical transition within a single energy band and are therefore independent on the bandgap of the detecting material. In QWIPs, infrared absorption occurs via intersubband transitions. The transition energy is determined by the energy levels in each quantum well due to one dimension confinement of carriers, and can be varied by changing its structure.

An extension of QWIPs is the quantum dot infrared photodetector (QDIP) which utilize intersubband absorption between bound states in the conduction/valence band in quantum dots. In a later chapter, Quantum dot infrared photodetector will be discussed in detail.

2.3 Comparison of existing semiconductor detector technologies

At present efforts in infrared detector research are directed towards improving the performance of single element devices, large electronically scanned arrays and higher operating temperature. Another important aim is to make IR detectors cheaper and more convenient to use.

Nowadays the dominant detector technology is based on MCT. MCT is most extensively developed material system for 3-12 μm region. It currently provides state-of-the-art performance for single element detectors operating at MWIR and LWIR windows. The disadvantages of this material are associated with difficulties in its growth, processing, and device stability. In the LWIR region, MCT has a cutoff wavelength which is very sensitive to the composition. In addition, it is very difficult to control the incorporation of mercury, especially at the high

compositions required for longer wavelength detectors. The problem of non-uniform composition leads to non-uniform detector with uncertainty of peak wavelength. Further non-uniformity in quantum efficiency and responsivity among the detectors in an array creates great difficulty in producing high quality arrays of large size (1024×1024) when using MCT. The ultimate result of the difficulty in growing the MCT material is low yields of acceptable arrays.

On the other hand, quantum well infrared photodetectors suffer low quantum efficiency compared to MCT. The low quantum efficiency is due to the smaller absorption coefficient for intersubband transitions in comparison to interband transitions. By nature n-type QWIPs need special optical coupling scheme to incorporate normal incidence light. QWIPs cannot compete with MCT photodiode as the single device, especially at temperature above 70K due to fundamental limitations associated with intersubband transitions. The advantage of QWIP over MCT is relatively easy to grow very uniform material over a large wafer, which make it easy for the fabrication of large format FPA.

Both MCT and QWIP require cryogenic cooling to lower the temperature which is bulky and consume a large energy. So Attractions on high operating temperature detectors have been grown.

2.4 Motivation of Our work

Motivation of our work is to develop quantum dot infrared photodetectors which can outperform the quantum well infrared photodetector with higher operating temperature and higher performance. In a later chapter, we will discuss the operation principle of the QDIP and their expected advantages in more detail.

Photon Detector Type	Advantages	Disadvantages
Intrinsic		
IV-VI (PbS, PbSe,PbSnTe)	Easier to prepare	Very high thermal expansion coefficienty
	Most stable materials	Large permittivity
II-VI (HgCdTe)	Easy bandgap tailoring	Non-uniformity over large area
	Well developed theory and exp.	High cost in growth and processing
	Muticolour detectors	Surface instability
III-V (InGaAs, InAs, InSb, InAsSb)	Good material and dopants	Heteroepitaxy with large lattice mismatch
	Advanced technology	Long wavelength cutoff limited to 7μm(at 77K)
	Possible monolithic integration	
Extrinsic (Si:Ga, Si:As, Ge:Cu, Ge:Hg)	Very long wavelength operation	High thermal generation
	Relatively simple technology	Extremely low temperature operation
Quantum wells/Supperlattice		
Type I (GaAs/AlGaAs, InGaAs/AlGaAs, InP/InGaAs)	Matured material growth	High thermal generation
	Good uniformity over large area	Complicated design and growth
	Muticolour detectors	Optical coupling for normal incidence
Type II (InAs/InGaSb, InAs/InAsSb, InAs/GaSb)	Low Auger recombination rate	Complicated design and growth
	Easy wavelength control	Sensitive to the interfaces
Qunatum dots (InAs/GaAs, InGaAs/InGaP, InAs/InP)	Normal incidence of light	Complicated design and growth
	Low thermal generation	Low quantum efficiency

Table 2.1. Comparison of infrared detectors

3 Overview of Quantum dot infrared photodetector

The area of research on infrared detectors utilizing semiconductor quantum dots or nanostructures has been very active nowadays. Drawing a similarity to the success of the quantum well infrared photodetector (QWIP), the quantum dot infrared photodetector (QDIP) has attracted a lot of interests. Presently QWIPs are being commercialized for infrared imaging application. An ideal QDIP is expected to be substantially superior to QWIP.

3.1 Operation of principle

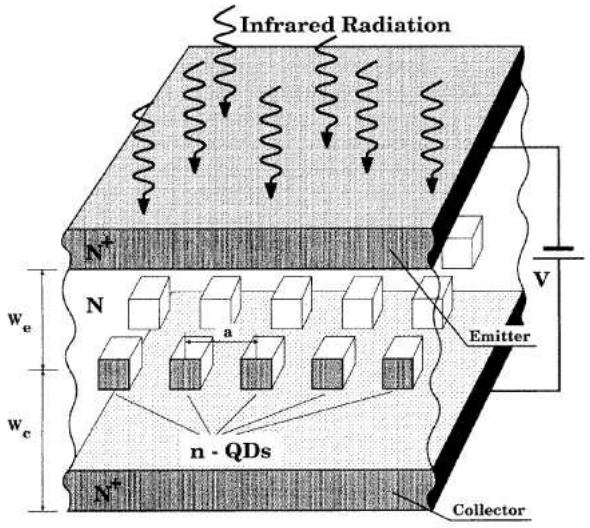

Figure 3.1. The schematic view of the QDIP structure[17].

Generally, the structure of QDIPs are similar to those of QWIPs in that quantum wells are replaced by quantum dots which play the role of a photosensitive base for the QDIP. The typical structure of QDIPs consists of an N^+-N (or i)-N^+ diode structure with an array of QDs inserted in the undoped barriers. Each self-assembled QDs are formed by a nanometer-size semiconductor cluster of a narrow-gap material which is buried in the barrier material of large-gap material. The QDs are located in a plane parallel to the arrays of the N^+-N (or i)-N^+ structure shown in Figure 3.1. The quantum dots can be directly doped through dopants or unintentionally doped. The current QDIP devices usually have n-type doping profiles and thus unipolar nature in contrast with the interband lasers which are bipolar devices.

The electron charges in the QDs result in the formation of the emitter and collector barriers. These barriers have a nearly triangular form and their heights are nearly independent of the in-plane coordinates. Under illumination by infrared radiation, the in-plane potential

distribution and the height of the emitter and collector barriers vary due to the shift of the balance between the excitation and capture of the electrons by means of photoionization of the QDs. This leads to the extra injection of electrons from the emitter to the collector through the QD array.

The current of the extra injected electrons can significantly exceed the current of the electrons photoexcited from the QDs. This means that the photoelectric gain can be much more than unity.

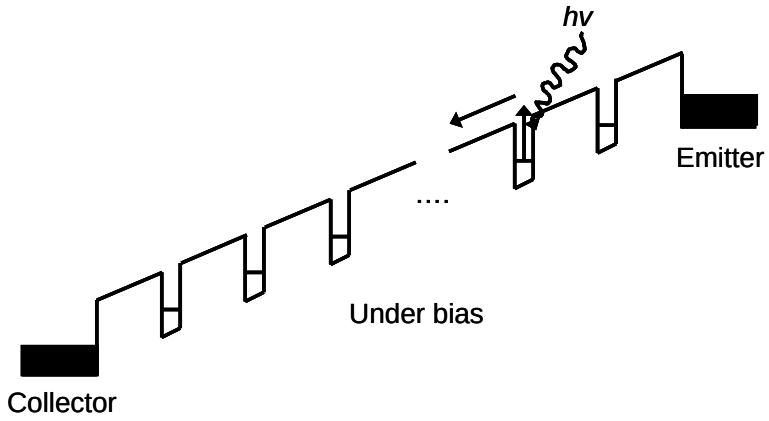

Figure 3.2. Schematic potential profile for QWIPs and QDIPs. The detection mechanism in both devices is by intersubband photoexcitation.

3.2 Expected Advantages of Characteristics in QDIP

One of the major advantages is that QDIPs allow normal incidence. The incident light normal to the wafer along the growth direction is expected to cause the intersubband absorption unlike the standard n-type QWIPs. The normal incidence property is advantageous because it avoids the need of fabricating a grating coupler in the standard QWIP imaging arrays. The grating coupler not only adds at least extra fabrication step but also cause difficulties in realizing

a wide and multiple wavelength coverage because of its spectrally peaked nature and in fabricating a short wavelength coupler because of the required small grating features.

Another potential advantage of QDIPs over QWIPs is that QDIPs have lower dark currents. Since the dark current causes the noise, a lower dark current leads to higher detector sensitivity. The simplest way to estimate dark current is by counting the mobile carrier density in the barrier and then the current is given by multiplying the carrier velocity. The following expression can be used.

$$j_{dark} = evn_{3D} \qquad \text{Eq (3.1)}$$

where v is the drift velocity and n_{3D} is the three-dimensional density, both for electrons in the barrier. Eq (3.1) neglects the diffusion contribution. The electron density can be estimated by

$$n_{3D} = 2\left(\frac{m_b k_B T}{2\pi\hbar^2}\right)^{3/2} \exp\left(-\frac{E_a}{k_B T}\right) \qquad \text{Eq (3.2)}$$

Where m_b is the barrier effective mass and E_a is the thermal activation energy which equals the energy difference between the top of the barrier and the Fermi level in the well or dot. We have assumed that $E_a/k_BT>>1$, appropriate for most practical cases. Eq (3.2) can be easily derived by integrating the 3D density of state and Fermi distribution above the barriers. For similar barriers in a QWIP or a QDIP, the difference in E_a gives rise to a difference in dark current. If we neglect the field induced barrier lowering effect in E_a which makes the estimation valid for low applied fields, the activation energy relates to detection cut-off wavelength (λ_c) by

$$E_a^{QWIP} = \frac{hc}{\lambda_c} - E_f \qquad \text{Eq (3.3)}$$

for a QWIP with a bound-to-continuum detection scheme, and for a QDIP

$$E_a^{QDIP} = \frac{hc}{\lambda_c} \qquad \text{Eq (3.4)}$$

where E_f is the Fermi level in the well. The term E_f in Eq (3.3) is due to the subband nature of quantum wells in QWIPs.

The final advantage relates to the potentially long excited electron lifetime τ_{life}. It has been anticipated that the relaxation of electrons is substantially slowed when the inter-level spacing is larger than the phonon energy-"phonon bottleneck". In later chapter, this effect will be discussed in more detail. If the phonon bottleneck can be fully implemented in a QDIP, the long excited electron lifetime directly leads to a higher responsivity, higher operating temperature, and higher dark current limited detectivity. The photoconductor responsivity is given by

$$R = \frac{e}{hv}\eta g \qquad \text{Eq (3.5)}$$

where v is the photon frequency, η is the absorption efficiency, and g is the photoconductive gain

$$g = \frac{\tau_{life}}{\tau_{ttrans}} \qquad \text{Eq (3.6)}$$

where τ_{trans} is the transit time across the device. A long τ_{lifes} directly translates into a large R. High operating temperature and high detectivity are immediate consequences[18].

4 Unique physical properties of Self-Assembled Quantum Dots

As the dimension of the structure decreases, the physical properties of the systems become different. For example, the electronic structure of bulk semiconductors has delocalized electronic states and their energy spectrum in the conduction and valence bands are continuous. In semiconductor nanostructures where the electrons are confined in small regions of space in the range of a few tens of nanometers or below, the energy spectrum is significantly affected by the confinement. In this chapter, we will discuss the unique physical properties of low dimensional structure and specially focus on the semiconductor quantum dots.

4.1 Density of states

For the example of the quantum well, the confined states within the one-dimensional potential could hold two charge carriers of opposite spin, from the Pauli Exclusion Principle and broaden into subbands, thus allowing a continuous range of carrier momenta. Then we can raise the question about the distribution of their energy and momenta, given a particular number of electrons or holes within a subband. But this question can be raised about other low dimension quantum confined states such as the quantum wire and the quantum dot. In order to answer this question, the concept of the density of states is required. The density of states means that how many electrons or holes can exist within a range of energies. It is important to look over the density of states of various dimensional structures because they determine their unique electrical and optical properties.

4.1.1 Bulk

According to Bloch's theorem, an eigenstate within a bulk semiconductor can be written as

$$\Psi(\vec{r}) = \frac{1}{\Omega}\exp(i\vec{k}\cdot\vec{r}) \qquad \text{Eq (4.1)}$$

where Ω is the volume of the bulk semiconductor.

The eigenstate should display periodicity within the lattice, then if the unit cell is of side L, $\Psi(x,y,z) = \Psi(x+L, y+L, z+L) = 1/\Omega \exp[i(k_x x + k_y y + k_z z)]\exp[i(k_x L + k_y L + k_z L)]$ should be satisfied. For the periodicity condition to be fulfilled $\exp[i(k_x L + k_y L + k_z L)]$ must be identical to 1, which indicates that

$$k_x = \frac{2\pi}{L}n_x \qquad k_y = \frac{2\pi}{L}n_y \qquad k_z = \frac{2\pi}{L}n_z \qquad \text{Eq (4.2)}$$

where n_x, n_y, and n_z are integers. Each set of values of these three integers defines a distinct state, and hence the volume of **k**-space occupied by one state is $(2\pi/L)^3$. The density of states is defined as the number of states per energy unit volume of real space:

$$\rho(E) = \frac{dN}{dE} \qquad \text{Eq (4.3)}$$

In **k**-space, the total number of states N is equal to the volume of the sphere of radius **k**, divided by the volume occupied by one state and divided again by the volume of real space,

$$N = 2\frac{4\pi k^3}{3}\frac{1}{(2\pi/L)^3}\frac{1}{L^3} = 2\frac{4\pi k^3}{3(2\pi)^3} \qquad \text{Eq (4.4)}$$

where the factor of 2 has been introduced to allow for double occupancy of each state by the different carrier spins. Then according to Eq (4.4),

$$\rho(E) = \frac{dN}{dE} = \frac{dN}{dk}\frac{dk}{dE} \qquad \text{Eq (4.5)}$$

From Eq (4.4), dN / dk can be easily calculated. In addition, the parabolic bands of effective mass theory give the dispersion relation between energy and momentum.

$$E = \frac{\hbar^2 k^2}{2m^*} \qquad \text{Eq (4.6)}$$

Finally the density of states in bulk semiconductor is following

$$\rho(E) = \frac{1}{2\pi^2}\left(\frac{2m^2}{\hbar^2}\right)^{\frac{3}{2}}\sqrt{E} \qquad \text{Eq (4.7)}$$

4.1.2 Quantum well

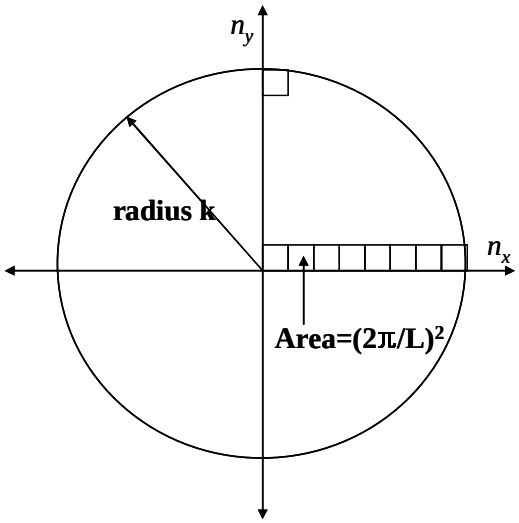

Figure 4.1. Illustration of the two dimensional momenta states in a quantum well.

The density of states in quantum well systems can be deduced in a similar way as the case of bulk. But the number of the degrees of freedom is two. The available volume or area in **k**-space with successive states represented by values of n_x and n_y is illustrated in Figure 4.1. The

total number of states per unit area is given by the spin degeneracy factor, multiplied by the area of the circle of radius k, divided by the area occupied by each state,

$$N^{2D} = 2\pi k^2 \frac{1}{(2\pi/L)^2}\frac{1}{L^2} = \frac{2\pi k}{(2\pi)^2} \qquad \text{Eq (4.8)}$$

In analogy to the bulk three dimensional case with Eq (4.5), the density of state of a two-dimensional quantum well is

$$\rho^{2D}(E) = \frac{k}{2\pi}\left(\frac{2m^*}{\hbar^2}\right)^{\frac{1}{2}} E^{-\frac{1}{2}} \qquad \text{Eq (4.9)}$$

with the in-plane dispersion curves still described by parabolas, Eq (4.6). Finally substituting Eq (4.6), the density of states for a single subband in a quantum well system is given by:

$$\rho^{2D}(E) = \frac{m^*}{\pi\hbar^2} \qquad \text{Eq (4.10)}$$

If there are n confined states within the quantum well system then the density of states ρ^{2D} at any particular energy is the sum over all subbands below that point, which can be written as

$$\rho^{2D}(E) = \sum_{i=1}^{n} \frac{m^*}{\pi\hbar^2}\Theta(E - E_i) \qquad \text{Eq (4.11)}$$

where Θ is the unit step function.

4.1.3 Quantum wire

In quantum wires, the confinement takes place in two directions (e.g. x, y) of space and the carrier motion is free in other direction (z). The number of density of quantum wire can be formulated in a similar way as Eq (4.8),

$$N^{1D} = 2 \cdot 2k \frac{1}{(2\pi / L)} \frac{1}{L} = \frac{2k}{\pi} \qquad \text{Eq (4.12)}$$

With parabolic approximation, the density of states in quantum wire systems is given by

$$\rho^{1D} = \sqrt{\frac{2m^*}{\hbar^2}} \frac{1}{\pi\sqrt{E}} \qquad \text{Eq (4.13)}$$

Like in quantum well systems, if there are subbands within a quantum wire, the density of the states is the summation of all subbands below certain energy E_i.

$$\rho^{1D}(E) = \sum_{i=1}^{n} \sqrt{\frac{2m^*}{\hbar^2}} \frac{1}{\pi\sqrt{E}} \Theta(E - E_i) \qquad \text{Eq (4.14)}$$

The density of states is equal to zero when $E<E_i$. Thus 1D density of states is highly peaked, since it presents singularities at each value of E_i.

4.1.4 Quantum dot

In quantum dots, the confinement takes place in the three directions of space, the main consequence is that the electronic spectrum consists in series of discrete levels, like in isolated atoms. Therefore the density of states of quantum dots consists of δ functions at the discrete energies:

$$\rho^{0D}(E) = 2\sum_{i=1}^{n} \delta(E - E_i) \qquad \text{Eq (4.15)}$$

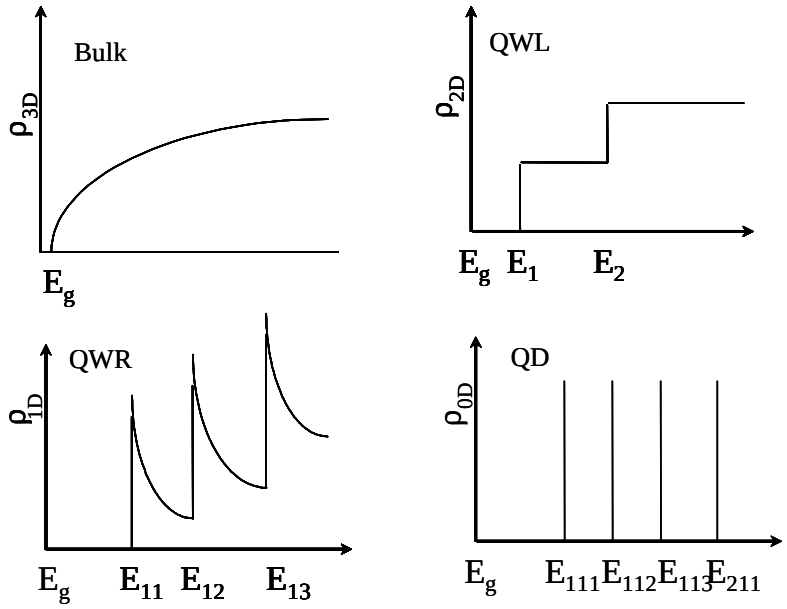

Figure 4.2. Comparison between the density of states at 3D, 2D, 1D and 0D.

4.2 Phonon Bottleneck

4.2.1 Theoretical background

The electronic states in all solid structures are subject to different scattering mechanism such as electron-electron, electron-phonon, and electron-impurity scattering. Especially the scatterings related to electron or phonon are inherent to solid state of matter. Concerning the hot carriers, the emission of phonon is important to nonradiative relaxation mechanism because it is very efficient channel to distribute the energy of the electrons into the medium.

The phonon is kind of quantum version of classical normal modes. In classical theory of the harmonic crystal the lattice vibration is described by the motion of the atoms that are connected by the ideal spring.

In classical mechanics, even very complicated motions are explained in terms of normal modes. We consider one-dimensional Bravais lattice with two ions per primitive cell, with equilibrium position. After solving equation of motion of this system, we can have two ω (frequency) versus k (wave vector) curves which are referred to as the two branches of the dispersion relation[19].

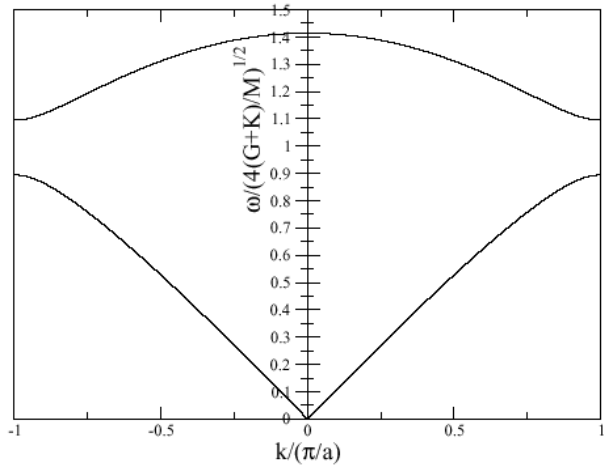

Figure 4.3. Dispersion curves for one-dimensional chain with two atoms per cell.

In the lower branch, ω vanishes linearly in k for small k, and the curves becomes flat at the edges of the Brillouin zone. This branch is known as the acoustic branch because its dispersion relation is of the form $\omega = ck$ characteristic of sound waves, at small k. The second branch starts at k with non-zero value and decreases with increasing k. This branch is known as the optical branch because the long wavelength optical modes in ionic crystals can interact with electromagnetic radiation, and are responsible for much of the characteristic optical behavior. In three dimensional case, there are three dispersion curves for each acoustical and optical branch.

Phonon distorts the local crystal structure and hence distorts the local band structure. This distortion affects the conduction electrons. Here are important effects of the coupling of electrons

with phonons. Electrons are scattered from one state to another state, leading to electrical resistivity. Phonon can be absorbed in the scattering event, leading to the attenuation of ultrasonic waves. An electron will carry a crystal distortion with it, and the effective mass of the electron is thereby increased. A crystal distortion associated with one electron can be sensed by a second electron, thereby causing the electron-electron interaction.

We first look at the effect of phonon scattering and energy relaxation in electron gas in terms of confinement dimension such as 1, 2, and 3 dimensions[20].

For the quantitative calculation, the semiconductor system can be used that is a rectangular $In_{0.47}Ga_{0.53}As$ quantum well with a width of 100Å embedded in InP for two-dimensional basis. The lateral confinement is modeled by potential barriers of infinite height outside the wire or dot region, which enables a complete separation of the carrier motion in the three spatial directions. The wavefunctions in growth direction (z) are the solutions of the finite-barrier quantum well problem, which are harmonic functions $[\sin(k_w z), \cos(k_w z)]$ inside the well matched to exponential decreasing tails $[\exp(-k_b z)]$ in the barriers. Let's denote n, m, l as the standard (z, y, x) quantum numbers of a quantum-well, -wire, or –dot system in the infinite square well approximation.

Electron-phonon scattering times τ can be calculated in first-order perturbation theory using the Fermi golden rule,

$$\tau_{i\to f}^{-1} = \frac{2\pi}{\hbar}\sum_{f,q}\alpha^2(q)\left|\langle\psi_f \mid e^{\mp iq\cdot r} \mid \psi_i\rangle\right|^2 \times \delta\left(E_f - E_i \pm E_q\right)\left[n_B(E_q, T_l) + \begin{pmatrix}1\\0\end{pmatrix}\right] \qquad \text{Eq (4.16)}$$

The upper (lower) signs account for emission (absorption) of phonons by an electron in the initial quantum state i. The sum extends over all possible final-electron quantum numbers f and

phonon wave vectors q. The electron energies E_i and E_f are always measured from the bottom of the respective 0D, 1D or 2D ground subbands. n_B stands for the Bose distribution function $n_B(E,T)=(e^{(E/kT)}-1)^{-1}$. E_q is the energy of a phonon with wave vector q and T_l is the lattice temperature.

For the coupling of the electron to LA phonons by means of a deformation potential D, the expression

$$\alpha^2(q)=\frac{D^2}{2\rho c_s^2\Omega}\hbar c_s q \qquad \text{Eq (4.17)}$$

is used with D=7.2 eV, a density ρ=5500 kg/m^3, and a longitudinal velocity of sound c_s=3400 m/s.

The electron-phonon matrix element in Eq (4.16) separates in the x, y, and z coordinates and has been calculated analytically.

For a confined lateral direction (for example, x), the matrix element can be calculated analytically

$$\left|\left\langle \varphi_x^n \mid e^{iq_x x} \mid \varphi_x^{n'} \right\rangle\right|^2 = M_x^{n,n'}(q_x)$$
$$= \frac{1}{4}\left[\begin{array}{l} \dfrac{\sin(Q+K_i+K_f)}{Q+K_i+K_f}+\dfrac{\sin(Q+K_i-K_f)}{Q+K_i-K_f}\pm \\ \dfrac{\sin(Q-K_i+K_f)}{Q-K_i+K_f}\pm\dfrac{\sin(Q-K_i-K_f)}{Q-K_i-K_f} \end{array}\right] \qquad \text{Eq (4.18)}$$

with $Q=q_xL_x/2, K_i=n\pi/2, K_f=n'\pi/2$. The upper signs mean by the band index n and n' either even or odd, the lower signs are for one of them even and the other odd. This matrix element decreases rapidly with increasing $q_xL_x>>1$.

Then we have numerical calculation of Eq (4.16) for LA phonon scattering. For this calculation we have chosen the same energy difference ΔE between the initial and the lowest electron state for the quantum dot (0D), quantum wire (1D), and quantum well (2D). The corresponding 2D situation is an electron of energy

$$\Delta E = \hbar^2 / 2m^* (\pi / L)^2 (2^2 - 1^2)$$

in the ground quantum well subband.

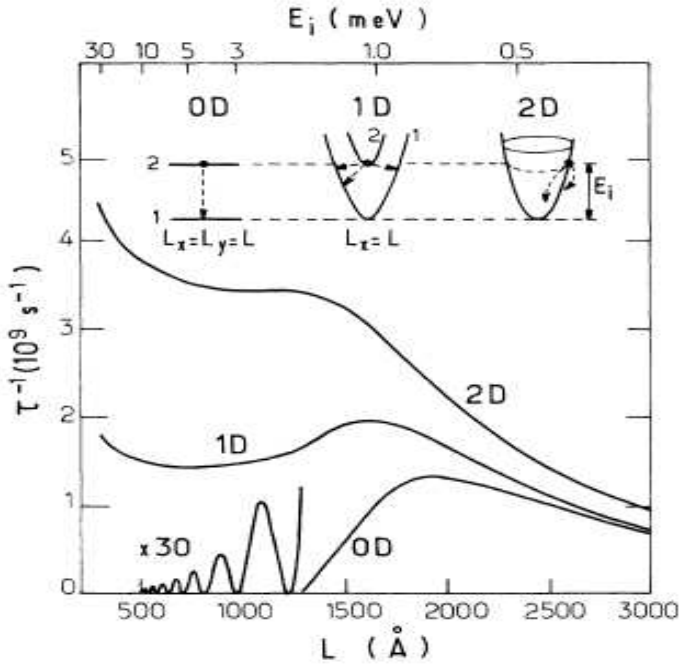

Figure 4.4. Emission rates of LA phonons from 0D, 1D, and 2D electron gases. L indicates the lateral layer widths and defines the initial energy (upper scale) the 0D scattering rates plotted below 1300A are multiplied by a factor of 30. T_l = 4 K from Ref 20.

When the lateral size L exceeds 2000 Å, the three scattering rates decrease monotonously and become very close. This means that any physical difference between the zero-, one-, and two-dimensional systems disappear when the lateral confinement becomes weak. In the 1D and

2D cases there always exists a continuum of final electron states and possible phonon energies. The quantum dot system has only the ground state available below ΔE. Thus, the emitted LA phonon spectrum consists of a single line with $q = \Delta E / \hbar c_s$. For L below ~1300Å, τ_{0D}^{-1} is smaller than τ_{1D}^{-1} and τ_{2D}^{-1} by more than one order of magnitude and exhibits strong oscillations.

The optical phonons have no continuous-energy spectrum in this approach. For the 0D system the discrete electrons and phonon energies prevent any first-order interaction, except for the special case $E_i - E_f = \hbar\omega_{LO}$. A finite scattering time can result from broadening of the electron and phonon spectra, renormalization of the phonons due to the confinement and higher-order interaction terms.

In typical 3D and 2D systems, electrons meet holes both in real and k space. Elastic collisions randomize k directions very quickly. Energy is lost first through LO phonon emission and next through acoustic phonons in the sub-nanosecond ranges due to the 2D continuum of final states. With electron lifetime carriers thermalize at their band edges and decay radiatively there. In case of 0D, relaxation rate vanish, mainly due to the scarcity of final states satisfying both energy and momentum conservation.

Above figure which is the result of calculation of total decay rate of electron and hole shows the slow relaxation in high-energy states. Carriers clearly accumulate whenever a larger ΔE induces a slow relaxation. This effect is called as phonon bottleneck.

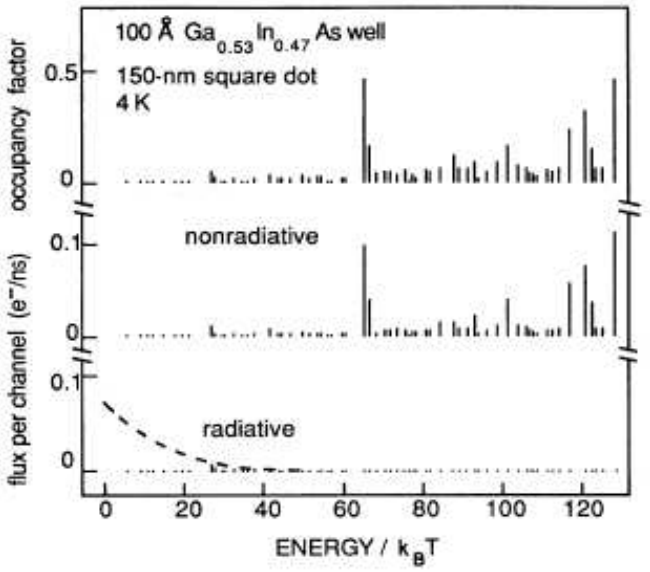

Figure 4.5. Occupancy (upper part), nonradiative flux (middle part), and radiative flux (bottom part) of the 66 levels of a quantum box at 4 K of size L_x =150 nm for the 100 A $Ga_{0.53}In_{0.47}As/InP$ well system as a function of the reduced energy (E/k_BT). The dashed line schematizes the radiative probability reflecting the thermal hole distribution from Ref 21.

4.2.2 Experimental observation of phonon bottleneck

The decreased relaxation probability makes QDs prone to competing recombination processes and has been made responsible for the low quantum yield of early QD structures especially for laser applications. However Self-organized QDs show bright intrinsic ground state luminescence after non resonant excitation (excite electron and hole in different QD) and PL rise time of only a few tens picoseconds are observed at low excitation densities. In order to explain the fast and efficient relaxation alternative processes such as Coulomb scattering, Auger scattering, and defect-induced tunneling has been suggested. We can distinguish two limits for the density regime. The low-density regime means a single carrier or exciton in an otherwise

empty QD with no additional carriers in the barrier and on the other hand, in the high-density regime carriers or excitons are present in the QD or the barrier. In this case Auger and Coulomb scattering are expected to be the most efficient relaxation processes and might account for the observed fast carrier relaxation in actual device structures.

J. Urayama et al.[22] reported the experimental observation of phonon bottleneck in quantum dot electronic relaxation by differential transmission measurement. Electron-hole scattering in QD usually masks the phonon bottleneck effect by Coulomb interaction which leads to fast relaxation. For the investigation of the intersublevel electron transition, it is necessary to have special carrier capture path. There are two kinds of carrier capture mechanism. One is Germinate (pair) capture, and the other is Non-Germinate capture.

If electron-hole pairs are photoinjected into the continuum above the quantum dots, and the number of carriers is much lower than the number of accessible dots, the carrier capture process will occur mainly in two different configurations. In Germinate capture, the electron and hole settle into the same dot.

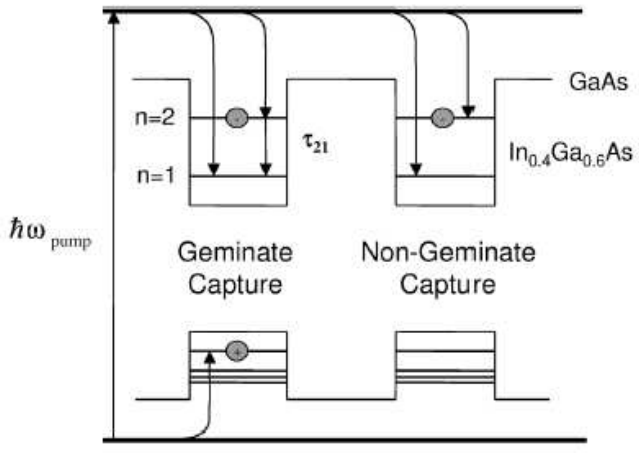

Figure 4.6. Carrier capture model with germinate and non-germinate configuration.

The other is the unpaired capture in which the electron and hole fall into two different, laterally separated dots. Germinate captured electrons will undergo fast relaxation due to electron and hole scattering and non-germinate capture electrons will experience a phonon bottleneck in the relaxation. The n=2 time scan shown in Figure 4.7 (a) reveals that after a very fast capture into the dot excited state, some of the carriers relax quickly, as indicated by the fast decay component of the differential transmission (DT) signal. In longer time scans shown in Figure 4.7 (b), the tail decays at a rate lower than the recombination rate (~250 ps). This slowly decaying signal is a clear sign of the predicted phonon bottleneck. Even in the resonantly pumped DT scan Figure 4.7 (c) the relaxation seems to be suppressed due to the combination of germinate and non-germinate capture process.

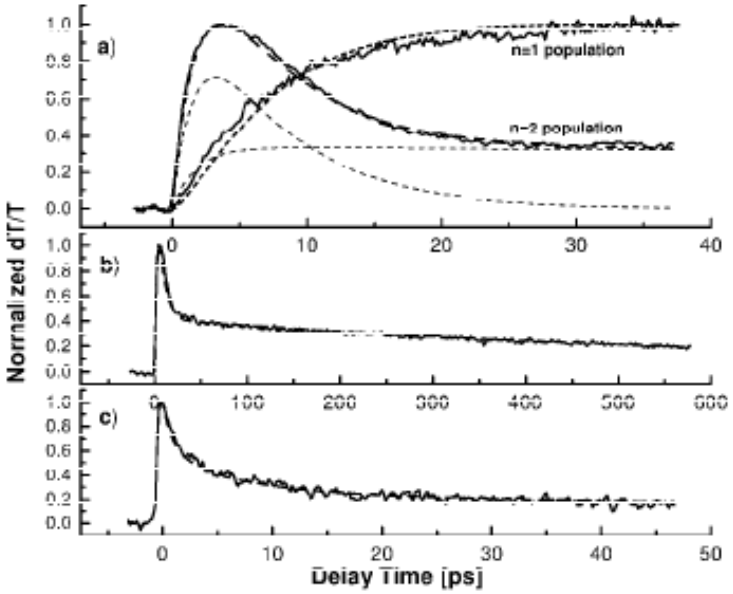

Figure 4.7. DT time scans taken at 40 K. The rate equation fits are shown as dark dashed lines. (a) Nonresonantly pumped DT scan for n=1 (980 nm) and n=2 (910 nm) dot levels. The

germinate and non-germinate components of n=2 fits are given as light dashed line. (b) DT time scan n=2 level with a long delay. (c) Resonantly pumped DT scan for n=2 dot level from Ref 22.

4.2.3 Effect on Quantum Dot Infrared Photodetector

For the quantum dot infrared photodetector application, the intersublevel transitions are major principle of physics which creates the photoconductivity. For the measurement of photoconductivity, MWIR absorption excites carriers from bound QD states to higher energies so that the carriers can be swept away by applied electric field and thus generates a photocurrent. Two different situations can be distinguished. (i) Transitions into the continuum band, where the carriers can move away directly and (ii) transitions between two bound states, where the excited carriers can only contribute to the photocurrent via tunneling or thermionic emission. In QDIP structure, QDs are embedded in the N^+-N(or i)-N^+ structure. A schematic conduction band profile of such a sample is shown in Figure 4.8. When the inter-level of energy spacing is larger than LO phonon energy, the relaxation of electron is very much slowed. This phonon bottleneck effect on the excited state electron causes the increased carrier capture and relaxation times, leading to an efficient detection of radiation since photoexcited carriers are less likely to be captured into QDs or relax to the ground state before being swept away as a photocurrent. This results in increased extraction efficiency and increased operating temperatures.

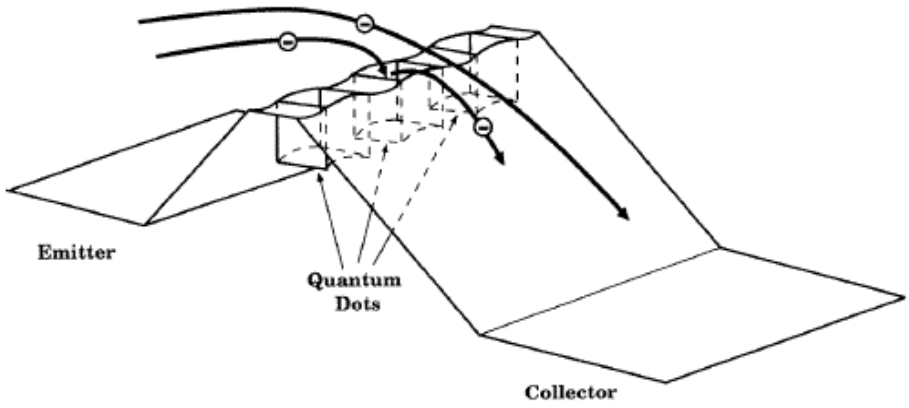

Figure 4.8. Conduction band profile in the QDIP from Ref 17.

4.2.4 Conclusion

The physical origin of phonon bottleneck is explained by the simplified model of square box quantum dot. The scattering time of electron-phonon can be calculated with Fermi golden rule. The occupancy of the excited electrons is simulated showing the slow relaxation of excited state electrons in quantum dot. There were many experiments on measuring relaxation times of electrons, but many experiments didn't distinguish the other effects which lead to fast relaxation of electron via electron-hole scattering. Excluding the electron-hole scattering, the intersublevel transition of electrons has long relaxation time and it was confirmed by the experiment. In QDIP, infrared light excites the electron to higher energy state and phonon bottleneck results in the high responsivity and high temperature operation.

5 QDIP Fabrication and Measurement

5.1 Growth techniques of SAQDs

In this chapter, the experimental methods to fabrication of the QDIP devices will be described from the growth of the quantum dots to test mesa of QDIP for the measurement.

5.1.1 Growth Mechanism

Generally the semiconductor self-assembled quantum dot can be grown either with Molecular Beam Epitaxy (MBE) or Metal Organic Chemical Vapor Deposition (MOCVD) via Stranski-Krastanow (SK) growth mode. When for a strained epilayer with small interface energy, initial growth may occur layer-by-layer up to the critical thickness, but a thicker layer, which should be less than the thickness where the dislocation occurs, has large strain energy and can lower its energy by forming isolated islands in which the strain is relaxed. Thus SK growth mode occurs. In order to form quantum dots on a substrate or any matrix material, the lattice mismatch between quantum dot material and should be above certain value (2%). Even though there is large enough lattice mismatch between two materials, it does not guarantee the quantum dot formation. The uses of quantum dot in the device applications and searching for the novel physical properties lie in the confinement of electrons or holes in the quantum dots. So the lattice constant of quantum dot material should be larger than the substrate or the matrix material so that the confinement of electrons and holes can exist and compressive strain enables the quantum dot material to wet on the matrix material. Typical materials of the epitaxial III-V semiconductor quantum dot are In(Ga)(Al)As(P) on GaAs and InP substrates. Most works on the III-V

semiconductor quantum dot have been focused on InAs/GaAs system using the Molecular Beam Epitaxy (MBE). In this work, we have used two material systems such as InAs on InP and GaInAs on GaInP lattice-matched to GaAs substrate via Low Pressure-Metal Organic Chemical Vapor Deposition (LP-MOCVD).

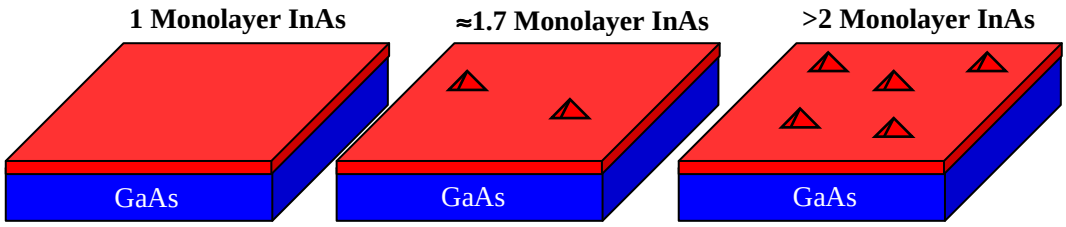

Figure 5.1. Evolution of quantum dots as the amount of InAs increases.

5.1.2 Growth of SAQDs by Molecular Beam Epitaxy (MBE)

Molecular Beam Epitaxy (MBE) is a technique for the epitaxial growth of materials. It operates via chemical interaction of one or several molecular or atomic beams of different intensities and compositions, which occurs on the surface of a heated single crystalline substrate. A special feature about the MBE is that it can control the layer thickness, composition and the doping profile very precisely with very slow growth rate (~ 1 ML/sec). This feasibility can be achieved by opening and closing the relevant fluxes using the shutters with which each cell is equipped. The operation time of a shutter (< 1s) is usually less than the time needed to grow one monolayer (1~5 s). Another feature is that the MBE chamber is equipped with a reflection high energy electron diffraction (RHEED) system. The RHEED enables to monitor not only the reconstruction of the film surface, but also its smoothness at the monolayer level, the surface diffusion length of migration atoms, and the deposition rate.

In case of quantum dot growth with MBE, there are several things to be pointed out. First, for the quantum dot growth, relatively slow growth rate is used compared to the growth rate for the bulk material.

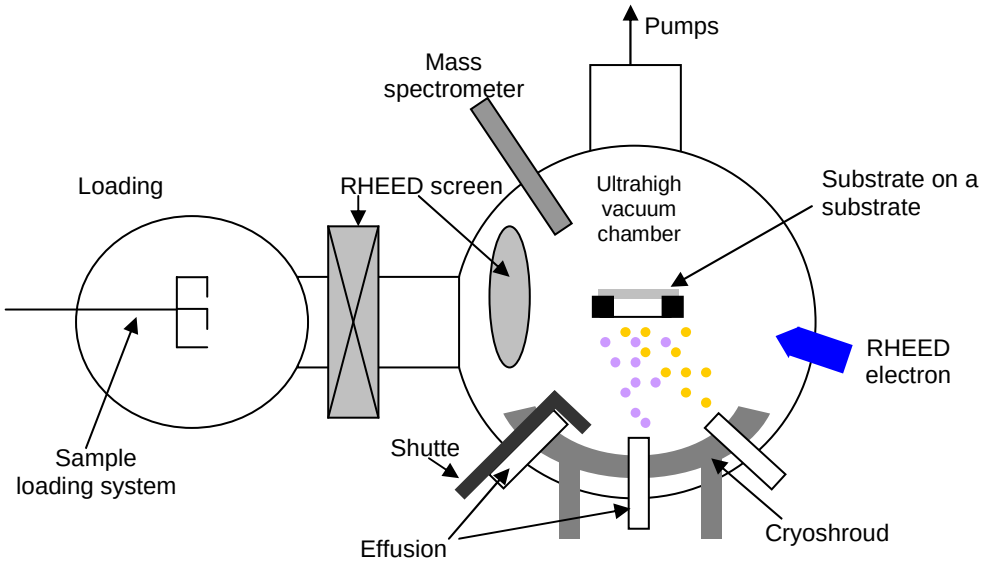

Figure 5.2. Schematic diagram of Molecular Beam Epitaxy (MBE).

For example, in order for InAs quantum dots to form on GaAs, the amount of InAs material should be above the critical thickness which is around 1.7 monolayer (~ 5Å), but less than the critical thickness for dislocated islands (~ 4ML). Normally the quantum dots with good optical and electrical properties for the device applications are coherent islands, which are dislocation-free islands. Incoherent islands occur from strain relaxation when larger amounts of material are deposited[23]. But this situation can be also applied to the quantum dot growth by MOCVD. The growth environments between MBE and MOCVD are different. One advantage with MBE is that it is equipped with RHEED. RHEED pattern can be monitored during the growth. In the usual InAs quantum dot growth, the formation of dots started after the deposition

of a ~0.5 nm thick InAs wetting layer and led to the transformation of a streaky RHEED pattern to a dashed one. Further InAs deposition resulted in well-developed diffraction spots typical for a three-dimensional growth mode. The growth conditions such as the growth temperature, the growth rate, the growth time, and V/III ratio should be optimized for the desired shape, size and density of the quantum dots.

5.1.3 Growth of SAQDs by Metalorganic Chemical Vapor Deposition (MOCVD)

Metalorganic chemical vapor deposition (MOCVD), also known as Metalorganic vapor phase epitaxy (MOVPE), is another modern growth technique widely applied to grow semiconductor heterostructures including quantum wires and quantum dot nanostructure.

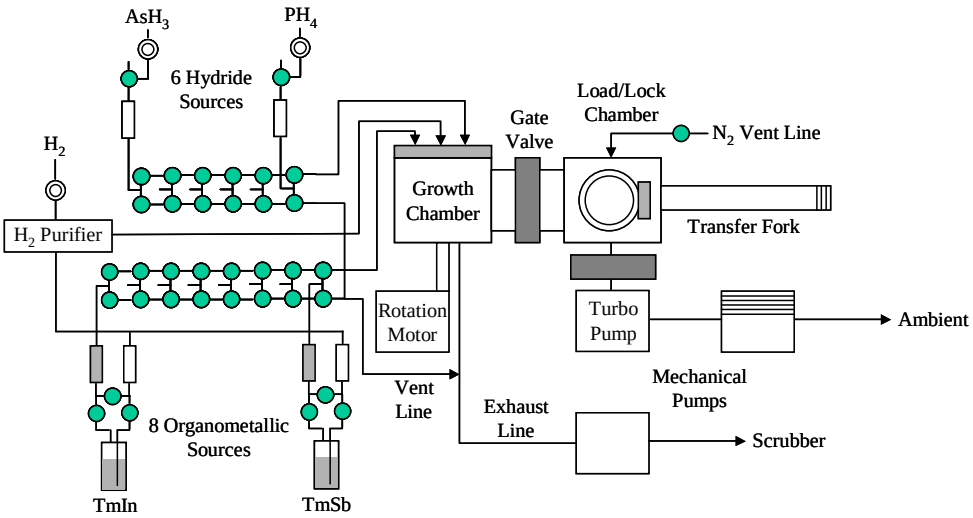

Figure 5.3. Schematic of the Emcore LP- MOCVD reactor which has been used to grow the QDIP device structures.

MOCVD uses various precursors for group III and group V elements. For example, Triethygallium $(C_2H_5)_3Ga$, TrimethyIndium $(CH_3)_3In$, TrimethyAluminum $(CH_3)_3Al$ etc. for

group III and the phosphine (PH_3) for the phosphorus and the arsine (AsH_3) for the arsenic for group V can be used. If the precursor is in the vapor phase, a defined gas flux mixed with the carrier gas is directed into the reactor.Less volatile liquid or solid precursors are placed in special bubblers, through which the carrier gas flows. These bubblers are, in turn, placed in the thermal baths, to stabilize the concentration of the precursors within the carrier gas. The flowing gas, saturated with the Metalorganic precursors, flows into the reactor with a well defined flux. The gas flux with group III precursors is only mixed with the gas flux with group V precursors at the reactor entrance, in order to avoid pre-reactions. The precursors dissolve in the carrier gas and flow with the laminar flux over the heated susceptor at a typical pressure of 20~100 Torr. The temperature of the susceptor determines the growth temperature. The typical growth temperature of high quality of III-V semiconductor is around 450-700 °C. Significant oversaturation of the reactants leads to the growth of a crystal over a substrate.

The works on the growth of quantum dots by MOCVD are limited compared to those by MBE. The reason would be the growth control is relatively more difficult than in MBE. But the MOCVD can give better material qualities and enables mass-production for the device structures.

5.2 QDIP fabrication

After the growth of the device structure, next step will be fabrication of single detectors for the characterization and measurement of the QDIP detector. In a typical wafer grown for the device structure, there are a number of test mesas. In order to fabricate QDIP test mesas, multiple processing steps such as cleaning, photolithographic patterning, etching, evaporation of metal

contacts, bonding to the heat sink, and finally wire bonding are required. The details of processing steps are a little different depending on the materials dealt with because of different etching and Ohmic contact material. But generally the overall steps are in principle similar. In this chapter we will discuss the fabrication steps of QDIP detectors. The brief processing steps are following.

1. Cleaning the substrate
2. Photolithography for mesa definition
3. Mesa pattern transfer with dry etching
4. Photolithography for metallization
5. Electron beam evaporation or and thermal evaporation
6. Metal lift-off
7. Rapid thermal annealing
8. Die bonding and wire-bonding

5.2.1 Photolithography

The photolithography is the standard process for transferring device patterns from mask to substrate in integrated chip fabrication. This method uses a photosensitive resist layer, patterned mask and UV light to achieve critical dimensions. In general, the resolution of photolithography is limited by diffraction and quality of the optics. There are two types of photoresist: positive and negative. For positive resists, the resist is exposed with UV light wherever the underlying material is to be removed. In these resists, exposure to the UV light changes the chemical structure of the resist so that it becomes more soluble in the developer. The exposed resist is then

washed away by the developer solution, leaving windows of the bare underlying material. Negative resists behave in just the opposite manner. Exposure to the UV light causes the negative resist to become polymerized, and more difficult to dissolve. Therefore, the negative resist remains on the surface wherever it is exposed, and the developer solution removes only the unexposed portions.

Photolithography for mesa definition

In a standard photolithography process for test mesa definition, first a polymer resist is spun onto the substrate material or device structure. The resist is then soft baked to harden the resist and make it stable under certain mechanical pressure. A chrome and glass mask brought into soft contact with the resist layer and UV light is then incident on the resist and mask. The chrome regions block UV light from reaching the resist. Finally, a developer chemical is used to remove the exposed resist. The photoresist pattern after development acts as the etching mask for the mesa definition. We will talk about the etching process later.

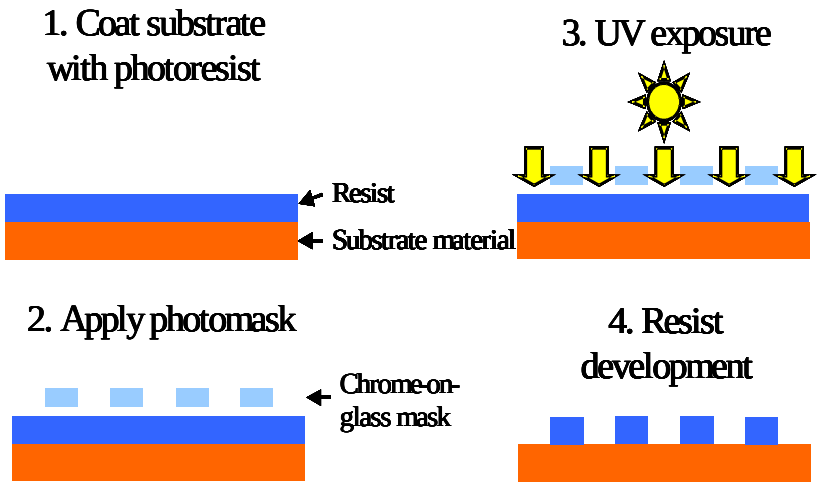

Figure 5.4. The photolithography process for mesa definition using positive resist.

Photolithography for metallization

In order to deposit metals on the device structure to make ohmic contacts, the lift-off process is necessary. If the standard photolithography were used to define the contact, it can be very difficult to have good lift-off because of the lack of the undercut profile in the developed pattern. Instead the continuous film forms (see Figure 5.5).

In order to overcome this problem, we need to use the image reversal technique to form the undercut profile. After initial exposure of the metal contact pattern, the resist should be heated at ~100℃ in order to change the chemical property of the resist, which means the exposed region will be insoluble and will not contain photosensitive compounds to react in subsequent UV exposure. A flood exposure, which is UV exposure without a mask, is used to expose the area previously unreacted which, when developed, creates a negative image of the original mask.

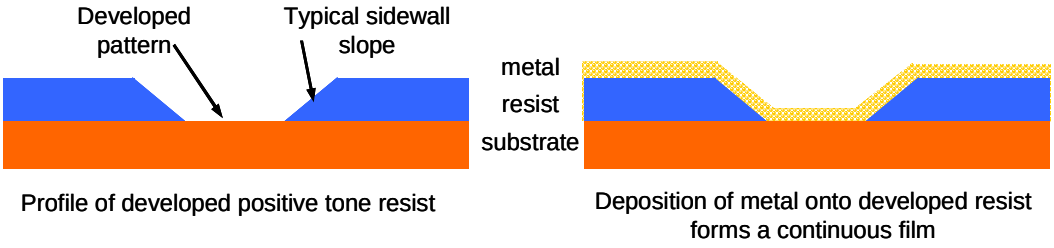

Figure 5.5. Problem of normal photolithography for metallization.

Thus the flood exposed positive resist is reversed and functions as if it is a negative photoresist. This process is called “image reversal”. After image reversal, the sidewall slope that worked against the lift-off in positive tone now forms the undercut profile, which is favorable for lift-off. When the metal is evaporated, the film is discontinuous over the desired features. Now the resist can be removed cleanly, leaving a well-defined metallization pattern behind (see Figure 5.6).

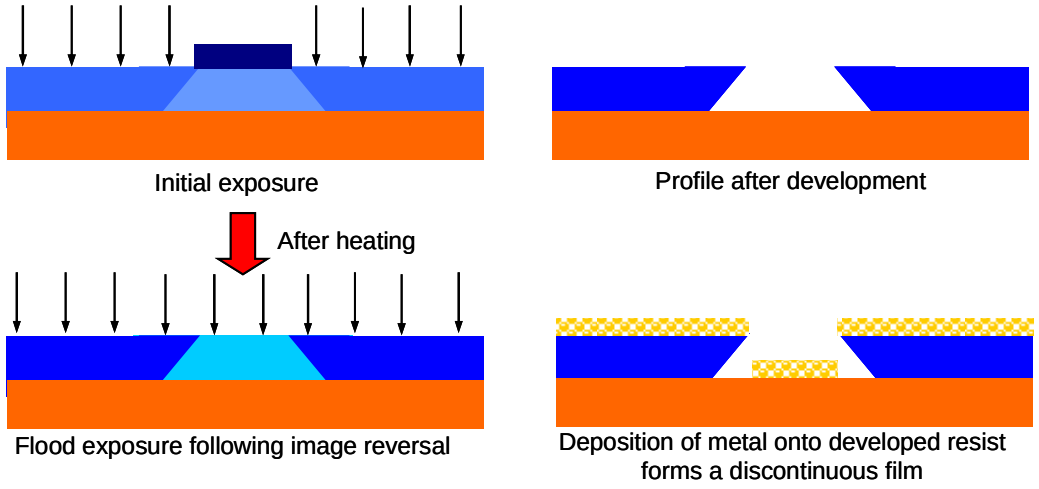

Figure 5.6. Image reversal for metallization through flood exposure.

5.2.2 Dry etching by electron cyclotron resonance reactive ion etching (ECR-RIE)

In order to define the test mesas, it is necessary to etch the device structures uniformly up to certain thickness. The plasma or dry etchings are used for the all the etchings required in our works. In the ECR-RIE, the plasma is excited by a microwave field of 2.45 GHz in the presence of a dc magnetic field of the correct magnitude to cause the electrons to spiral at the microwave frequency, thus increasing the probability of ionization. This dense plasma is extracted and applied to the specimen table by the application of an independent rf field of 13.56 MHz. The potential advantages of the ECR-RIE over RIE lie in this separation of the fields which first create the plasma and then impart energy to the ions. So far, ECR-RIE processes have been developed for etching GaAs and InP based materials. The etching rate usually increases with rf power. However, high momentum gas ions created by higher rf power causes serious damage to the etching surface. Another method to control the etching rate is to change the ion density.

Increasing ion density can be done by coupling 2.45 GHz microwave power into the plasma under a magnetic field.

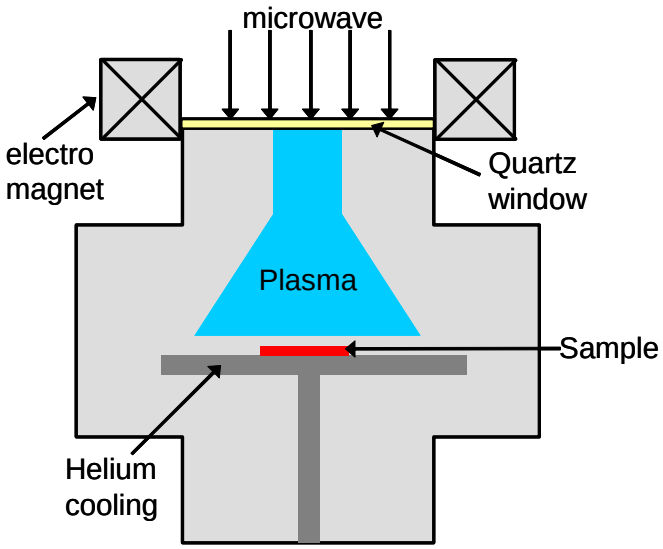

Figure 5.7. Operation principle of ECR-RIE reaction.

A Plasma-Therm SLR-770 ECR-RIE system is currently being used at CQD. This system has a capability of handling 14 different gas sources and is controlled by a computer. During the etching, the substrate is fixed with heat-conductive grease on a 3-in Si carrier wafer and the large amount of heat generated during the etching is cooled by helium gas from the bottom side of the Si wafer. We use different gases for etching GaAs and InP based QDIP.

5.2.3 Metallization

To deposit thin metallic films for device contacts, an electron beam metal deposition system is used. The sample is loaded upside down in a vacuum bell jar chamber. After the proper vacuum around usually ~10^{-7} torr is attained, the electron source is turned on by applying high voltage of 10 kV and directed at a selected boat, which may contain Au, Ti, Ni, Pt or other

materials. After the metal is heated to its melting point, uniform deposition begins to take place within the vacuum chamber. A film monitor near the sample is used to measure the metal deposition rate and overall thickness. The deposition rate should be controlled at a low rate (< 3 Å) through the control of the emission current. Another important issue for uniform evaporation is to level the sample relative to the source. Slight tilt will cause non-uniform in metal thickness. After the deposition of one kind of metal, if next other kind of metal should be deposited, the crucible should be cooled off for 2~3 minutes and then change the source and resume a next deposition. For GaAs QDIP, it is necessary to deposit AuGe alloy to make Ohmic contact on GaAs. The thermal evaporation is used for AuGe evaporation. In thermal evaporator, the material is heated up by passing a high current through a highly refractory metal containment such as a tungsten boat. The thickness is also monitored in real-time by a quartz crystal and is controlled by the amount of the input current.

5.2.4 Procedure steps for QDIP fabrications

The steps for QDIP fabrication will be discussed in detail. The real processing of the device requires very delicate handling of samples and a lot of care. Multiple device structures are usually grown for the device optimization. Therefore the different device structures are fabricated at the same time except that when the device structures have different etching thickness, the etching of the devices should be done separately. The samples must be properly labeled not to mix them. It is better to grow on large substrates so we can have enough test pieces.

1. **Cleaning procedure before processing**

- Rinse in boiling trichloroethylene (TCE - $ClCH:CCl_2$) for 5 minutes to remove any residual organic grease. TCE is soluable in acetone.
- Rinse in acetone (CH_3OH) for 5 minutes to remove any polymer residue from the plastic sample holder.
- Rinse in heated methanol ($(CH_3)_2OH$) for 5 minutes.
- Rinse in second bath of heated methanol for 5 minutes. Methanol is water soluble
- Blow dry with high purity nitrogen and verify that the samples are totally free of everything except growth defects.
- Rinse in de-ionized(DI) water for 5 minutes.

2. Photolithography for mesa definition

- HMDS resist is spun on the substrate with a speed of 4000 rpm for 30 seconds and right after then AZ 5214 resist is also spun with 4000 rpm for 30 seconds. After finishing spinning two types of resists, the substrate undergoes softbaking at 96ºC for 50 sec. This softbaking removes the solvent in the resist and harden the resist layers.
- With Mask I-1 (400×400 μm^2 squares), the mask and the substrate are aligned and the sample is exposed for 13 sec (UV power ~9.6mW/cm^2) with MJB-3 aligner. Here the exposure time can be changed so it is recommended to check the condition quite often.
- After exposure, the resist on the sample needs to be developed with a solution 1:4 ratio of water to AZ400K developer for 10 sec and then rinsed in deionized water

(DI water) for more than 20 seconds. The developing time should be checked with a test piece. The complete photolithography of 400×400 μm^2 is shown in Figure 5.8.

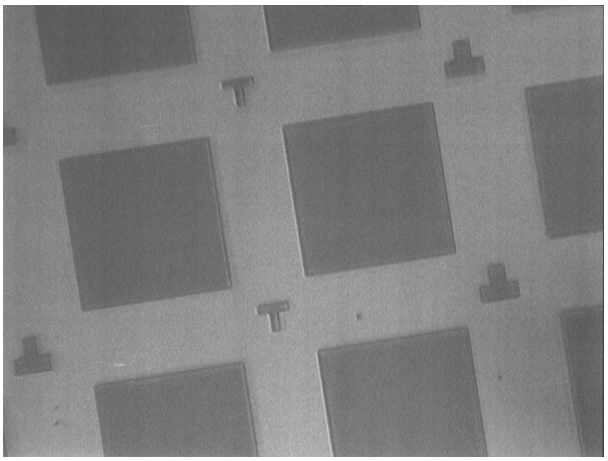

Figure 5.8. After photolithography, the resist etching windows with 400×400 μm^2 area are shown.

3. Mesa pattern transfer with dry etching of QDIP structure

- In order to etch InAs/InP QDIP, the following recipe is used. 32 sccm of Chlorine(Cl_2), 8 sccm of Boron trichloride(BCl_3) and 5 sccm of Argon(Ar) are used. The power of RF1 is 200W and the power of RF2 is 500W. The magnet setting is 180 A for an upper magnet current and 20A for a lower magnet current. The chamber pressure is 1 mTorr. In order to minimize the backward plasma, the stud should be properly set. The typical etching rate with this recipe is around 200 nm/min.
- For etching of the InGaAs/InGaP/GaAs QDIP etching, only 10 sccm of BCl_3 is required. The power of RF1 is 75W and the power of RF2 is 850W. The magnet

setting is 180A for a upper magnet current and 0A for a lower magnet current. The chamber pressure is 1 mTorr. The typical etching rate is around 250 nm/min.

4. Photolithography for metallization

- After etching, the residual photoresist is removed with AZ400T stripper which is heated up to 70ºC with Q-tip to help clean the surface, and then the samples are rinsed very well in flowing DI water for at least 5 minute. In order to remove the grease or other contaminant, the normal cleaning procedure discussed before is repeated.
- HMDS resist is spun on the substrate with a speed of 4000 rpm for 30 seconds and right after then AZ 5214 resist is also spun with 4000 rpm for 30 seconds. After finishing spinning two types of resists, the substrate undergoes softbaking at 96ºC for 50 sec.
- With Mask I-2 which is for the definition of metal top and bottom contacts, after alignment with existing etching mesas, 10 sec exposure is done with the same power as initial photolithography followed by postbaking at 110ºC for 60 seconds. Without any mask, 60 second flood exposure is done.
- The samples are developed in 1:4 ratio AZ400K developer for 10 seconds and rinsed in DI water for more than 20 sec. First a test piece should be checked.

5. Metallization with e-beam evaporator

- InAs/InP: Ti/Pt/Au=400Å/400Å/1400Å.
- InGaAs/InGaP/GaAs: AuGe/Ni/Au= 700Å/350Å/1300Å
- Lift-off with Acetone and rinse sample with methanol and DI water.

6. **Rapid thermal annealing**

   - Do a test run without sample first to make sure the system is working.
   - InAs/InP: 400ºC for 2 min with N_2 forming gas.
   - InGaAs/InGaP/GaAs: 400ºC for 3 min with N_2 forming gas.

7. Die bonding to a copper heat sink with pure indium

   - Pick a good mesa and do the wire bonding. Follow the bonding rule diagram below. (Rules not always applicable – just make sure you know which pad goes to which contact on which mesa)

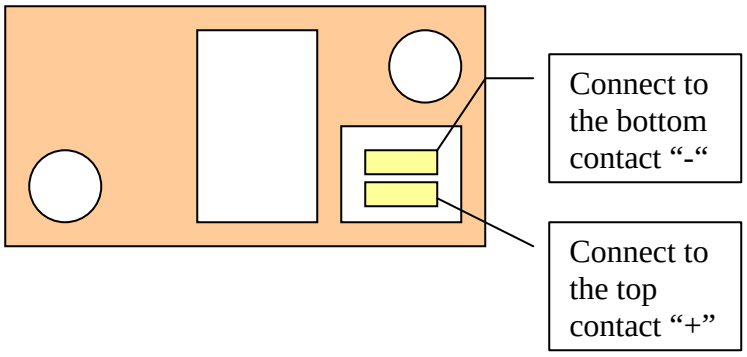

8. Check the room temperature resistance of bonded mesa and write it down. Check the resistance between ceramic pad and copper heat sink. This should be infinity! Change the ceramic pad if it's not infinity.

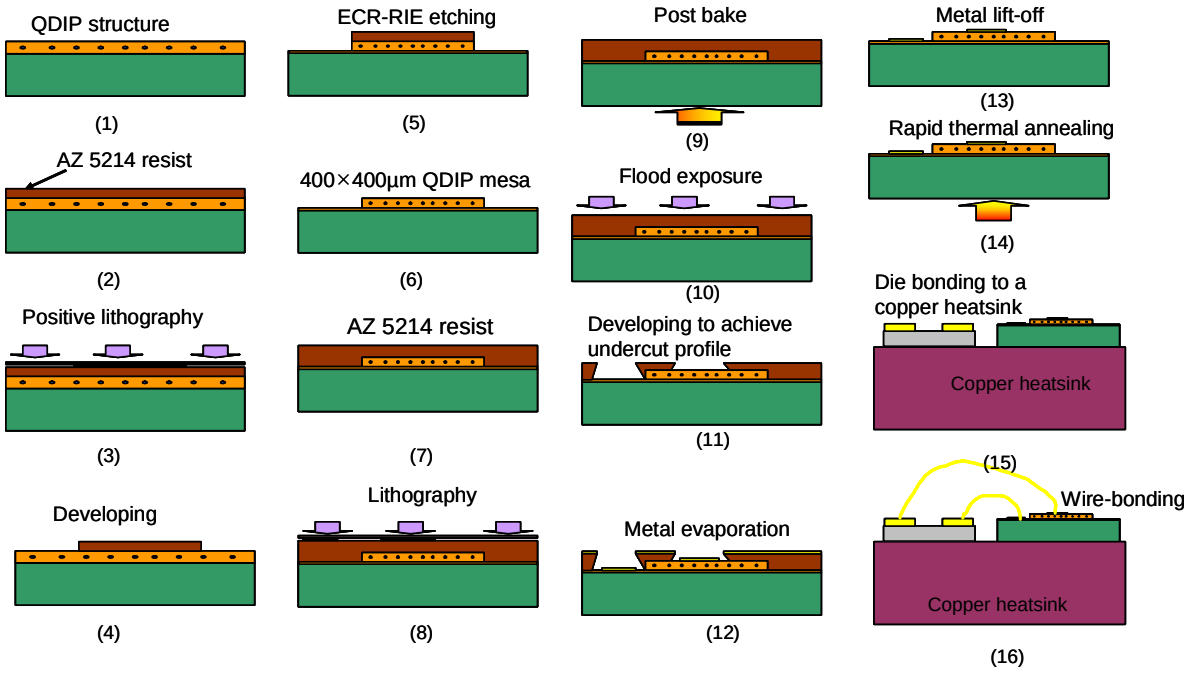

Figure 5.9. Schematic of QDIP test mesa fabrication.

5.3 QDIP Measurement

After finishing QDIP fabrication, next stage is to measure and characterize the performances. The performances of the QDIP detector are characterized usually by the peak detectivity and peak responsivity. We routinely measure FTIR, blackbody response, dark current and noise current. In this section, we will discuss the detail of the measurement.

5.3.1 Blackbody signal and peak responsivity

One of the most important figures of merit of the infrared detector is the peak responsivity. The peak responsivity is calculated from blackbody responsivity and relative responsivity. Optical sources are often characterized in terms of the incidence, E which is the flux density at the detector, either watts per square centimeter of detector area (W/cm^2) or

photons per second per square centimeter (photons/(cm^2·s)). The IR radiant input is the product of the incidence and the detector area A_d. Thus we can calculate responsivity as:

$$R = \frac{signal}{IR\ input} = \frac{S}{E \cdot A_d} \qquad \text{Eq (5.1)}$$

The detector is placed so that it can view a blackbody source and the resulting signal is observed. This signal can either be a DC signal or, an AC signal if the blackbody source is modulated with a chopper. The set-up for the blackbody responsivity is shown Figure 5.10.

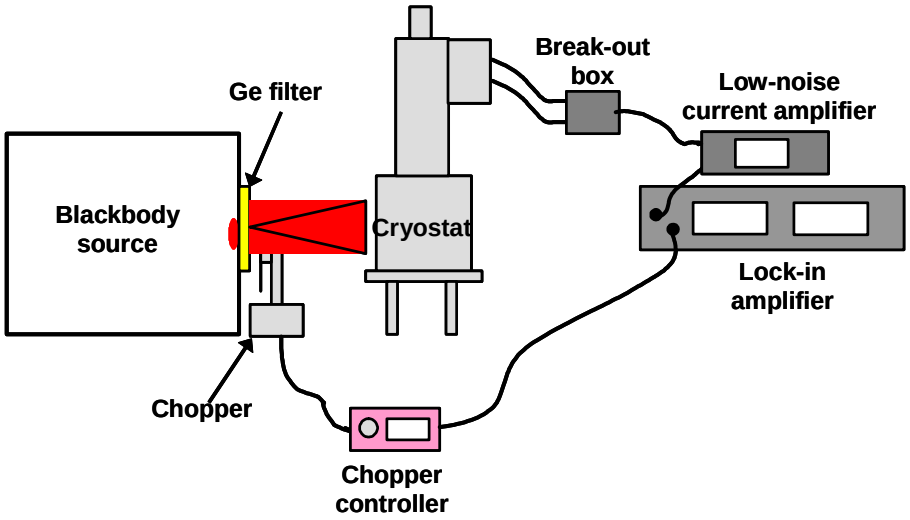

Figure 5.10. Experimental setup for the measurement of blackbody response.

The light from blackbody source through a certain aperture passes a Ge filter whose cut-off wavelength is 3 to 12 μm and is also modulated by a chopper with a frequency of 400 Hz. The sample (QDIP detector) in the cryostat is cooled down to the desired measurement temperature with liquid nitrogen and the temperature can be controlled by the temperature controller. The typical measurement temperature is 77 K and above. The bias applied to the detector is controlled by a current transimpedance amplifier Keithley model 428 and the signal can be amplified through setting a gain. The output voltage signal from the detector is measured

by an EG&G 5209 lock-in amplifier, which is triggered by a signal from the chopper controller. In order to recover the actual photocurrent, the voltage signal is divided by the amplifier transimpedance gain. Once this photocurrent is known, the blackbody responsivity is calculated using Eq (5.1).

The peak responsivity is defined as the responsivity the detector would have if the IR flux from the blackbody were concentrated at the peak wavelength where the detector is most sensitive. The ratio of these two responsivities is called the blackbody-to-peak conversion factor[24]. The formula for the blackbody-to peak conversion factor is given by:

$$C = \frac{M_{bb}}{M_{eff}} \qquad \text{Eq (5.2)}$$

where M_{bb} is the exitance of a blackbody at a blackbody temperature at QDIP detector. The total exitance from blackbody is predicted by Stefan-Boltzmann's Law:

$$M_{tot} = \sigma T^4 \ (\mathrm{W/cm^2}) \qquad \text{Eq (5.3)}$$

where σ is the Stefan-Boltzmann constant=$5.67\times10^{-12}\mathrm{W/(cm^2\cdot K^4)}$ and T is the blackbody temperature in Kelvin. The solid angle through which the QDIP detector sees the blackbody source is:

$$\Omega \approx \pi \frac{r^2}{R^2 + r^2} \qquad \text{Eq (5.4)}$$

where r is the radius of the aperture and R is the distance between the aperture and detector. Since the blackbody projects its radiation into a hemisphere, the projected solid angle of a hemisphere is π. The fraction of blackbody exitance at the plane of a QDIP detector is thus Ω/π. The total blackbody incidence at the QDIP plane is:

$$E_{QDIP} = M_{tot}(\Omega/\pi)T_{total} \qquad \text{Eq (5.5)}$$

where T_{total} is the total transmission coefficient, which includes the transmission of cryostat window, a chopper modulation factor, and a Ge filter. After QDIP response signal is measured, its responsivity can be calculated by:

$$R_{bb} = \frac{I_{signal}}{E_{QDIP}A} \qquad \text{Eq (5.6)}$$

The quantity M_{eff} is the effective exitance which is less than M_{bb}. This smaller amount of energy, if concentrated at the wavelength of peak response, would generate the same signal as did the blackbody. The R'(λ) is called relative responsivity. It is the ratio of the responsivity at wavelength λ to that at the wavelength λ_p where the responsivity is greatest. The R'(λ) has a maximum value of unity, and is often called the normalized response or FTIR because it is measured with FTIR (Fourier Transform Infrared spectrometer). Then the peak responsivity can be calculated as follows:

Peak responsivity (A/W)=Blackbody responsivity (A/W)×C Eq (5.7)

5.3.2 Relative Response Measurements (FTIR)

The relative response R'(λ) is measured with the Mattson Galaxy 3000 FTIR spectrometer at CQD. The schematic diagram of the FTIR system is shown in Figure 5.11. The FTIR system composes of two cube-corner mirrors (labeled 4 and 8), an infrared source (5), an infrared detector (13) and a beam splitter (7) and other mirror systems for guiding the light. The beam splitter reflects 50 percent of an incident light beam and transmits the rest 50 percent simultaneously.

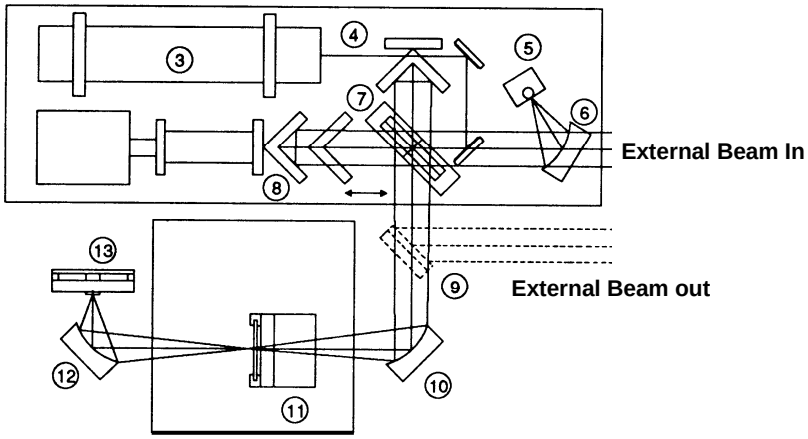

Figure 5.11. Schematic diagram of the Mattson Galaxy 3000 FTIR system.

One part of the split beam travels to the moving interferometer mirror (8) while the other part travels to the fixed interferometer mirror (4). Two mirrors reflect both beams back to the beam splitter where the light recombines. At the beam splitter, half the recombined beam is transmitted to the detector and the other half is reflected toward the infrared source. When two light beams recombine at the beam splitter, an interference pattern is generated. The interference pattern varies with the displacement of the moving mirror along its axis and is detected by the infrared detector as variation in the infrared energy level. In order to change the constructive to the destructive interference, moving the scanning mirror by a quarter wavelength of the incident light which results in sine wave signal is required. Because of the broad range of the frequencies from infrared sources, the resulting interferogram represents the sum of each sine wave generated by each individual frequency component of the input infrared radiation and the frequency and intensity of each sine wave in the interferogram is resolved by the Fourier transformation.

In the experiment, a deuterated-triglycine-surfate (DTGS) thermal detector is used as the reference detector. This detector has a uniform spectral response across the wavelength range

from 2.5 μm to 27 μm. The relative spectrum of QDIP detector is unknown and can be obtained from Eq (5.8). Before the spectral response of QDIP device is collected, the spectral response of DTGS is measured first. Next the QDIP spectral response is measured and its real spectral response is calculated by:

$$R'_{QDIP}(\lambda) = R'_{DTGS}(\lambda)\frac{S_{QDIP}(\lambda)}{S_{DTGS}(\lambda)} \qquad \text{Eq (5.8)}$$

where $R_{DTGS}(\lambda)$ is the spectral response of the DTGS detector, $S_{QDIP}(\lambda)$ is the measured spectrum of the QDIP, and $S_{DTGS}(\lambda)$ is the measured spectrum of the DTGS detector. The normalized spectral response $R'_{DTGS}(\lambda)$ of the reference detector is known from manufacturer's calibration data. The resolution of the Galaxy 3000 FTIR system is $2cm^{-1}$. One wavenumber (cm^{-1}) is equal to 1/10000 μm, so that the spectral response precision of this system at 10 μm is 0.04 μm.

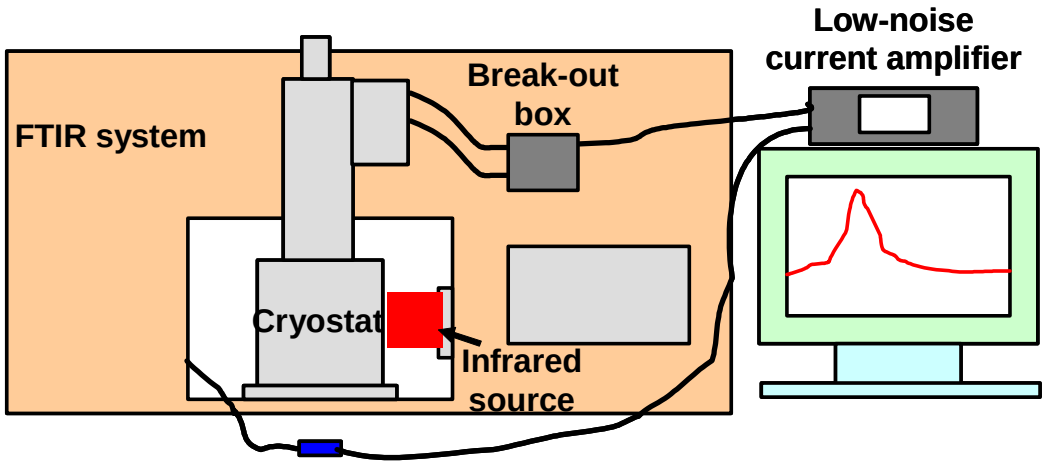

Figure 5.12. Schematic of FTIR measurement setup.

5.3.3 Noise Measurement

The noise can have a significant effect on the device performance such as the peak detectivity. It is important to know what type of the noise is really dominant in the device. In

addition to the noise of the detector generated by the carriers which are optically excited from the target or from the background of a scene, for a photoconductor, however, there are additional mechanisms that can increase the noise level. The sources of these noises are caused by two different types of randomness.

One is the fluctuation in the velocity of the carriers due to collisions between the carriers and lattice atoms. The associated noise is referred to as Johnson noise. Since the degree of motion of the lattice atoms depends on the lattice temperature, the magnitude of Johnson noise also depends on lattice temperature. The expression derived by Johnson for this noise current is

$$i_n \propto \left[\frac{4kT}{R}\right]^{1/2} \sqrt{\Delta f} \qquad \text{Eq (5.9)}$$

Another is the fluctuation in the number of carriers. The random nature of the quantum mechanical optical emission process of the light source and the absorption process of the detector can cause fluctuation in the carrier density. The thermionic emission process in a photoconductor will also increase the mobile carrier density and hence its statistical fluctuation. There are several different types of noise found in QDIP detectors. The noise associated with the generation of the mobile carries is called generation noise. The random recombination process of mobile carriers also contributes to fluctuation of carrier density and hence increases noise. The generation-recombination (g-r) noise then collectively describes the noise caused by the fluctuation in carrier density of a photoconductor. The noise current spectral density caused by this process is derived in the following equation in terms of the noise gain (g_n).

$$I_n^2 = 4eg_n I_{dark} \Delta f \qquad \text{Eq (5.10)}$$

One of the noises is 1/f noise. Although the physical mechanisms causing this noise are not understood yet, it has been observed in non-ohmic contacts and crystal surface. The noise can be minimized by proper fabrication procedures. A general expression for the 1/f noise current is given by

$$i_n \propto \frac{I^2}{fA_d}\sqrt{\Delta f} \qquad \text{Eq (5.11)}$$

In an experiment of the noise measurement, the most accurate way to characterize noise is to measure it as a function of frequency. The noise spectral density (NSD) is the noise in a 1 Hz bandwidth plotted versus frequency f (Amps/$Hz^{1/2}$). The NSD is measured by a SR 770 spectrum analyzer. The bias and amplification gain are controlled by a low noise transimpedance amplifier (Keithley 428) and output voltage is measured by a spectrum analyzer.

6 Theoretical modeling of Quantum Dot infrared detectors

It is important to understand the correlations between the design parameters and the device characteristics. However, in order to make correlations between them, one needs to know what is going on inside the device and should have certain picture about physics of the device. In this section, the modeling of quantum dot infrared photodetector will be presented based on the semi-phenomenological theory. The energy levels and oscillator strengths calculation, responsivity, dark current and detectivity will be theoretically modeled. We will discuss one by one.

6.1 Energy levels and oscillator strength calculations

In order to design the detection wavelength of QDIPs, it is important to know the electronic energy levels of quantum dots and their possible transitions by absorption of the light. Actually, there are many literatures around explaining how to calculate the energy levels of quantum dots and their optical transitions. But the interband transitions between the states of electrons and those of holes have been intensely studied for the QD laser application.

But in the QDIPs, we deal with the only electrons because QDIP device is a unipoloar device unlike the QD laser which is a bipolar device where electrons and holes recombine inside the quantum dots.

There are several popular methods to calculate the electronic energy levels such as k·p method, pseudopotential calculation, and simple single-band effective mass envelope function method which is currently used in this work. First we will see how those methods work briefly

and will discuss our method, effective mass envelope function method, in detail. This method assumes many approximations and works only semi-phenomenological in terms of the device modeling. Before going to the modeling of the energy levels, we will start with quantum dots with infinite potential and simple geometries such as cube, sphere and cylinder.

6.1.1 k·p method and Empirical pseudopotential method

k·p method

The k·p method has been used to calculate the electronic band structure, including the energy band and the corresponding the wave function. Especially for optical devices, most semiconductors have direct band gaps, and many physical phenomena near the band edge are of great interest. Further the concept of the effective masses near a band extremum is very useful for heterostructures and nanostructures.

The basis of the method is to express the eigenfunctions as Bloch functions and to write a Schrödinger-like equation for its periodic part. We can begin with

$$\left\{\frac{\vec{p}^2}{2m_0}+V\right\}e^{i\vec{k}\cdot\vec{r}}u_{\vec{k}}(\vec{r})=E(\vec{k})e^{i\vec{k}\cdot\vec{r}}u_{\vec{k}}(\vec{r}) \qquad \text{Eq (6.1)}$$

where $u_{\vec{k}}(\vec{r})=u_{\vec{k}}(\vec{r}+\vec{R})$ which is the Bloch function and has a translational symmetry by $\vec{R}$. We can rewrite this in the following form

$$\left\{\frac{\left(\vec{p}+\hbar\vec{k}\right)^2}{2m_0}+V\right\}u_{\vec{k}}(\vec{r})=E(\vec{k})u_{\vec{k}}(\vec{r}) \qquad \text{Eq (6.2)}$$

We can expand the unknown periodic part $u_{\vec{k}}(\vec{r})$ on the basis of the corresponding solutions at a given point $\vec{k}_0$, which we label $u_{n,\vec{k}_0}(\vec{r})$

$$u_{\vec{k}}(\vec{r}) = \sum_n c_n(\vec{k}) u_{n,\vec{k}_0}(\vec{r}) \qquad \text{Eq (6.3)}$$

To solve the equation above, the Bloch function should be fed into the equations and it generates the matrix equation with the general element

$$A_{n,n'}(\vec{k}) = \left\langle u_{n,\vec{k}_0} \left| \frac{(\vec{p}+\hbar\vec{k})^2}{2m_0} + V \right| u_{n',\vec{k}_0} \right\rangle \qquad \text{Eq (6.4)}$$

Because $u_{n,\vec{k}_0}$ is an eigenfunction of Eq (6.2) for $\vec{k} = \vec{k}_0$ with energy $E_n(\vec{k}_0)$, we can rewrite Eq (6.4) into the simpler form

$$A_{n,n'}(\vec{k}) = \left\{ E_n(\vec{k}_0) + \frac{\hbar^2}{2m_0}(\vec{k}-\vec{k}_0)^2 \right\} \delta_{n,n'} + \frac{\hbar(\vec{k}-\vec{k}_0)}{m_0} \vec{p}_{n,n'}(\vec{k}_0) \qquad \text{Eq (6.5)}$$

where the matrix element $\vec{p}_{n,n'}(\vec{k}_0) = \left\langle u_{n,\vec{k}_0} \left| \vec{p} \right| u_{n',\vec{k}_0} \right\rangle$.

If we consider the energy band $E_n(\vec{k})$ which has an extremum at $\vec{k} = \vec{k}_0$, the last term of Eq (6.5) can be considered as a small perturbation and we can determine the difference $E_n(\vec{k}) - E_n(\vec{k}_0)$ by second order perturbation theory applied to the matrix $A(\vec{k})$. This leads to

$$E_n(\vec{k}) = E_n(\vec{k}_0) + \frac{\hbar^2}{2m_0}(\vec{k}-\vec{k}_0)^2 + \frac{\hbar^2}{m_0^2} \sum_{n' \neq n} \frac{\left[(\vec{k}-\vec{k}_0) \cdot \vec{p}_{nn'} \right] \left[(\vec{k}-\vec{k}_0) \cdot \vec{p}_{n'n} \right]}{E_n(\vec{k}_0) - E_{n'}(\vec{k}_0)} \qquad \text{Eq (6.6)}$$

which is the second order expansion near $\vec{k}_0$ leading to the definition of the effective masses. The effective masses m_α^* can be expressed in the following equation and α is the principal axe which represents x, y, and z.

$$\frac{m_0}{m_0^*} = 1 + \frac{2}{m_0} \sum_{n' \neq n} \frac{\left| (p_\alpha)_{nn'} \right|^2}{E_n(\vec{k}_0) - E_{n'}(\vec{k}_0)} \qquad \text{Eq (6.7)}$$

In Kane's model for direct band semiconductors[25], the spin-orbit interaction is taken into account. Four bands, which are the conduction, heavy-hole, light-hole and the spin-orbit split-off bands, are considered. Each band has double degeneracy with their spin counterparts.

The Hamiltonian near the zone center $\vec{k}_0 = 0$,

$$H = \frac{p^2}{2m_0} + V(\vec{r}) + \frac{\hbar}{4m_0^2 c^2} \vec{\sigma} \cdot \nabla V \times \vec{p} \qquad \text{Eq (6.8)}$$

where the third term accounts for the spin-orbit interaction, $\vec{\sigma}$ is the Pauli spin matrix. Here the detail of the eigenenergies and corresponding basis function will not be presented and can be found at ref. 26.

If only degenerate six valence bands would be considered in the calculation of the bandstructure ignoring the coupling to the two degenerate conduction bands with both spins, Luttinger-Kohn's model can be used. It is convenient to use Lödwin's perturbation method and treat the six valence bands in class A and put the rest of the bands in class B.

Now let's see how the k·p method can be applied to the nanostructure such as the quantum dot. With the k·p method and the envelope approximation, the wavefunction in each compositionally homogeneous region of the structure is assumed to be of the form

$$\Psi(\vec{r}) = \sum_n u_n(\vec{r})\phi_n(\vec{r}) \qquad \text{Eq (6.9)}$$

where the $u_n(\vec{r})$ are Bloch waves at $\vec{k} = 0$ for the material in a particular region[27]. The $\phi_n(\vec{r})$ are the envelope functions and the summation is restricted to bands close to the gap.

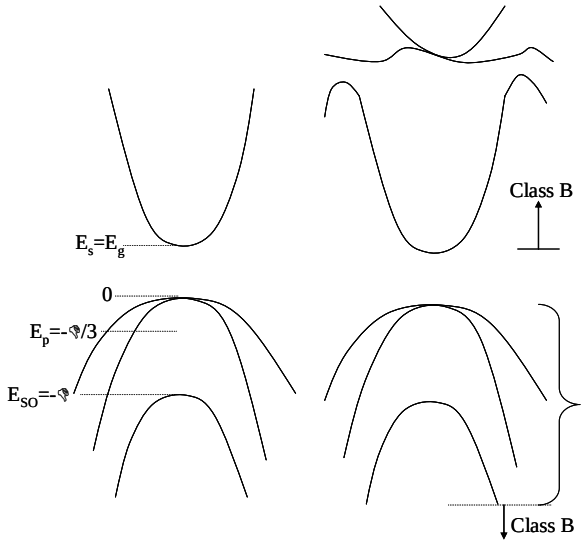

Figure 6.1. (a) The k·p method in Kane's model. Only a conduction band, a heavy hole, a light hole, and a spin-orbit split-off band with double degeneracy are considered. (b) Luttinger-Kohn's model. The heavy hole, light-hole, and spin-split off bands in double degeneracy are of interest and are called class A. All other bands are denoted as class B.

In case of multiband approximation, the envelope functions are governed by eight coupled differential equations with the basis of the eight Bloch waves. It can be expressed like the matrix equation,

$$\sum_n H_{mn}\phi_n(\vec{r}) = \varepsilon\phi_m(\vec{r}) \qquad \text{Eq (6.10)}$$

The eight Block waves are $|s\uparrow\rangle, |x\uparrow\rangle, |y\uparrow\rangle, |z\uparrow\rangle, |s\downarrow\rangle, |x\downarrow\rangle, |y\downarrow\rangle, |z\downarrow\rangle$ where the arrows indicate the spin, the matrix H can be Kane's 8×8 Hamiltonian. In the case of the strained structures, it is possible to add extra terms using deformation potentials which accounts for the variation of the band edge energies associated with elastic strains[28]. The envelope functions which are solutions of Eq (6.10) are expanded in 1D, 2D, and 3D Fourier series according to whether the system has spatial variation in 1D, 2D and 3D. After expansion of the envelope functions as Fourier series, Eq (6.10) is reduced to simple eigenvalue problem, which can be solved through the diagonalization. Another approach is to use a finite difference method to solve the differential equations[29]. The system is divided into different regions which define a mesh of perpendicular planes. The parameters of the Hamiltonian matrix are constant in each region but differ from region to region. Figure 6.2 shows the electron and hole wavefunctions InAs quantum dot with base lengths (b) 20.4 nm and 13.6 nm on GaAs resulting from multi-band 8×8 k·p method[29]. The drawbacks of k·p model, when applied to small quantum structures, are related to conceptually fixed number of Bloch functions which is usually eight, used for expanding the wave functions, the restriction to the Brillouin zone center Γ, the assumption of the same Bloch functions throughout the entire structure regardless of material and strain variations, the arbitrary of the matching conditions for the envelopes at heterointerfaces. These problems do not arise in microscopic theories like empirical pseudopotential theory.

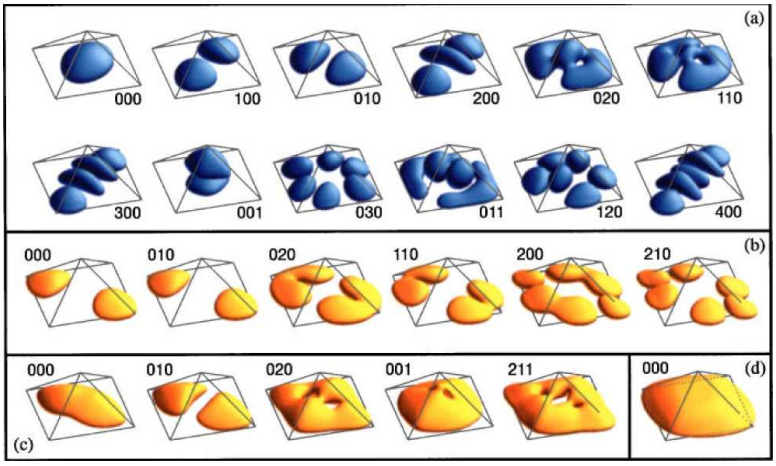

Figure 6.2. Probability density isosurfaces (p=65%) of (a) the electron and (b) the hole states for b=20.4 nm, the strain calculated using CM model. (c) Hole states for b=13.6 nm and strain calculated using the VFF model (d) Hole ground state for b=13.6 nm from effecibve mass calculation using VFF model form O. Stier et al[29].

Empirical Pseudopotential method

Compared to k·p method, Empirical Pseudopotential Method (EPM) is designed to make the best possible approximation to the bulk semiconductor Hamiltonian in the whole Brillouin zone. They involve adjustable parameters that are fitted to experimental data or ab initio band structure. Here we will discuss EPM briefly and how they can be applied to nanostructures.

Suppose one has a periodic solid in which the electrons can safely be divided into two groups, the core states and the conduction states. The core states are localized around particular atomic states. The core states are likely to be quite similar to what they are in the free atom. Thus the use of the full atomic potential in a band calculation is likely to lead to unnecessary computational complexity since the basis state will have to be chosen in such a way that they describe localized states and extended states at the same time. Therefore, it is of much interest to

devise a method which allows us to eliminate the core states, focusing only on the conduction states of interest which are easier to describe. By doing this, the true potential in Schrödinger's equation is replaced with the pseudopotential $V(\vec{G})$. There is some price to be paid for this simplification. The pseudopotential is nonlocal which means one has to perform integrals in order to compute its action upon a general state. One example of EPM is the empty-core potential due to Ashcroft[30]. There are three free parameters of this potential which are its magnitude, the cutoff and the exponential decay length. They can be adjusted to fit measurements taken from optical or magnetic experiments. The application of the EPM to semiconductor nanostructures has been mainly developed by the group of A. Zunger[31,32].

6.1.2 Single-band Effective mass envelope function method

The simplest model for the quantum dot energy level calculation is when a quantum dot is surrounded by infinite potential barrier. Of course this is not realistic, but gives a general idea about the discrete energy levels and other properties. The wavefunctions of a quantum dot surrounded by infinite potential barrier are used for the basis functions of the single-band finite potential problem. The solutions to the fundamental box problems are presented here in the case of the rectangular box, the cylindrical box and the spherical box.

6.1.2.1 Rectangular box with infinite potential barrier

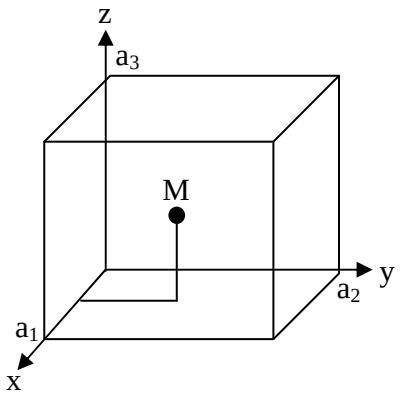

Figure 6.3. One particle inside a rectangular infinite potential box.

The edge lengths of the rectangular box have a_1, a_2, and a_3. The Hamiltonian is given as

$$\hat{H} = \frac{1}{2M}\left(\hat{p}_x^2 + \hat{p}_y^2 + \hat{p}_z^2\right) \qquad \text{Eq (6.11)}$$

where $\hat{p}_x^2 = \left(-i\hbar\frac{\partial}{\partial x}\right)^2$, $\hat{p}_y^2 = \left(-i\hbar\frac{\partial}{\partial y}\right)^2$, and $\hat{p}_z^2 = \left(-i\hbar\frac{\partial}{\partial z}\right)^2$

Solving Hamiltonian with proper boundary conditions ($\sin k_q a_1 = \sin k_s a_2 = \sin k_t a_3 = 0$) results in the wave equation for x, y and z direction, wavefunctions and eigenenergies.

$$\left(\frac{d^2}{dx^2} + k^2\right)\sin kx = 0 \qquad \text{Eq (6.12)}$$

$$\psi_{qst}(x,y,z) = \sqrt{\frac{8}{a_1 a_2 a_3}}\sin k_q x \sin k_s y \sin k_t z \qquad \text{Eq (6.13)}$$

$$E_{qst} = \frac{\hbar^2}{2M}\left(k_q^2 + k_s^2 + k_t^2\right) \qquad \text{Eq (6.14)}$$

where $k_q = \frac{l\pi}{a_1}, k_s = \frac{m\pi}{a_2}, k_t = \frac{n\pi}{a_3}$ and *l*, *m* and *n* are integer numbers.

6.1.2.2 Cylindrical box with infinite potential barrier

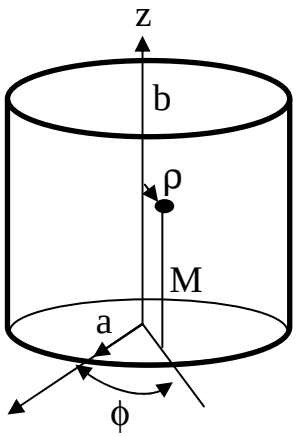

Figure 6.4. One particle inside a cylindrical infinite potential box.

The cylindrical has radius *a* and height *b*. The Hamiltonian has the cylindrical symmetry which is azimuthal around z axis and is given as

$$\hat{H} = \frac{1}{2M}\left(\hat{p}_\rho^2 + \hat{p}_z^2 + \frac{L_z^2}{\rho^2}\right) \qquad \text{Eq (6.15)}$$

where $\hat{p}_\rho^2 = -\hbar^2 \frac{1}{\rho}\frac{\partial}{\partial\rho}\left(\partial\frac{\partial}{\partial\rho}\right)$ and $\hat{L}_z^2 = -\hbar^2 \frac{\partial^2}{\partial\phi^2}$.

The boundary condition for this problem is

$$\sin k_q b = J_m(K_{mn} a) = 0 \qquad \text{Eq (6.16)}$$

where J_m is the m-th order of Bessel function and K_{mn} is the n-th zero of J_m.

The Bessel function is a solution of the Bessel equation. The Bessel equation is written as

$$\left[\frac{1}{x^2}\left(x\frac{d}{dx}\right)^2 + 1 - \frac{m^2}{x^2}\right] J_m(x) = 0 \qquad \text{Eq (6.17)}$$

After solving the Hamiltonian with the boundary condition above, the eigenfunctions and eigenenergies can be calculated as follows.

$$\psi_{qmn}(x,y,z) = \sqrt{\frac{2}{\pi b\left[aJ'_m(K_{mn}a)\right]^2}} J_m(K_{mn}\rho)\sin k_q z e^{im\phi} \qquad \text{Eq (6.18)}$$

$$E_{qmn} = \frac{\hbar^2}{2M}\left(K_{mn}^2 + k_q^2\right) \qquad \text{Eq (6.19)}$$

6.1.2.3 Spherical Box with infinite potential barrier

The sphere has radius *a* and is surrounded by infinite potential barrier. The electron or any particle cannot penetrate into the wall. Due to the spherical symmetry, the Hamiltonian has angular momentum operator which is

$$\hat{L}^2 = -\hbar^2\left[\frac{1}{\sin\theta}\frac{\partial}{\partial\theta}\left(\sin\theta\frac{\partial}{\partial\theta}\right) + \frac{1}{\sin^2\theta}\frac{\partial^2}{\partial\phi^2}\right] \qquad \text{Eq (6.20)}$$

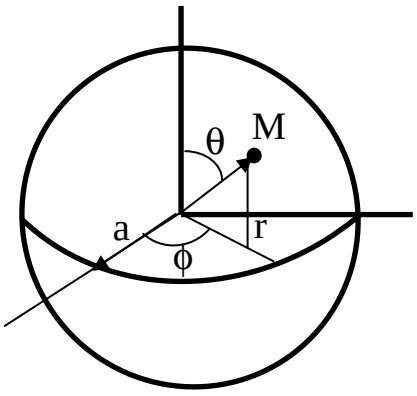

Figure 6.5. One particle inside a spherical infinite potential box.

The Hamiltonian is given by

$$\hat{H} = \frac{1}{2M}\left(\hat{p}_r^2 + \frac{\hat{L}^2}{r^2} \right) \qquad \text{Eq (6.21)}$$

where $\hat{p}_r^2 = -\hbar^2 \left(\frac{1}{r}\frac{\partial}{\partial r} r \right)^2$. This Hamiltonian becomes the Spherical Bessel Function as follows,

$$\left[\left(\frac{1}{x}\frac{d}{dx} x \right)^2 + 1 - \frac{l(l+1)}{x^2} \right] j_l(x) = 0 \qquad \text{Eq (6.22)}$$

and the boundary condition is $j_l(k_{\ln} a) = 0$. This boundary condition results in the eigenenergy which is $E_{nl} = \frac{\hbar^2 k_{nl}^2}{2M}$. Finally the eigenfunctions are following.

$$\psi_{nlm}(x, y, z) = \sqrt{\frac{2}{a^3 \left[j_l'(k_{\ln} a) \right]^2}}\, j_l(k_{\ln} r) Y_l^m(\theta, \phi) \qquad \text{Eq (6.23)}$$

where $Y_l^m(\theta, \phi)$ is normalized spherical harmonics.

6.1.2.4 Arbitrary shape with finite potential barrier

k·p method and pseudopotential methods have been used to calculate the energy levels of quantum dots. But those calculations cannot be performed easily because of the finite potential confining barrier and the nontrivial geometry of the dot. The Schrödinger's equation must be solved numerically. Due to the nontrivial geometry of the quantum dots the calculations based on k·p method and pseudopotential methods require a lot of computational resources and time. For the design of the real device of QDIP, it is desirable to have such a tool that the energy levels and their transitions can be easily calculated and can be applied to the design of the device structure. The process between the design and the growth should be quick. As a further approximation to

multi-band effective mass theory, the single-band effective mass envelope function method can be used for the energy levels of quantum dots.

Gershoni et al.[33] developed a numerical method in which they expand the envelope function of a rectangular quantum wire which is 2D confined system using a complete orthonormal set (COS) of periodic functions, which are solutions for a rectangular wire with an infinite barrier height and suitably chosen dimensions. The advantage of this method is that it can be applied to structures of arbitrary shape. Moreover, all the matrix elements can be calculated analytically. Gangopadhyay and Nag[34] extended this method to study 3D confined structures such as pararellepipeds and cylinders.

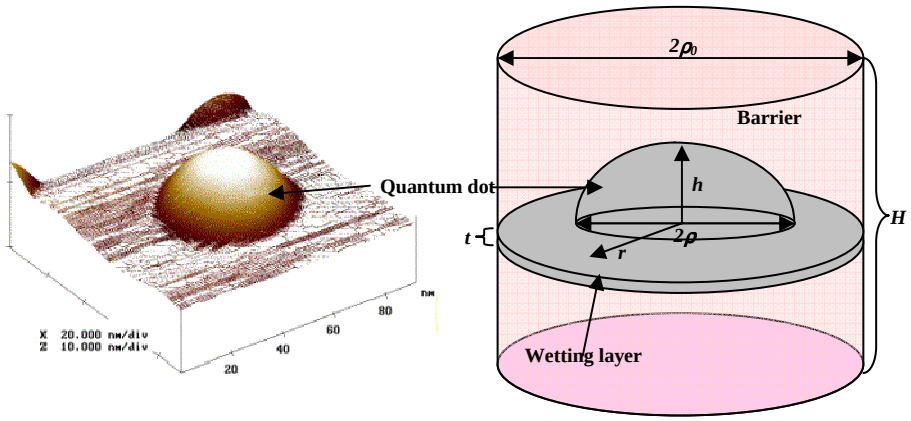

Figure 6.6. (left) AFM image of uncapped InAs quantum dot on InP, (right) the calculation model of a capped quantum dot.

The aim of this section is to extend Gershoni et al's method to determine the energy levels of current quantum dots we are discussing.

InGaAs QD on InGaP and InAs QD on InP grown by MOCVD have lens-like shape like Figure 6.6. In order to model the quantum dot energy levels, it is necessary to simplify the geometry of

quantum dots into perfect lens shape like Figure 6.6 (right). The quantum dot is varied inside the barrier cylinder which has infinite potential wall. The size of the barrier cylinder should be independent of the calculation results when it is bigger than certain size. Usually the size of the barrier cylinder is that 4 times QD height is height of the cylinder and 4 times QD radius is the radius of the cylinder. The dimensions of lens-shape quantum dot are usually taken from AFM (atomic force microscope) measurement. For example, one of InAs QD on InP is shown in Figure 6.6 (left).

The Schrödinger's equation for the envelope function in the effective mass approximation can be written as

$$-\frac{\hbar^2}{2}\left(\nabla\frac{1}{m^*(x,y,z)}\nabla\right)\Psi(x,y,z)+V(x,y,z)\Psi(x,y,z)=E\Psi(x,y,z) \qquad \text{Eq (6.24)}$$

We can convert the above Schrödinger's equation into the following equation

$$-\left(\nabla\frac{1}{m^*(\vec{r})}\nabla\right)\Psi(\vec{r})+V(\vec{r})\Psi(\vec{r})=E\Psi(\vec{r}) \qquad \text{Eq (6.25)}$$

The unit length is the Borh radius a_0 ($=\hbar^2/m_e^2$) 0.529 Å and the unit energy is the Rydberg constant Ry ($= m_e e^4/2\hbar^2$) 13.6 eV. This Schrödinger's equation is Hermitian and its wavefunctions are orthogonal and the probability current is conserved at the interface of the heterojunction. The envelope function of the quantum dot with a lens shape $\Psi(x,y,z)$, is then expanded in terms of a complete orthonormal set of solutions $\psi_{lmn}(x,y,z)$ of the cylindrical problem with infinite barrier height (see Eq (6.18)).

$$\Psi(x,y,z)=\sum_{lmn}a_{lmn}\psi_{lmn}(x,y,z) \qquad \text{Eq (6.26)}$$

$$\psi_{lmn}(x,y,z)=\sqrt{\frac{2}{H\pi\left[\rho_0 J_{m+1}(k_{mn}\rho_0)\right]^2}}J_m(k_{mn}r)\sin\left[l\pi\left(\frac{1}{2}-\frac{z}{H}\right)\right]e^{im\phi} \qquad \text{Eq (6.27)}$$

The boundary condition is $J_m(k_{mn}\rho_0)=0$. We have chosen the domains [-H/2,H/2] and [0,ρ_0] for the variation z and r. This approach does not need explicit matching wavefunctions across the boundary between the barrier and dot materials. This method is easily applicable to an arbitrary confining potential. Substituting Eq (6.26) into Eq (6.25), multiplicating on the left by $\psi^*_{l'm'n'}$, and finally integrating over the cylinder, yields the matrix equation

$$(A_{lmnl'm'n'}-E\delta_{mm'}\delta_{nn'}\delta_{ll'})a_{lmn}=0 \qquad \text{Eq (6.28)}$$

The matrix element $A_{lmnl'm'n'}$ are given by

$$A_{lmnl'm'n'}=-\int_{Cylinder}\psi^*_{l'm'n'}(\vec{r})\left(\nabla\frac{1}{m^*(\vec{r})}\right)\psi_{lmn}(\vec{r})d\upsilon + \int_{Cylinder}\psi^*_{l'm'n'}(\vec{r})V(\vec{r})\psi_{lmn}(\vec{r})d\upsilon \qquad \text{Eq (6.29)}$$

This integration should be done in the quantum dot and wetting layer. The barrier potential $V(\vec{r})$ is zero inside the quantum dot and V_0 outside the quantum dot. The effective mass $m^*(\vec{r})$ is m_w inside QD and m_b outside QD. If we integrate the first term of Eq (6.29) by part,

$$A_{lmnl'm'n'}=\int_{Cylinder}\nabla\psi^*_{l'm'n'}(\vec{r})\frac{1}{m^*(\vec{r})}\nabla\psi_{lmn}(\vec{r})d\upsilon + \int_{Cylinder}\psi^*_{l'm'n'}(\vec{r})V(\vec{r})\psi_{lmn}(\vec{r})d\upsilon \qquad \text{Eq (6.30)}$$

The problem in above equation is the discontinuity of effective mass in passing from the well region into barrier region. In order to overcome this problem, the integral can be split into three parts, within each of which the effective mass is constant[35]. First we take an integral with

$m^* = m_B$ over the whole cylinder which also includes the quantum dot and wetting layer (the well region). Second, we subtract the integral with $m^* = m_B$ over the well region and third, we add the integral with $m^* = m_W$ over the well region. The same procedure has been adopted for the integral containing the potential. The final expression for the matrix element is

$$\begin{aligned} A_{lmnl'm'n'} = & \frac{1}{m_B} \int_{Cylinder} \nabla \psi^*_{l'm'n'}(\vec{r}) \nabla \psi_{lmn}(\vec{r}) d\upsilon \\ & + \left(\frac{1}{m_W} - \frac{1}{m_B} \right) \int_{QD+WL} \nabla \psi^*_{l'm'n'}(\vec{r}) \nabla \psi_{lmn}(\vec{r}) d\upsilon \\ & - V_0 \int_{QD+WL} \psi^*_{l'm'n'}(\vec{r}) \psi_{lmn}(\vec{r}) d\upsilon \\ & + V_0 \delta_{ll'} \delta_{mm'} \delta_{nn'} \end{aligned} \qquad \text{Eq (6.31)}$$

The first term of Eq (6.31) is simply the free particle energy inside a cylinder. After replacing the first term with free particle energy, the matrix element becomes

$$\begin{aligned} A_{lmnl'm'n'} = & \left[\frac{1}{m_B} \left(k^2_{mn} + \left(\frac{\pi l}{H} \right)^2 \right) + V_0 \right] \delta_{ll'} \delta_{mm'} \delta_{nn'} \\ & + \left(\frac{1}{m_W} - \frac{1}{m_B} \right) \int_{QD+WL} \nabla \psi^*_{l'm'n'}(\vec{r}) \nabla \psi_{lmn}(\vec{r}) d\upsilon \\ & - V_0 \int_{QD+WL} \psi^*_{l'm'n'}(\vec{r}) \psi_{lmn}(\vec{r}) d\upsilon \end{aligned} \qquad \text{Eq (6.32)}$$

where the subscript QD+WL in the integrals means that the integration is over the quantum dot and wetting layer inside a cylinder. In order to calculate the matrix elements $A_{lmnl'm'n'}$, the integrals need to be calculated over the quantum dot and wetting layer. But these volume integrations can be done analytically for the lens shape geometry. For the volume integration, we need find the relation between the height and the radius of lens shaped quantum dot. If we imagine the big sphere whose part is lens shaped quantum dot, the height at any position r from the origin in the

lens can be calculated with other geometry factors such as R and ρ (see Figure 6.7). The integrations over the quantum dot and wetting layer can be separate in the following way.

$$\int_{QD+WL} \nabla \psi^*_{l'm'n'}(\vec{r}) \nabla \psi_{lmn}(\vec{r}) d\upsilon = \int_{QD} \nabla \psi^*_{l'm'n'}(\vec{r}) \nabla \psi_{lmn}(\vec{r}) d\upsilon + \int_{WL} \nabla \psi^*_{l'm'n'}(\vec{r}) \nabla \psi_{lmn}(\vec{r}) d\upsilon \qquad \text{Eq (6.33)}$$

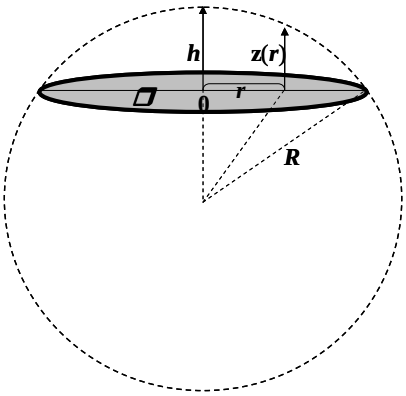

Figure 6.7. The geometry of lens shaped quantum dot for the calculation. At the distance r from the origin 0, the height z(r) at r is given by $\sqrt{R^2 - r^2} - \sqrt{R^2 - \rho^2}$.

The first term of the right hand side of Eq (6.33) becomes

$$\int_{QD} \nabla \psi^*_{l'm'n'}(\vec{r}) \nabla \psi_{lmn}(\vec{r}) d\upsilon = \int_0^{\rho} dr \left[r \frac{dR^*_{n'm}}{dr} \frac{dR_{nm}}{dr} F_{l'l}(z(r)) + \frac{m^2}{r} R^*_{n'm} R_{nm} F_{l'l}(z(r)) + \frac{ll'\pi^2}{H^2} r R^*_{n'm} R_{nm} G_{ll'}(z(r)) \right] \delta_{mm'} \qquad \text{Eq (6.34)}$$

Here $R_{nm}(r)$ is the radial part of a basis function $\psi_{lmn}(\vec{r})$,

$$R_{nm}(r) = \frac{\sqrt{2}}{\rho_0 J_{m+1}(k_{mn}\rho_0)} J_m(k_{mn} r) \qquad \text{Eq (6.35)}$$

$F_{l'l}(z)$ and $G_{ll'}(z)$ are integrals over the height $z(r) = \sqrt{R^2 - r^2} - \sqrt{R^2 - \rho^2}$ and are expressed by

$$F_{ll'}(z(r)) = \frac{2}{H}\int_0^{z(r)} dz' \sin\left[l'\pi\left(\frac{1}{2} - \frac{z'}{H}\right)\right] \sin\left[l\pi\left(\frac{1}{2} - \frac{z'}{H}\right)\right]$$

$$G_{ll'}(z(r)) = \frac{2}{H}\int_0^{z(r)} dz' \cos\left[l'\pi\left(\frac{1}{2} - \frac{z'}{H}\right)\right] \cos\left[l\pi\left(\frac{1}{2} - \frac{z'}{H}\right)\right] \qquad \text{Eq (6.36)}$$

The same procedure can be applied to the last integral of Eq (6.32). The integration over the wetting layer is relatively straightforward because the geometry of the wetting layer is simply the thin cylinder.

Before diagonalizing the matrix, we can notice that the matrix is block-diagonal and symmetrical.

$$A_{lmnl'm'n'} = A_{l|m|nl'|m|n'}\, \delta_{mm'} \qquad \text{Eq (6.37)}$$

$$A = \begin{bmatrix} \ldots & 0 & 0 & 0 & 0 & 0 & 0 \\ 0 & (m=-2) & 0 & 0 & 0 & 0 & 0 \\ 0 & 0 & (m=-1) & 0 & 0 & 0 & 0 \\ 0 & 0 & 0 & (m=0) & 0 & 0 & 0 \\ 0 & 0 & 0 & 0 & (m=1) & 0 & 0 \\ 0 & 0 & 0 & 0 & 0 & (m=2) & 0 \\ 0 & 0 & 0 & 0 & 0 & 0 & \ldots \end{bmatrix} \qquad \text{Eq (6.38)}$$

and

$$A^m = (m) = (-m) \qquad \text{Eq (6.39)}$$

$$A^{m}_{l\,n\,l'\,n'} \quad = \quad A^{m}_{l'\,n'\,l\,n}$$

The eigenvectors will be called according to m which refers to the number m of φ_{lmn} (angular moment of the fictitious particle represented by φ_{lmn}) and an extra quantum number p (p increases with the energy for constant m):

$$\varsigma_{mp} \quad = \quad \sum_{l\,n} a^{p}_{lmn}\, \varphi_{lmn} \qquad \text{Eq (6.40)}$$

In this work, we do not have to take φ_{lmn} of high energy for our computation. Here we took $l \in \{1,2,\ldots,20\}$ and $n \in \{1,2,\ldots,20\}$ since we are interested only in bound states. For m we took $m \in \{0,1,2\}$ because the matrix remains unchanged by the transformation $m \rightarrow -m$.

We have used 20 sine functions and 20 Bessel functions as basis functions for expanding the envelope functions. Eq (6.44) is 400×400 matrix for each m and it can be solved numerically. The program was made in C-language and the diagonalization was made by MatLab (See Appendix).

This method which we have discussed is not the most accurate of the available methods[36,37], but the advantage is that it is simple to use, versatile, and good enough for our modeling for QDIPs.

For the example, we calculated the energy levels and wavefunctions of the InGaAs QD whose height is h_{QD} = 4 nm and radius r_{QD} = 20 nm. The InGaAs QDs are surrounded with InGaP barrier. Underneath is a small wetting layer, whose height is h_{WL} = 1.5 monolayers (0.44 nm). The effective mass of the dot and wetting layer was assumed to be equal to $0.05m_e$. The potential was taken equal to -0.7 eV. Outside the well is the InGaP barrier, whose effective mass was $0.11m_e$ and potential was zero.

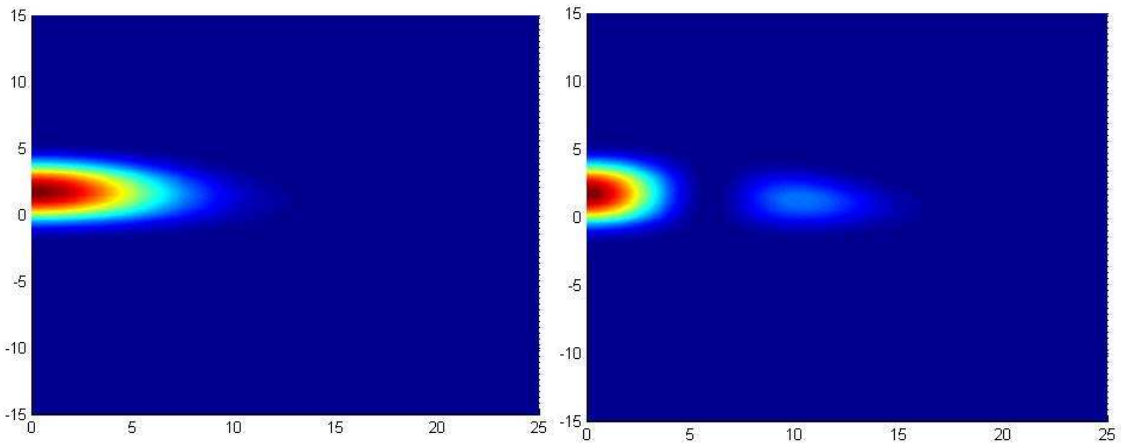

Figure 6.8. Electronic wavefunctions of the InGaAs QD whose height is h_{QD} = 4 nm and radius r_{QD} = 20 nm and which is surrounded by InGaP barrier. (Left) $|m=0, p=1\rangle, E=-0.5206\,eV$; (Right) $|m=0, p=2\rangle, E=-0.4359\,eV$.

The size of the cylinder which delimitated the space available for the electron was taken big enough to avoid the boundary condition effect: R_C = 80 nm and H_C = 16 nm (the picture is not at scale).

As expected the quantum number p gives the number -1 of nodes for the wavefunctions as shown in Figure 6.8 and Figure 6.9. The angular moment due to the term in $e^{im\theta}$ cannot be seen with this representation. It corresponds to the rotation of the particle around the z-axis.

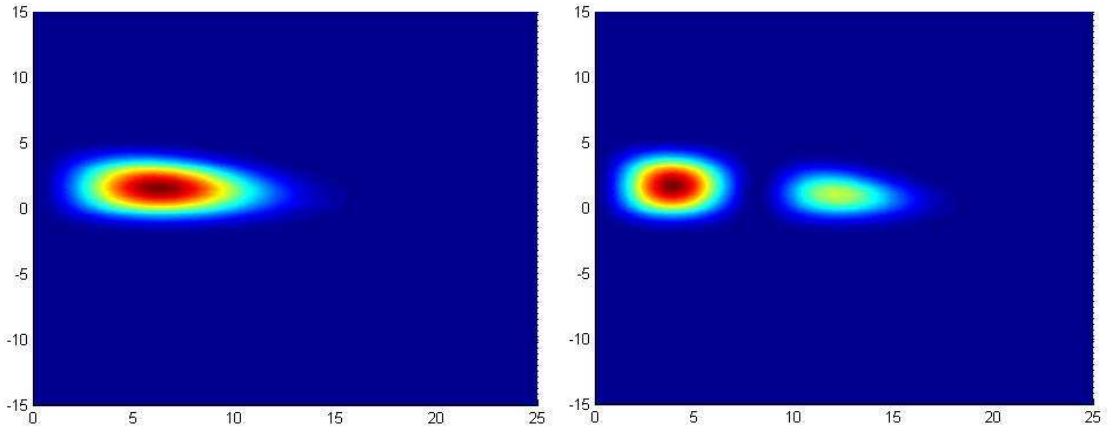

Figure 6.9. Electronic wavefunctions of the InGaAs QD whose height is h_{QD} = 4 nm and radius r_{QD} = 40 nm and which is surrounded by InGaP barrier. (Left) $|m=\pm1, p=1\rangle, E=-0.4810\ eV$; (Right) $|m=\pm1, p=2\rangle, E=-0.3885\ eV$.

We can see incoherence when energy levels are too close to zero (energetical edge of the Quantum Dot): for instance the wavefunction |m=±2,p=4> behaves strangely in Figure 6.10. This is due to two reasons:

- The number of basis functions chosen for the computation: the higher the energy is, the more basis function is needed
- The size of the cylinder: because the energy is close to the zero potential (free particle) and so to the continuum, the linear combination Eq (6.44) has non-negligible coefficient for the (l, m, n) triplet of the continuum. But this is not a real continuum due to the boundary conditions (cylinder), and this can cause inaccuracy for particle whose energy is close to the one of a free particle.

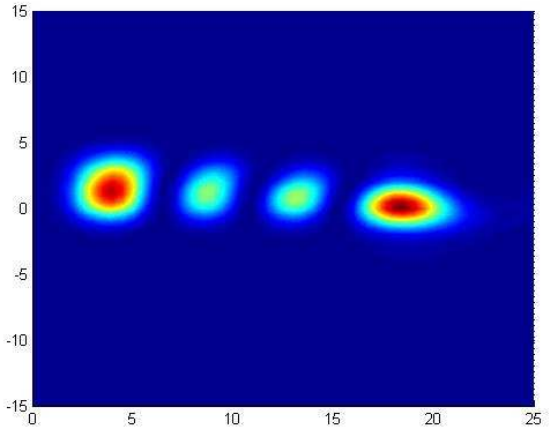

Figure 6.10. Electronic wavefunction of the InGaAs QD whose height is h_{QD} = 4 nm and radius r_{QD} = 40 nm and which is surrounded by InGaP barrier. $|m = \pm 2, p = 4\rangle, E = -0.0815\ eV$.

6.1.3 Oscillator strength

In order to calculate the optical absorption spectrum or analyze the photocurrent spectrum in the QDIP, one requires the energy levels and the oscillator strengths for transitions between the various energy levels. The oscillator strength is the measure of the interaction between the light and electrons. When the incoming light enters the quantum dots, the electrons in the discrete energy levels gain the energy and experience dipole transitions. The rate of the dipole transition can be obtained from the Fermi Golden rule. The oscillator strength for a transition from a level i to a level j is given by

$$f_{ij} = 2\left|\langle i|\vec{\eta}\cdot\vec{p}|j\rangle\right|^2 \Big/ \left(m^*\hbar\omega_{ij}\right) \qquad \text{Eq (6.41)}$$

where $|i\rangle$ and $|j\rangle$ are wavefunctions of the quantum dot, $\vec{\eta}$ is the photon polarization, $\vec{p}$ is the electron momentum operator, and ω_{ij} is the transition frequency. It may be noted that a spherical QD of cubic material is optically isotropic, and the oscillator strength is polarization

independent. In reality, the quantum dot has asymmetric shape and therefore the oscillator strength of quantum dot has strong dependence of polarization. For the normal incidence of the light, which is perpendicular to the growth plane, the incoming light has in-plane polarization (or s-polarization) which is parallel to the growth plane. If the quantum dot has rotational symmetry, the wavefunction of quantum dot also has rotation symmetry. In such a case, the in-plane coordinates such as x and y do not make difference. For the x-polarization (or s-polarization), $\vec{\eta} \cdot \vec{p}$ is $-i\hbar\partial/\partial x$ and for the z-polarization, it is $-i\hbar\partial/\partial z$. In order to calculate the oscillator strength numerically, it is necessary to know the wavefunctions and their derivatives. In a later chapter, the results of the calculation of the oscillator strength for the quantum dots in our QDIPs will be discussed.

6.2 Absorption

The absorption of the light in the QDIPs mostly happens in the quantum dots. The absorption coefficient $\alpha(\omega)$ can be written as

$$\alpha = \frac{\pi\hbar N_d n_{op} e^2}{m^* \varepsilon \varepsilon_0 c} \left[\frac{\Gamma}{\left(\hbar\omega - E_{eg}\right)^2 + \Gamma^2} \right] n_g \left(1 - n_e\right) f_{ge} \qquad \text{Eq (6.42)}$$

where n_{op} is the refractive index, c is the velocity of light, Γ is the total level width. The absorption coefficient also involves the following quantities: i) the dot density $N_{d,}$ ii) the oscillator strength f_{ge}, and iii) the probability n_g that the carriers remain in the initial state and the probability n_e that the carriers stay in the excited state. As you can see, the absorption can be increased by increasing the dot density and the oscillator strength and maximizing $n_g(1- n_e)$. In order to increase the dot density, the growth condition of the quantum dot should be optimized.

Increasing the oscillator strength is not simple problem. The occupation probabilities n_g and n_e can be calculated if the energy levels of the quantum dot are known. Assuming Boltzmann statistics for convenience, n_g can be written

$$n_g = \frac{e^{-E_g/kT}}{\sum_s d_s e^{-E_s/kT} + \sum_t e^{-E_t} + \int_{\varepsilon_c} d\varepsilon \rho(\varepsilon) f(\varepsilon)/N_d} \qquad \text{Eq (6.43)}$$

where the E_s are the quantum dot energy levels, d_s the degeneracy, the "t" sum is over traps including the new eigenstates formed by electron phonon resonances; $\rho(\varepsilon)$ is the band density of states and $f(\varepsilon)$ the Fermi function. As we can see, the absorption of the quantum dot depends on the occupation probabilities of the levels. Experimentally these occupation probabilities can be controlled through the doping of the quantum dot.

6.3 Modeling of Responsivity and photocurrent

When the incoming infrared light is absorbed in the QDIP, the electrons are generated in the QDIP and the electrons can be collected as a photocurrent under the bias. After absorption of the light by quantum dots, the excited electrons should come out of quantum dots to be detected. This escape process involves tunneling and thermal activation. If R is the responsivity as a function of temperature T and applied bias V, then the photocurrent I_P flowing is given by

$$I_P = AR(T,V)P_L \qquad \text{Eq (6.44)}$$

where P_L is the optical power per unit area, and A is the illuminated area of the device. Collecting together the terms, we can write the peak responsivity apart from a wavelength dependent constant $e/\hbar\omega$, in terms of three varying factors

$$R = \left[\frac{e\alpha(\omega)L}{\hbar\omega}\right] g \left[\frac{\nu_{ec} e^{-E_{eff}/kT}}{\nu_0 + \nu_{ec} e^{-E_{eff}/kT} + \nu_t e^{-\Delta/kT}}\right] \qquad \text{Eq (6.45)}$$

or also in terms of the quantum efficiency η as

$$R = \frac{eg\eta}{\hbar\omega} \qquad \text{Eq (6.46)}$$

We can define the quantum efficiency η

$$\eta = \alpha L \left[\frac{\nu_{ec} e^{-E_{eff}/kT}}{\nu_0 + \nu_{ec} e^{-E_{eff}/kT} + \nu_t e^{-\Delta/kT}}\right] \qquad \text{Eq (6.47)}$$

where the first factor αL is the absorbance, L is the device length, and α(ω) the absorption coefficient. The second factor in Eq (6.45)is the gain "g" defined as the ratio of the recombination time over the transit time,

$$g = \frac{\mu F}{L C_{be}} \qquad \text{Eq (6.48)}$$

where μF/L is the transit time, and C_{be} the capture rate of electrons from the continuum band into the bound excited state of the quantum dot. The third factor in Eq (6.45) is the ratio of the escape rate $W_{ec}(= \nu_{ec} \exp[-E_{eff}/kT])$ out of the excited state to the continuum and the inverse lifetime of the excited state (ν_0). In this section, we will concentrate on the third factor of Eq (6.45) which is related to the escape rate and the quantum efficiency and gain will be discussed in a later section.

6.3.1 Escape rate

In the quantum dot, the electron can tunnel out back to the extended state outside the quantum dot if the electric field is applied. Transmission out of the dot through a triangular barrier which is created by an electric field, known as Fowler-Nordheim tunneling is given as following.

$$T = \exp\left[-\frac{2}{\hbar}\int_0^x \sqrt{2m(E_{ec} - eFx')}dx'\right] \qquad \text{Eq (6.49)}$$

Another process involved for the escape process is thermal activation. In Figure 6.11, the physical picture is that (1) the electron in the excited state can thermally activate to the continuum state or (2) directly tunnel out or (3) thermally activate and tunnel to continuum state. In order to estimate the escape rate, the sum of all the possible paths should be required.

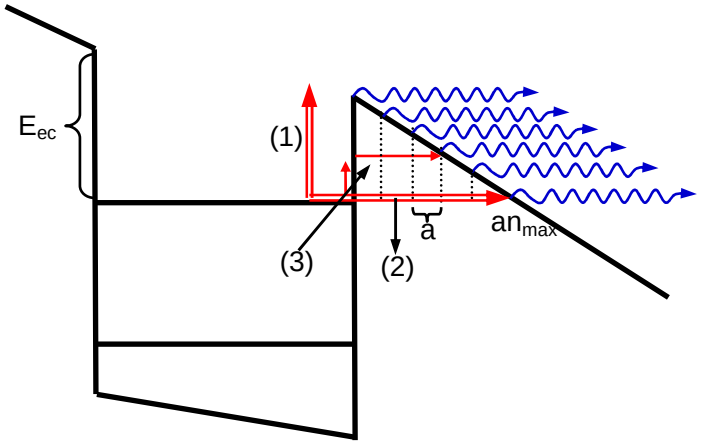

Figure 6.11. Escape paths out of the excited state to the continuum state.

If the longest tunneling path is divided into a lattice constant a, the possible escape occurs at the point whose distance from the well is multiple lattice constants (na) (Figure 6.11).

The escape rate through one path is given by

$$W_{0n} = \nu_{ec} \exp\left[-2\gamma\int_0^{na}\sqrt{(E_{ec}-eFx')}dx'\right]\exp\left(-\frac{E_{ec}-eFna}{kT}\right) \qquad \text{Eq (6.50)}$$

where ν_{ec} is the attempt frequency, F is the applied electric field, $\gamma = \sqrt{2m^*}/\hbar$ and E_{ec} is the height of the escape barrier. The total escape rate is the sum of the all the escape rates through each path. The limit of the summation (n_{max}) is determined by F and E_{ec} ($n_{max}a=E_{ec}/eF$).

$$\sum_0^{n_{\max}} W_{0n} = \sum_0^{\infty} W_{0n} - \sum_{n_{\max}+1}^{\infty} W_{0n} \qquad \text{Eq (6.51)}$$

It is possible to calculate the exact summation numerically with the left hand side of Eq (6.51) but the analytic form can be obtained assuming some approximations. The First part of the right hand side of Eq (6.51) can be approximated if the electric field F is not strong and the perturbation is used. The approximation is

$$\exp\left[-2\gamma\int_0^{a}\sqrt{(E_{ec}-eFx')}dx'\right] \approx \exp\left[-2\gamma a E_{ec}^{1/2}\right] \qquad \text{Eq (6.52)}$$

Then the infinite series can be done and the first part is

$$\sum_0^{\infty} W_{0n} = \frac{\exp[-E_{ec}/kT]}{1-\exp[-2\gamma a E_{ec}^{1/2}]\exp\left[eFa/kT\right]} \qquad \text{Eq (6.53)}$$

With another approximation,

$$\begin{aligned}
&\exp\left[-2\gamma\int_0^{(n_{\max}+1)a}\sqrt{(E_{ec}-eFx')}dx'\right] \\
&\approx \exp\left[-2\gamma a E_{ec}^{1/2}\right]\exp\left[-2\gamma\int_0^{n_{\max}a}\sqrt{(E_{ec}-eFx')}dx'\right] \\
&= \exp\left[-2\gamma a E_{ec}^{1/2}\right]\exp\left[-\frac{4\gamma E_{ec}^{3/2}}{3eF}\right]
\end{aligned} \qquad \text{Eq (6.54)}$$

The second part becomes

$$\sum_0^\infty W_{0n} = \frac{\exp[-2\gamma a E_{ec}^{1/2}]\exp[-4\gamma E_{ec}^{3/2}/3eF]\exp[eFa/kT]}{1-\exp[-2\gamma a E_{ec}^{1/2}]\exp[eFa/kT]} \qquad \text{Eq (6.55)}$$

Finally the escape rate is given by

$$\begin{aligned} W_{ec} &= \nu_{ec}\exp[-E_{eff}(F)/kT] \\ &= \nu_{ec} g_c \frac{\exp[-E_{ec}/kT]-\exp[-2\gamma a E_{ec}^{1/2}]\exp[-4\gamma E_{ec}^{3/2}/3eF]\exp[eFa}{1-\exp[-2\gamma a E_{ec}^{1/2}]\exp[eFa/kT]} \end{aligned} \qquad \text{Eq (6.56)}$$

where g_c is the density of final states of escaping charge at the band edge which is reachable within kT. ν_{ec} varies between a) the value of a phonon frequency multiplied by the probability of finding the charge at a given site in the quantum dot localized state, giving ν_{ec} ~10^9 to 10^{10} Hz, and b) the excited state pure tunneling attempt frequency ~E_{ec}/h. g_c is given by g_c~$10^4(kT/e)^{3/2}$ ~10, assuming three dimensional plane wave like states. Even though clearly ν_{ec} is not a constant but depends on the path chosen, we shall assume that the product $\nu_{ec}g_c$ is a fit parameter varying between 10^{10} and 10^{13} Hz.

So far the responsivity has been modeled by the absorption, the gain and the escape rate. Later we will compare the theoretical modeling and experimental data and discuss the results in chapter 7.2.

6.4 Dark current

Let us consider now the dark current dynamics[38,39,40]. This can be understood as follows: the electrons are emitted from a dot thermally and by a filed on a timescale which depends on the temperature and the bias, and on the eigenstate in which they are in. A charge already in the top most excited state will, for example, be emitted with an escape rate with Eq (6.56). In the dark

current, this time has to be lengthened by dividing it with the probability that the level is occupied. In the meantime, while charges are being emitted from the dot, other charges are being injected from the electrode.

In the QDIPs, the current flows along the growth axis under the applied bias. There are two main resistances to conduction along the growth axis: i) the injection barrier from the n-type contact Fermi level to the conduction band of the barrier material and ii) the resistance region produced by the QD layers. Experiments on QD-free samples have allowed us to establish that the dominant resistance of the complete QDIP device is caused by the QD region and not the interface. This does not mean that the contact injection resistance is completely negligible. Indeed it has ideally and in practice, a resistance comparable to a single QDIP layer to layer resistance.

In the steady state, as many are coming in as going out. The electrode injection rate I_{inj}, assuming injection into a drifting state, rather than a pure eigenstate, is given by

$$I = eA\int_0^{E_b} dE f(E)\rho(E)\mu F \exp\left[-(\frac{2m^*}{\hbar^2})^{1/2}\frac{4}{3eF}\{[E_b - E]^{3/2}\right] + eA\int_{E_B} dE\rho(E) f(E)\mu F \qquad \text{Eq (6.57)}$$

where the first term is Fowler-Nordheim tunneling through the injection barrier, A is the electrode area, and f(E) the Fermi function. The second term is the band contribution. The equality of injection current to bulk current establishes the Fermi level in the bulk.

Assuming the system is roughly neutral, then it follows that quantum dots which have just emitted will eventually be replenished by charges which are flowing about in the band. The typical timescale $1/C_{be}$ for reoccupation is 10^{-9} to 10^{-10} s, which is much longer than the typical transit time $L/\mu F \sim 10^{-12}$ s. So it follows that photo-excited charges will be flowing around the

circuit at very high speeds before they get captured again. This is the so called gain, and is one of the reasons why QDIPs represent an important technology.

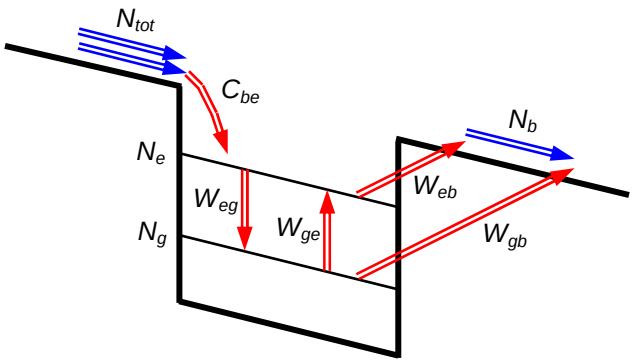

Figure 6.12. Schematic diagram for the processes of the electrons that escape from, capture into a dot and excite and recombine in the dot.

The theory of the dark current is developed using a rate equation approach dissimilar to the one in the literature[41]. In Figure 6.12, the schematic diagram of the processes involved in the dark situation is shown in two-level system. But this can be easily expanded into multi-level system. N_{tot} is the number of electrons which are provided to a quantum dot through the current injection from the electrode and proportional to the density of the quantum dots in one layer. N_e and N_g are the numbers of the electrons staying in the excited states and the ground state respectively. N_b is the number of electrons which are emitted from a dot to the barrier continuum. C_{be} is the capture rate from the band continuum to the excited state. W_{eb} and W_{gb} are the escape rates from each quantum level (e: excited state and g: ground state) to the band continuum. These escape rates can be obtained with the same method as the escape rate for the responsivity, Eq (6.56), because the photoexcited electrons and electrons under dark condition in a dot follow the same routes such as thermal activation and tunneling. W_{eg} is the transition rate

from the excited state to the ground state. W_{ge} is the transition rate from the ground state to the excited state. Because of the charge conservation,

$$N_{tot} = N_b + N_g + N_e \qquad \text{Eq (6.58)}$$

should be satisfied at any time. In Eq (6.58), N_{tot} is a constant which is determined as

$$\dot{N}_{tot} = Ae\mu(F)FN_d \qquad \text{Eq (6.59)}$$

But the other numbers N_b, N_g, and N_e change under circumstances. For the steady state, detailed balance rate equations can be written as

$$\begin{aligned}
\dot{N}_b &= N_e W_{eb} + N_g W_{gb} - N_b C_{be} = 0 \\
\dot{N}_e &= N_b C_{be} + N_g W_{ge} - N_e W_{eb} - N_e W_{eg} = 0 \\
\dot{N}_g &= N_e W_{eg} - N_g W_{gb} - N_g W_{ge} = 0
\end{aligned} \qquad \text{Eq (6.60)}$$

If we solve above equations to get the relation between N_b and N_{tot}, we can get

$$\begin{aligned}
N_b &= \frac{N_{tot}\left(W_{eb}W_{gb} + W_{eb}W_{ge} + W_{eg}W_{gb}\right)}{\left(W_{eb}W_{gb} + W_{eb}W_{ge} + W_{eg}W_{gb}\right) + C_{be}\left(W_{eg} + W_{gb} + W_{ge}\right)} \\
&\approx \frac{N_{tot}W_{eb}}{W_{eb} + C_{be}\left(1 + W_{eg}/W_{ge}\right)}
\end{aligned} \qquad \text{Eq (6.61)}$$

Here we use the approximation that W_{gb} is very small and can be neglected in most cases. Because W_{eg}/W_{ge} is the very occupation probability in the quantum dot level ‘e’ which obeys a Fermi distribution with a self-consistent Fermi level and temperature, Eq (6.61) becomes

$$N_b = \frac{N_{tot}W_{eb}f_e}{C_{be}\left[1 + f_e + \left(f_e W_{eb}/C_{be}\right)\right]} \qquad \text{Eq (6.62)}$$

In general, the quantum dot has more than two levels. In case of multi-level case, the number of electrons emitted from each level and therefore the dot emission currents from each level can add up. The general expression for the dot emission current can be written

$$I_{dot} = \frac{Ae\mu(F)Fn_d}{C_{be}} \left\{ \sum_s \frac{f_s W_{sb}}{(1 + f_s + W_{sb}/C_{be})} \right\}$$

$$W_{sb} = \nu_{sb} g_s \frac{\exp[-E_{sb}/kT] - \exp[-2\gamma a E_{sb}^{1/2}]\exp[-4\gamma E_{sb}^{3/2}/3eF]\exp[-E_{sb}/kT]}{1 - \exp[-2\gamma a E_{sb}^{1/2}]\exp[eFa/kT]} \qquad \text{Eq (6.63)}$$

where A is area, e is the electronic charge, F is the electric field, μ(F) is band mobility and n_d is the density of quantum dots. f_s is the Fermi function at level 's' and the Fermi level has to be determined self-consistently for each bias V and temperature T by matching injection and quantum dot escape current. W_{sb} is the escape rate from each quantum level s to the band continuum. For simplicity we define activation energy, also $\sum_s 2 f_s = \langle n_{dot} \rangle$ which is the mean number of electrons in a dot.

$$I_{dot} = \frac{Ae\mu(F)FN_d}{(1 - n_e)C_{be}} < g_s \nu_{sc} > \exp[-E_D(F)/kT], \qquad \text{Eq (6.64)}$$

The total current across the device area includes also the uniform band contribution as in Eq (6.57). The prefactor $g_s\nu_{sc}$ is the product of the density of final states and the sum over all paths from a level "s" to the continuum "c". It will in principle depend on the energy difference and by experience will be scaled by the Meyer-Neldel factor (MY) $\exp[(E_c - E_s)/\hbar\omega_0]$ where $\hbar\omega_0$ is an optic phonon energy and represents the dominant mode for thermal transitions in these materials. The MY enhancement is an empirical way to take into account the fact that there are many ways for the charge to reach its final destination[42,43].

6.5 Gain

The high photoconductive gain observed in semiconductor quantum dot infrared detectors (QDIPs) constitutes one of the most exciting recent topics in nanotechnology. In this chapter we present a theory of diffusion and recombination which is an attempt to explain the high values of gain in QDIPs. We allow the kinetics to encompass both the diffusion and capture rate limited regimes of carrier relaxation using rigorous random walk and diffusion methods. The photoconductive gains are calculated. In a later chapter, we will compare the calculated gain with the experimental values obtained from InGaAs/InGaP/GaAs[44] and InAs/InP[45] QDIPs using the Generation Recombination noise analysis. The theory can be also applied to other material systems as well.[46,47,49,50,51]

6.5.1 Introduction

QDIPs have longer carrier lifetimes, which create the potential for higher photoconductive gain and higher operating temperature.[17] Understanding the photoconductive gain is important to understanding and optimizing QDIPs. We recall that the photoconductive gain is defined as the ratio of the recombination time to the transit time of photo-generated carriers. Recombination time is defined here as the time the carrier is free before it falls back down into the QD state from which it was emitted. Despite its importance, only a few attempts have been made so far to give the measured values of gain a fundamental theoretical interpretation. Photoconductive gains of QDIPs have been reported by many research groups,[46,47,48,49,50,51] the reported values span a very broad range from ~1 to ~10^6 depending upon the material, applied bias, and temperature. To explain the large values of the measured gain

various interpretations have been proposed, some invoking high electron mobility of the barrier materials,[46] and or, the low carrier capture probability (or long carrier life time).[48,50,51] Avalanche mechanisms have also been proposed.[47,49] These were invoked to understand the high gain (~ 20) observed in hot carrier QWIP devices. The objective of this paper is to analyze the gain in quantum dot infrared photodetectors (QDIPs) in terms of a unified rigorous transport mechanism which allows one to integrate the main mechanisms into a single practical formula.

6.5.2 Methodology

Using an adaptation of the t-matrix diffusion and recombination formalism of Ghosh et al.[52], we present formulae for the time decay and steady state QDIP photocurrent. The recombination kinetic exhibits a diffusion and a recombination rate limited regime. We will allow the band mobility to be affected by trapping and de-trapping of charge. The trapping can be due to “shallow” defects and constitutes a random process. It can in general encompass also the top shallow bound levels of a quantum dot (QD), the wetting layer bound states, and other random defect centers in the barrier layers. We will use the basic formula for dark current and responsivity in an n-QDIP as given in the previous section. The recombination dynamics will be discussed later.

The In(Ga)As layers which form the QDs are n-doped with Si, to allow on average up to 3-electrons per a QD, filling the lowest (ground) state and partially the first excited state. The carrier will typically obey the following scenario: direct escape or first excitation from the QD levels below the Fermi level to the bound levels nearer the continuum, and then tunnel or thermally escape out into the band; then travel either to the contact or get trapped. The trapping

can be in a shallow non QD-state, normally a wetting layer state, from which the carrier can escape again. The trapping can also take place in the excited state(s) of the QD from which the carrier can either escape or recombine into the lower QD levels. This scenario also brings with it, its own noise structure known as the "Generation-Recombination" (G-R) noise where the noise current I_n is related to the gain "g" via the dark current I_D through $I_n = \sqrt{4egI_D\Delta\nu}$ where e is an electron charge and $\Delta\nu$ is the frequency bandwidth[38]. In the real system, one normally finds that the measured noise is quite a bit more complex than that. At low bias the noise is frequency dependent and behaves as 1/f noise. Then as we go up in frequency, the 1/f behavior turns constant which is a sign that we have reached the G-R noise situation. At very high bias, the carrier generation process is no longer dominated by supply from the QD but by direct injection from the electrode. The experimental results show that there is only a well defined range of biases over which we can discuss about G-R noise[50]. This is the regime we will now try to model.

In the formalism derived in the previous section 6.3, one key quantity is C_{be}, which is the effective rate of capture of a band electron to the excited top QD state of any QD from which it recombines down into the ground levels, on a time scale faster than back up again into the conduction band. The quantity C_{be} is the inverse of the average time it takes for a delocalized band electron near the bottom of the conduction band to fall into a QD excited level, as precursor to recombination. Thus in the language of random walk diffusion and trapping theory, $1/C_{be}$ is the time integral of the survival fraction.

We shall now examine what this means in terms of recombination kinetics. But before doing that, we note that in a 3-dimensional system, the trap and saturation limited velocity which enters the theoretical gain formula (recombination time/transit time) should be written as

$$v_d = \mu_o F\left(1+\sum_l \frac{W_{bl}(1-n_l)}{W_{lb}}\right)^{-1}\left[1+(\frac{\mu F}{v_s})^2\right]^{-1/2} \qquad \text{Eq (6.65)}$$

and in this approach the photoconductive or dark current gain is indeed

$$g = \frac{v_d}{LC_{be}} \qquad \text{Eq (6.66)}$$

where L is the length of the active region of the device, F the applied field, μ is the trap controlled mobility, μ_0 is the trap-free mobility, W_{bl} and W_{lb} are trapping and detrapping rates, v_s is the saturated velocity, and n_l the occupation number of trap "l". When the carrier takes a long time to get in from the contact, then the system will have a low gain; it is as if it has a long transit time. The pure bulk band mobility on the other hand, includes the trap term but not the injection term.

Now let us consider the carrier dynamic from a time dependent point of view. We don't consider the precise spatial distribution of these traps, only the configurationally average effect will be allowed. Note also that in a high electric field, the band velocity will saturate at the value v_s, typically order of 10^4 to 10^5 m/s and different for different materials. Consider now an electron moving in a band with effective mobility μ and diffusivity D where μ is eD/kT. It can be described by the diffusion equation with recombination centers. The trapping and release is included in the definition of D(T,V).

$$\frac{\delta n(r,t)}{\delta t} = G_g(r,t) + D\nabla^2 n(r,t) + \frac{\delta n(r,t)}{\delta x}\mu_b F_x - \sum_i n(r,t)V(r-r_i) \qquad \text{Eq (6.67)}$$

Here n(r,t) is the band occupation density at time 't' at point '**r**', V(**r**-$\mathbf{r_i}$) is the capture rate due to the i'th QD at $\mathbf{r_i}$. The generation rate is denoted by G_g. For a single carrier created in the band at time t=0 at **r**=0, $G_g = \delta(\mathbf{r},t)$, the above can be thought of as the Green function of a "Schrödinger like" equation with V(**r**) being a scattering potential. If the QDs were uniformly distributed, we would have a standard band structure problem to solve with $V(\vec{r}) = \sum_i V(\vec{r} - \vec{r}_i)$ acting as the periodic potential. For a random distribution and spherical symmetric trapping rates, the problem has been solved by Ghosh et al. in the average t-matrix approximation[52]. Even though our QDs are in general not spherical, we will assume for the present purpose that they are, and choose the radius of the QD so that it occupies the same volume as the true QD. The full result with various spherical trapping potential models is given in Ref. 52. For traps of range R_t with capture rate strength V_t, the result for an isotropic 3d system with trap concentration N_t is

$$C_{be} = \frac{1}{\tau} = N_t(4\pi D R_t)\left[1 - \left(\frac{D}{V_t R_t^2}\tanh\left(\frac{V_t R_t^2}{D}\right)\right)^{1/2}\right] \qquad \text{Eq (6.68)}$$
$$V_t(r) = V_t\ (r < R_t); V_t(r) = 0\ (r > R_t)$$

This result has two limits. Recombination time limited capture occurs when $D/(V_t R_t^2) >> 1$, then we have

$$C_{be} = 4\pi R_t^3 V_t N_t / 3 \qquad \text{Eq (6.69)}$$

for a spherical potential. For a lens shape potential with the corresponding volume filling factor gives

$$C_{be} = \pi R_t^2 h_{QD} V_t N_t \qquad \text{Eq (6.70)}$$

with $4\pi R_t^3 / 3 = \pi R^2 h_{QD}$ defining the effective radius R_t.

When $D/(V_t R_t^2) << 1$, on the other hand, we have the diffusion limited result (effective spherical potential) and we have

$$C_{be} = N_t \left(4\pi D R_t\right) \qquad \text{Eq (6.71)}$$

The above result should be compared to the drift-limited Shockley Read result

$$C_{be} = N_t \left(\pi R_t^2 V_{th}\right) \qquad \text{Eq (6.72)}$$

where the classical thermal V_{th} velocity could be related to the diffusion quantities via $V_{th} \rightarrow D/a$, a is the lattice constant. It is interesting to note that in the Shockley-Read theory, the carriers are always drifting between collisions. They are moving at the thermal velocity. They don't actually diffuse from site to site in the random walk sense, but rather go from collision to collision with a fixed velocity. The Shockley-Read approach is classical and is indeed how one would treat the problem in a semi-classical Monte-Carlo model. In reality when a carrier undergoes a capture, then it escapes out mainly in bias direction, but then quickly randomizes again to a "diffusing" wave. The effect of drift on the diffusion/recombination dynamics is not important at these biases where v_d is smaller than D/a in 3-dimensions[52] and has been neglected as discussed by Grassberger et al[53].

6.5.3 The capture-recombination rate

The recombination-capture rate V_t can and in general will be bias and temperature dependent so $V_t(V,T)$. It can, and often will be, a combined process involving a capture step W_{be}

into the first bound state of the QD and then subsequently a relaxation step W_{eg} into the lower energy states. So in general we may also write V_t as $1/\left(1/W_{be}+1/W_{eg}\right)$, so that the rate determining step is the slower one. When the escape rate from the bound excited state W_{eb} is faster than the recombination step, i.e. when $W_{eb}>W_{eg}$, then the QD acts only as a temporary trap for the carrier. But this is unlikely since W_{eb} being tunnel/activated is small at low temperatures despite the fact that W_{eg} may also be bottlenecked down to 10^9 Hz. At higher temperatures, both rates go up reaching a peak of ~ 3×10^{12} Hz for W_{eg} and 10^{12} for W_{eb}. We will treat V_t as a parameter and not try to study its intricate and subtle structure. We will therefore for the time being neglect the temperature and bias dependence and argue that the main bias and temperature dependence of the dynamic is indeed in the drift term via the bias/temperature assisted trapping escape rate in the mobility. We will come back to this interesting point later.

6.5.4 Interpretation of the gains

The Eq (6.70) is a good enough approximation, but could in principle be generalized to include also a distribution of QD sizes using a suitable Gauss averaging of capture rates V_t. For lens like structures, the Eq (6.70) is approximately valid provided that the volume is normalized to the right value. The gain in this formalism becomes

$$g=\frac{\mu F}{L}\left[1+\left(\frac{\mu F}{v_s}\right)^2\right]^{-1/2}\left[N_t\left(4\pi DR_t\right)\left(1-\left(\frac{D}{V_tR_t^2}\tanh\left(\frac{V_tR_t^2}{D}\right)\right)^{1/2}\right)\right]^{-1} \qquad \text{Eq (6.73)}$$

which depends on the elementary capture rate V_t, the effective radius R_t, the density of QDs, N_t, the band diffusivity D and mobility which are related to each other $\mu=eD/kT$, and which can be trap-limited and thus temperature and bias dependent. We assume the uniform electric field over

the active region thickness of the device (L) with an applied bias V, and thus applied electric field F be written as V/L. The trap controlled mobility μ can be modeled and calculated using the multiple path-sum detrapping rate from Ref. To illustrate how this works consider the situation where a carrier can be trapped with rate ν_t, and escape either vertically upward in energy with rate $\nu_e e^{-E_t/kT}$, or Fowler-Nordheim tunnel escape adiabatically with rate $\nu_F e^{-sE_t^{3/2}/F}$ where s is constant. If we include all intermediate paths as well, assume the same prefactors, then we can derive a simple approximate form

$$\mu = \mu_0 \left(\frac{e^{-E_t/kT} - e^{-\varsigma E_t^{3/2}/eFa} e^{-\varsigma E_t^{1/2}} e^{eFa/kT}}{1 - e^{-\varsigma E_t^{1/2}} e^{eFa/kT}} \right) \Bigg/ \left[x + \frac{e^{-E_t/kT} - e^{-\varsigma E_t^{3/2}/eFa} e^{-\varsigma E_t^{1/2}} e^{eFa/kT}}{1 - e^{-\varsigma E_t^{1/2}} e^{eFa/kT}} \right] \quad \text{Eq (6.74)}$$

where E_t is the single (for simplicity) effective trap energy and μ_0 is the trap free band mobility and where "x" is the volume concentration of traps. Normally we are in the limit where x is much larger than the escape ratio in the denominator of Eq (6.74) so that only the numerator matters. The effect of bias on the quantum mechanical capture rate $V_t(V)$ has been neglected and we also have $\mu F R_t < D$. If the bias dependence D(V) and $V_t(V)$ are known, then they can be included.

The Eq (6.68) for the recombination time ($1/C_{be}$) is plotted in Figure 6.13 with different parameters such as temperature, trap energy, capture rate and QD radius as a function of field F. The temperature and electric field do not change the recombination time $1/C_{be}$ significantly because we are in the capture rate limited regime and we are assuming that V_t is only weakly bias-dependent in this regime. As the trap energy changes however, from 0.01 to 0.1 eV, the recombination time $1/C_{be,}$ can, depending on bias and temperature, become diffusion limited. At higher electric fields, the dynamic can change from diffusion to capture time limited, because the

high electric field assists the escape of the carriers from the traps. In the capture rate limited regime, increasing V_t, the quantum mechanical capture rate, results in a faster recombination time $1/C_{be}$. Interestingly, smaller quantum dots result in slower recombination times. For small bias and low enough temperatures the recombination (gain) is diffusion limited[54].

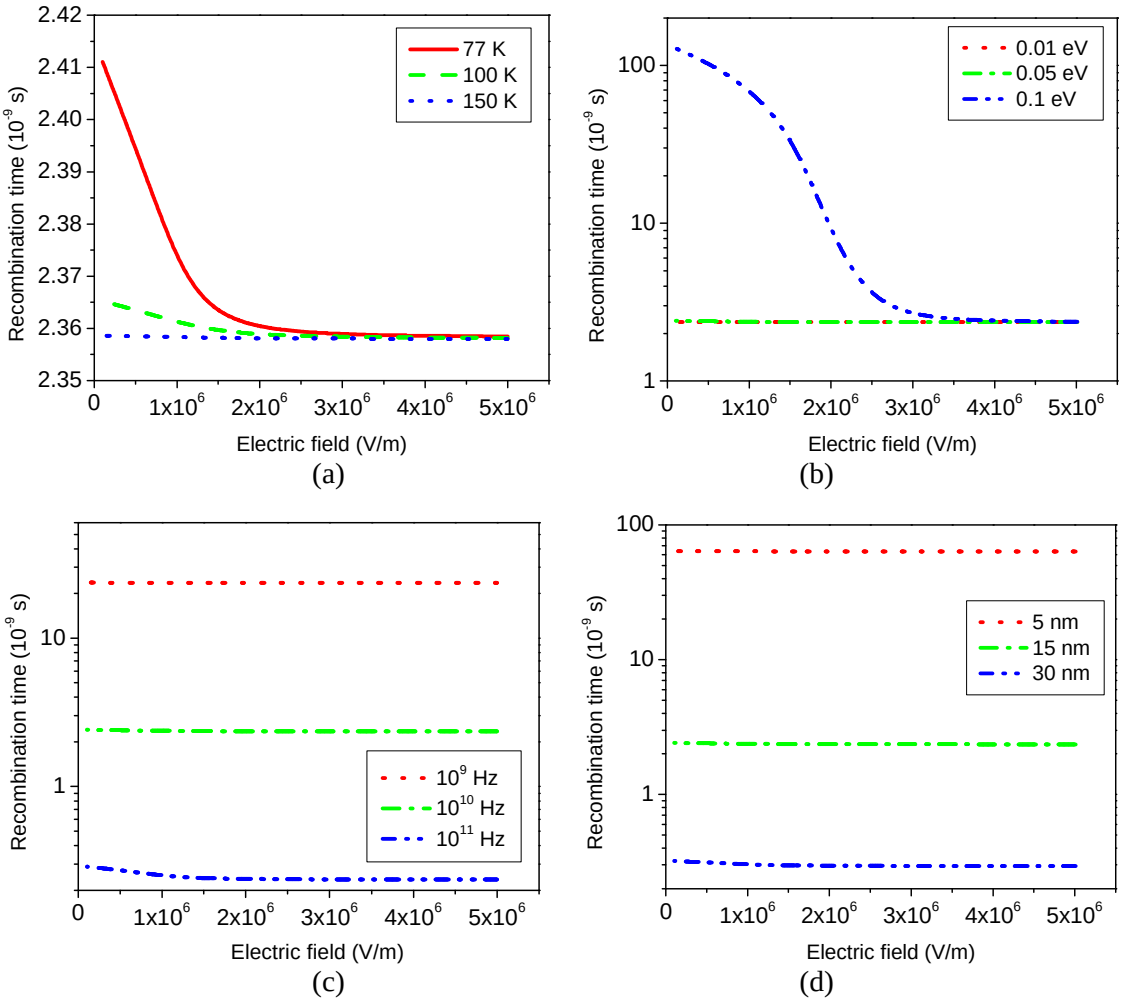

Figure 6.13. The recombination rate C_{be} with following default parameters: μ_0/x =1 m^2/Vs, x=0.1, T=77 K; $V_t=10^{10}$ Hz, $V_s=3\times10^5$ m/s, E_t=0.05 eV, $N_t=3\times10^{21}$ m^{-3}. For the variations of (a) temperature (b) trap energy (c) capture rate (d) radius of quantum dot. The insensitivity to bias in

Fig.1 c) and d) and even a) is because we are truly in the trap limited regime as in Refs. 44 and 45 so the time limiting step is V_t which is here assumed independent of bias. (b) has a larger trapping energy and is indeed in the diffusion limited regime.

In the paper by Choi[55] which is the generally accepted way of formulating the gain of quantum well infrared photodetectors (QWIPs), one uses a semi-classical description and writes for the gain defined as the ratio of recombination to transit time

$$g = \frac{1}{N}\frac{1-p_c}{p_c}$$
$$p_c = 1-\exp(-t_p/\tau_H) \qquad \text{Eq (6.75)}$$

where N is the number of periods, p_c is the capture probability, t_p is the transit time across one period, and τ_H is the recombination time from an extended state back into a quantum well. When $t_p << \tau_H$ and $p_c<<1$, we have

$$g = \frac{1}{N}\frac{\tau_H}{t_p} \qquad \text{Eq (6.76)}$$

Basically the product "Nt_p" is just the total transit time. A similar formula which is an adapted QWIP formula $g = (1-p_c)/(NF_{QD}p_c)$ which includes the QD relative space filling factor F_{QD}. If we rewrite our QDIP result in the capture time limited regime from Eq (6.69) as $g = \mu F/(LV_t(4\pi R_t^3 N_t/3))$ and compare with $p_c<<1$ in Eq (6.76) then we can see immediately what F_{QD} signifies. The Eq (6.73) is more general as it does not assume that the carriers are always in the capture limited regime. It allows the recombination to be diffusion-limited, which may happen at very low temperatures when we include the traps.[52]

The volume concentration of traps "x" is at least the same as the fill factor F_{QD} and assumed here to be 0.1. Typical theoretical gains with different parameters are shown in Figure 6.14. The gain curves shown in Figure 6.14 correspond to different choices of parameters and obviously agree with the trend exhibited by the corresponding recombination times $1/C_{be}$. The temperature increases the gain as shown in Figure 6.14, because the trap limited mobility increases with temperature. The magnitude of the recombination-capture rate V_t and QD radius also affect the gain. The smaller quantum dots will have lower recombination-capture rates V_t because the larger level separations decrease the relaxation rates and encourage the "phonon bottleneck"[22].

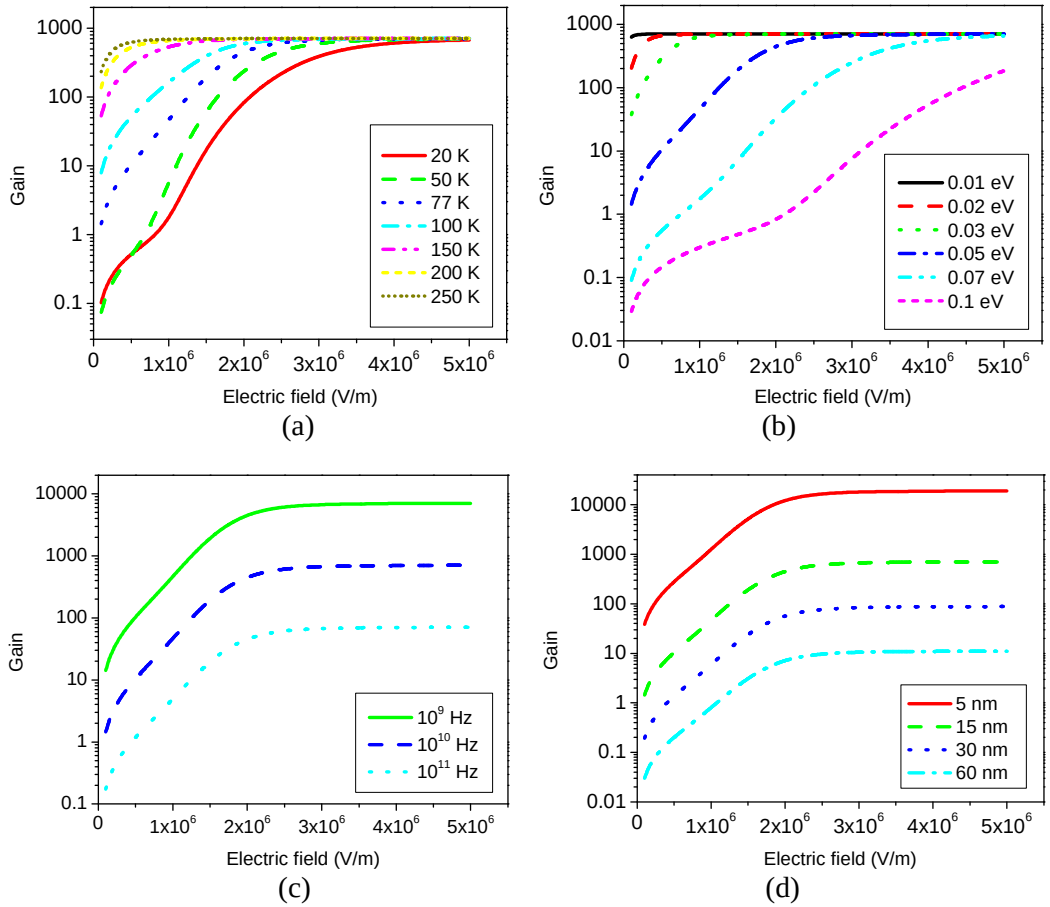

Figure 6.14. The theoretical gain curves as a function of electric field in V/m with the different physical parameters encompassing the trap limited and diffusion limited situations as defined by the Eq (6.69), Eq (6.71) and Eq (6.73). The default parameters are following. T=77 K, V_t = 10^{10} Hz, μ_0/x =1m^2/Vs, N_t =3×10^{21}/m^3, V_s=3×10^7cm/s, R_t =15nm, and E_t=0.05 eV. For the variations of (a) temperature (b) trap energy (c) capture rate (d) radius of quantum dotrecombination rate C_{be} with following default parameters: μ_0/x =1 m^2/Vs, x=0.1, T=77 K; V_t=10^{10} Hz, V_s=3×10^5 m/s, E_t=0.05 eV, N_t=3×10^{21} m^{-3}. For the variations of (a) temperature (b) trap energy (c) capture rate (d) radius of quantum dot.

A small size quantum dot is therefore beneficial to achieve high gain and good performance in QDIPs. The smaller QD will also in general have a higher oscillator strength for photo-excitation. Then we note that for a given excitation wavelength, the bound-to-bound transitions which involve two localized states in the QDs, have a stronger oscillator strength (more overlap) than the bound-to-continuum transition for the same excitation energy. For a selected wavelength, the ideal QD as far as the oscillator strength goes, is one in which we have two bound levels, and the excitation is from the lower to the upper bound state. This is confirmed by calculations too. We also note that the carriers trapped in traps with shallower energies do not need a strong bias to escape and this causes a weaker bias-dependent gain.

In order to compare the theoretical model with the experimental data, we used two QDIPs systems from Refs. 44 and 45. The gain can be extracted using $I_n = \sqrt{4egI_D\Delta\nu}$. Comparison of gains from experiment with theory as a function of bias is shown in Figure 6.15. The selected numbers used to fit the data are reasonable for the QDIP devices. To obtain good agreement for

g(V) with experiments on InGaAs/InGaP QDIPs[44] and InP/InAs QDIP,[45] we needed to assume a trap energies E_t in the range from 0.092 to 0.06 eV and a local capture rate V_t from 1×10^9 to 3×10^{10} Hz which are very reasonable

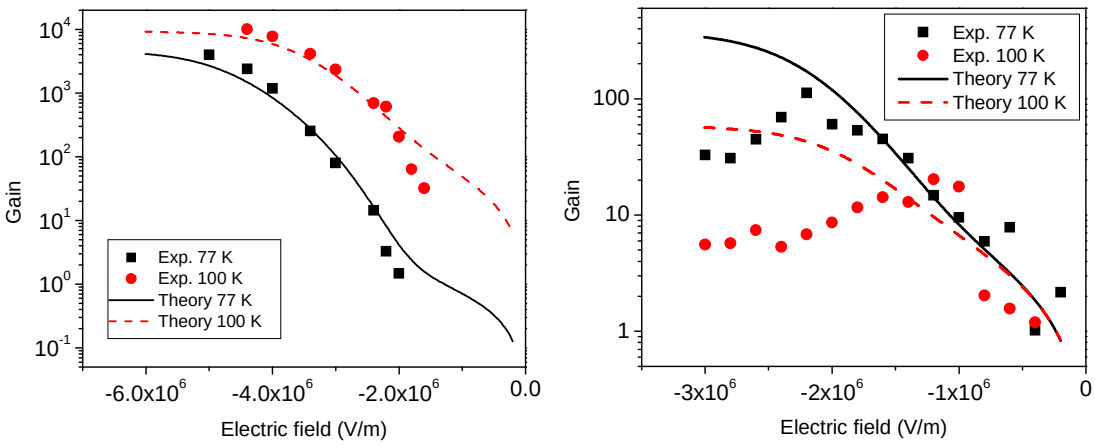

(a) (b)

Figure 6.15. Comparison of experimental and theoretical values of gain as a function of bias.

(a) InGaAs/InGaP from Ref. 44. At 77 K, $V_t = 1\times10^9$ Hz, $\mu_0/x = 0.5$ m^2/Vs; $N_t = 5\times10^{21}$/m^3, $V_s = 1\times10^5$ m/s , $R_t = 15$nm, and $E_t = 0.102$ eV. At 100 K, $V_t = 1\times10^9$ Hz, $\mu_0/x = 0.5$ m^2/Vs; $N_t = 5\times10^{21}$/m^3, $V_s = 1\times10^5$ m/s , $R_t = 15$nm, $E_t = 0.086$ eV.

(b) InAs/InP from Ref. 45. At 77 K, $V_t = 3\times10^{10}$ Hz, $\mu_0/x = 0.5$ m^2/Vs; $N_t = 1.2\times10^{21}$/m^3, $V_s = 1\times10^5$ m/s, $R_t = 15$nm, and $E_t = 0.06$ eV. At 100 K, $V_t = 2\times10^{11}$ Hz, $\mu_0/x = 0.5$ m^2/Vs; N_t 1.2×10^{21}/m^3, $V_s = 1\times10^5$ m/s, $R_t = 15$nm, $E_t = 0.06$ eV.

and agree with measurements and Monte Carlo estimates given in the literature on InAs/GaAs QDIPs as well[56]. We recall that the computed QD top bound level, which could also constitutes a trap in this logic, had capture energy around 0.1 eV in the InGaAs devices. A similar behavior of the gain has been observed in the work of Zhengmao et al.[50]. Usually one assumes that the time

of carrier re-injection is negligible, so the photoconductive gain is limited by the ratio of the recombination time to the transit time. Turning now again to the temperature dependence of the measured gain, we note that for a fixed capture rate V_t, the gain is expected to increases with temperature because in our model the trap limited mobility increases. We can observe such an increase of the gain from 77 K to 100 K for the InGaAs/InGaP/GaAs QDIP system in Figure 6.14. In Ref. 50, the increase of the gain can be expected to be due to a decrease of the capture probabilities as the temperature goes up. From Eq (6.73) it follows that in principle, there can be a temperature dependence coming both from the mobility and from the recombination-capture rate V_t. In the present model, which we developed for our devices, the main change is contained in the mobility. But a completely general analysis must allow different kind of scenarios. Thus in a very ordered device and trap free material, the band mobility may indeed even go down with temperature and this would then reduce the gain. The recombination-capture rate V_t will in general go up with temperature and reach a maximum ~10^{12} Hz[57]. Thermal fluctuations will produce level broadening and enhance the phonon emission cascade down the QD energy ladder into the ground levels. The responsivity strongly decreases with temperature above ~120 K, precisely because of the shortening of the excited state lifetime W_{eg}. Thus thermal fluctuations help to override any phonon bottleneck caused by energy mismatch, i.e. the mismatch between integral number of optic phonons and energy separation. At very high bias in Figure 6.15 (b), the gain starts to decrease again. The only mechanisms that can make the gain go down with bias are a decrease in the drift velocity caused by intervalley scattering, or simply the fact that the hot carrier injection has taken the system out of the G-R noise regime. If the high electric field were to reduce $V_t(V)$, this would raise the gain[56]. The data in Figure 6.15 (b) strongly suggest that the

gain saturation and decrease are due to hot carrier intervalley scattering as seen in the bulk material.

In the Monte Carlo (MC) model of Kochman et al.[56], there is no trap limited mobility as such , but the carrier is allowed to escape the capture into the quantum dot by way of a bias assisted process similar to detrapping. Here trapping sites are identical to recombination sites and are constituted by the quantum dots. The authors predict a gain which increases with bias up to value of order g~10 and in a superlinear way. Our model includes in principle a wide distribution of traps and uses the effective trap energy as a parameter. In our model the gain can reach much higher values with reasonable parameters. We believe that the observed voltage dependence of the gain in the present category of devices is due to shallow trap limited mobility[44,45,50]. A carrier being trapped in the top bound state of the QD is much more likely to go further down and recombine then go back up again. The bias assisted detrapping is more likely to be effective for those trap sites which are intrinsically shallow and there is no level further down. This view is supported by the transient data analysis given below. The observed gain in the region where the G-R noise formula holds is strongly voltage dependent, almost exponentially. This is true in most of our devices and those of Ref. 50. The gain values in the peak responsivity region of QDIPs are high, always in the range 100 to 1000, so that the lifetime in Eq (6.68) is recombination rate V_t limited and not drift or diffusion limited. This is true even though the mobility is still increasing with voltage. The high gain is a feature in almost all QDIPs, and is indeed one of the advantages of this technology over the QWIPs where most often g<1.

In the low voltage and low (noise) frequency regime, the noise is in general not dark current limited, and the G-R formula does not apply. This can be true also for very high biases

where carriers are generated by injection and not by emission out of the QD. If one still insists on extracting the gain using the G-R formula however, then one can get peculiar and unphysical bias dependences as shown in the experimental gain curves of ref. 50 at low bias and also in our own work[57].

6.6 Modeling of Detectivity

The measure of device performance is that the signal be at least as great as the background noise. The measure for useful performance is therefore the specific detectivity D*, defined as the ratio of responsivity over the square root of the dark current density at a given bandwidth multiplied by the gain.[58]

This can be written in the elegant form (unit band width, D* in $cmHz^{1/2}/W$)

$$D^* = \frac{R^*}{[eg(I_D)]^{1/2}} \qquad \text{Eq (6.77)}$$

Theoretical modeling of peak detectivity Eq (6.77) can be rewritten combining Eq (6.45) and Eq (6.64) as follows.

$$D^* = \left[\frac{\langle Q\nu_{ec} \rangle^{1/2}}{\nu_0 + \nu_t e^{-\Delta/kT} + \langle \nu_{ec} \rangle e^{-E_{ec}/kT}} \right] \frac{\langle \alpha(\omega,T) \rangle}{A^{1/2} N_d \hbar\omega} e^{(E_D/2kT - E_{ec}/kT)} \qquad \text{Eq (6.78)}$$

where $Q = N_d AL$ is the total number of quantum dots in the device.

7 Theoretical analysis on InGaAs/InGaP/GaAs Quantum Dot Infrared Photodetectors

In this chapter we will discuss the theoretical analysis on one of the InGaAs/InGaP/GaAs QDIPs based on the theoretical modeling we have discussed in the previous chapter.

7.1 Device structure

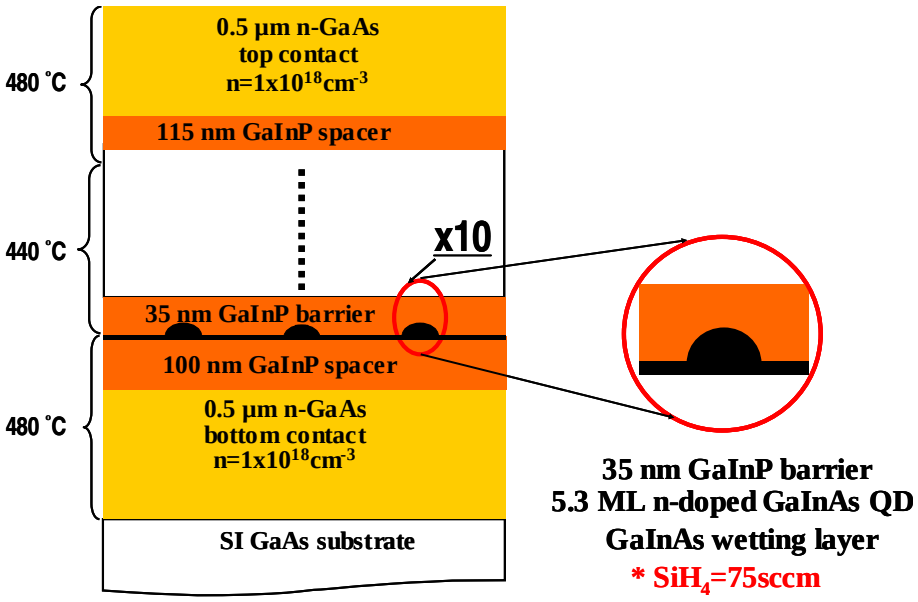

Figure 7.1. GaInAs QD/GaInP/GaAs QDIP device schematic diagram.

We succeeded in developing GaAs/GaInP based QDIPs. The InGaAs quantum dots are grown on GaInP matrix which is lattice matched to GaAs substrate. A LP-MOCVD reactor was used to grow the InGaAs quantum dots on semi-insulating (100) GaAs substrate. Trimethylindium (TMIn), triethylgallium (TEGa), and pure AsH_3. In Figure 7.1, the first grown was a 0.5 µm bottom GaAs contact layer doped with SiH_4 to $n=1\times10^{18}cm^{-3}$ and 0.1 µm lattice-matched InGaP thick barrier. Next grown was a series of multiple quantum dot layers consisting

of 10 barrier layers of undoped lattice-matched InGaP confining 10 GaInAs quantum dot layer. The nominal thickness of the barriers was 350 Å. The InGaAs quantum dots were formed on top of InGaP matrix (barrier) by self-assembly method which is based on Stranski-Krastanow epitaxy growth mode. The growth time for InGaAs quantum dots was 5 seconds and the ripening time was 30 seconds with AsH_3 flow. The growth rate and V/III ratio of InGaAs quantum dots were 0.68 ML/sec and 480, respectively. The dots density as given by atomic force microscopy (AFM) was 2.7×10^{10} cm^{-2}. InGaAs dot had the disk-like shape with 20 nm in diameter and 4 nm in height as shown in Figure 7.2. The InGaAs quantum dots were doped to n-type with dilute SiH_4 (200 ppm) with flow rate of 50 sccm. Last grown was a 0.15 µm lattice-matched InGaP thick barrier and 0.5 µm top contact layer of GaInAs doped to $n=1\times10^{18}$ cm^{-3}. The whole structure was grown at 480ºC except the active region, which was grown at 440ºC.

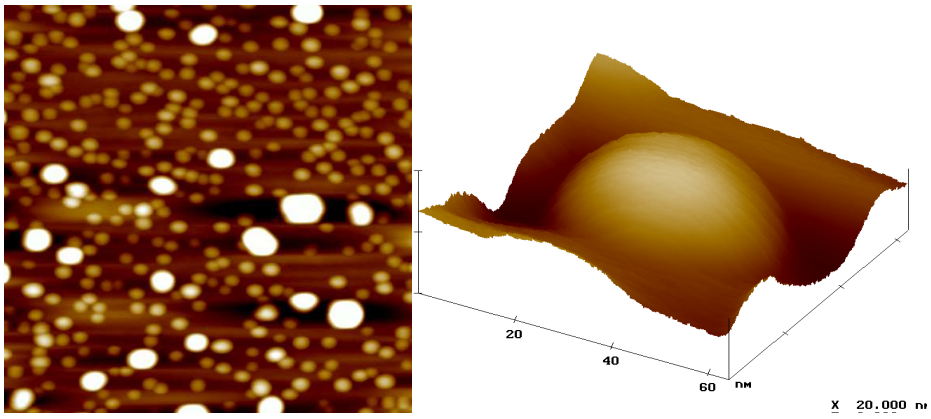

Figure 7.2. (left) 1µm x 1µm AFM image of GaInAs on GaInP matrix (right) Lens shaped quantum dots with typical diameter of 40nm and height of 4nm.

To test QDIP's performance, 400 µm×400 µm detector test mesas were fabricated with selective wet chemical etching through the bottom contact layer. AuGe/Ni/Au bottom and top

metal contact were made via lift-off technique and alloyed at 400ºC for 3 minutes. The sample was then mounted to a copper heatsink and attached to the cold finger of a cycled Helium cryostat equipped with a temperature controller.

7.2 Device analysis

In this section, the methods of the device modeling which were discussed in previous Chapter 6 will be applied to the one of the best devices in InGaAs/InGaP/GaAs QDIPs.

Energy levels and oscillator strengths

The energy levels and the corresponding oscillator strengths are shown in Figure 7.3. The quantum dots in Figure 7.2 have rotational lens symmetry. The calculations were done using the single band effective mass embedding method neglecting strain effects, which was described in 6.1.2.4. The geometry, "lens-shape", is taken from the AFM image as Figure 7.2. The base lengths and heights are approximately 40 nm and 4 nm, respectively. Effective masses m* are as follows; InGaAs: $0.05m_e$, InGaP: $0.11\ m_e$, GaAs: $0.063\ m_e$. m_e is the free electron mass.

The strongest photonic transitions are usually the ones which are energetically directly above each other, with an s-symmetry (m=0) to p-symmetry (m=1) change. The observed photoconductive transition (see Figure 7.4), as measured by Fourier transform infrared spectroscopy, at a peak wavelength of 4.6 μm is indicated in Figure 7.3, and as one can see, it does not have a high oscillator strength $f_{ge} \sim 5\times10^{-3}$ in s-polarization.

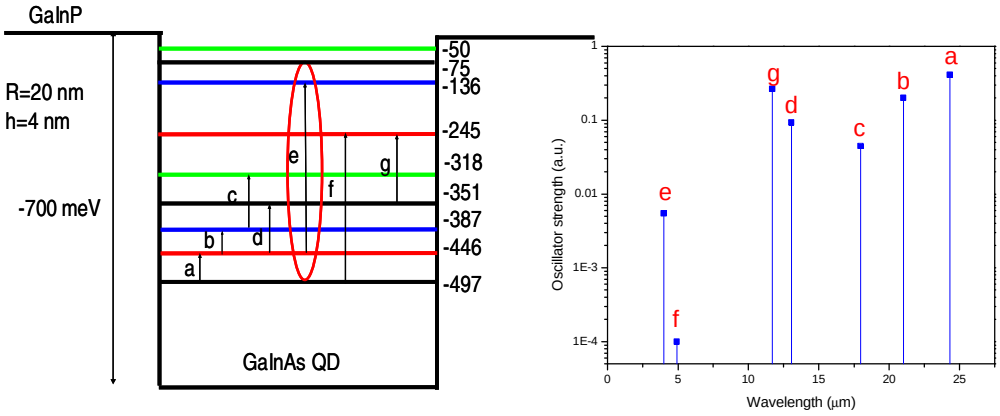

Figure 7.3. (Left) Calculated quantum dot energy levels and (right) oscillator strengths for s-polarized light.

The strongest s-polarized absorption is indicated by the line in Figure 7.3 and is at low energy. The carrier would have very little chance of escaping from such a deep level.

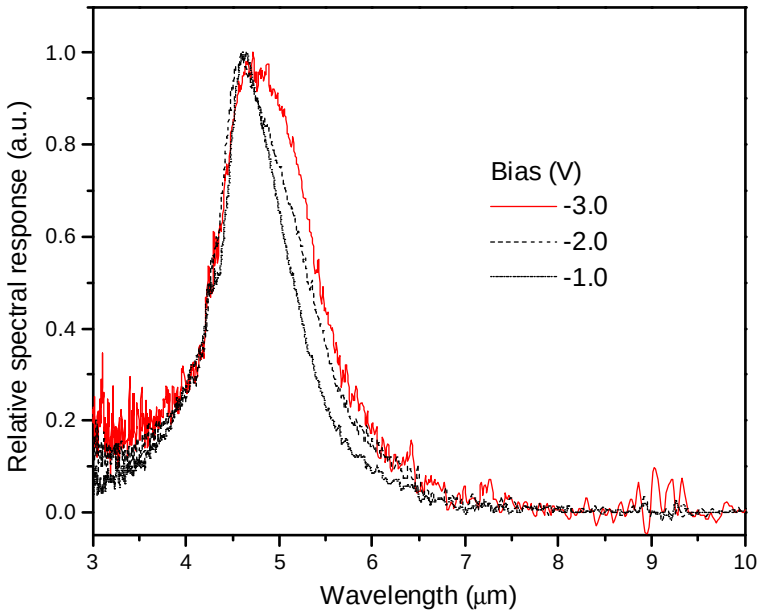

Figure 7.4. Variation of lineshape with applied bias at T=77K as measured by Fourier transform infrared spectroscopy.

The optimum escape path is an optically excited state which is still bound but very close to the continuum. This has been achieved in the best QWIP devices[38]. In QDIPs, the situation is somewhat more complicated.

Absorption and Peak Responsivity

In order to remind the equation of the absorption, the absorption coefficient $\alpha(\omega)$ can be written again.

$$\alpha = \frac{\pi\hbar N_d n_{op} e^2}{m^* \varepsilon \varepsilon_0 c}\left[\frac{\Gamma}{(\hbar\omega - E_{eg})^2 + \Gamma^2}\right] n_g (1 - n_e) f_{ge} \qquad \text{Eq (6.42)}$$

The absorption coefficient also involves the following quantities: i) the dot density $N_{d,}$ ii) the oscillator strength f_{ge}, and iii) the probability n_g that the carriers remain in the initial state and can absorb a photon. The dot density is typically ~$10^{22}/m^3$. The oscillator strength f_{ge} is, as we have seen, low for the transition in question because it involves a high excitation inside a relatively large dot. It could in principle be as high as 0.2, in p-polarization for smaller dots[59]. There is room for improving the oscillator strength by quantum dot engineering which means the reduction of the quantum dot size. For good performance, it is important that n_g stays high as the temperature goes up, as is achieved in QWIPs[60]. In QDIPs, this quantity is in the first place dependent on the level distribution in the dots corrected by polaron renormalization as shown in the literature [61, 62, 63]. Assuming Boltzmann statistics for convenience, n_g can be written

$$n_g = \frac{e^{-E_g/kT}}{\sum_s d_s e^{-E_s/kT} + \sum_t e^{-E_t} + \int_{\varepsilon_c} d\varepsilon \rho(\varepsilon) f(\varepsilon)/N_d} \qquad \text{Eq (6.43)}$$

where the E_s are the quantum dot energy levels, d_s the degeneracy, the "t" sum is over traps including the new eigenstates formed by electron phonon resonances; $\rho(\varepsilon)$ is the band density of states and $f(\varepsilon)$ the Fermi function. The plot of n_g and n_1 with temperature is shown in Figure 7.5 assuming one electron in a dot. As we can see, the occupation probability of the ground state decreases with the temperature, while the occupation probability of the first excited state increases up to 300K and decreases. Since the most probable transition of the current QDIP starts from the first excited state, it is important to fill the electrons up to first excited state at desired temperature through the doping of the quantum dot. In the experiments, actually, we could observe the doping dependence of responsivity.

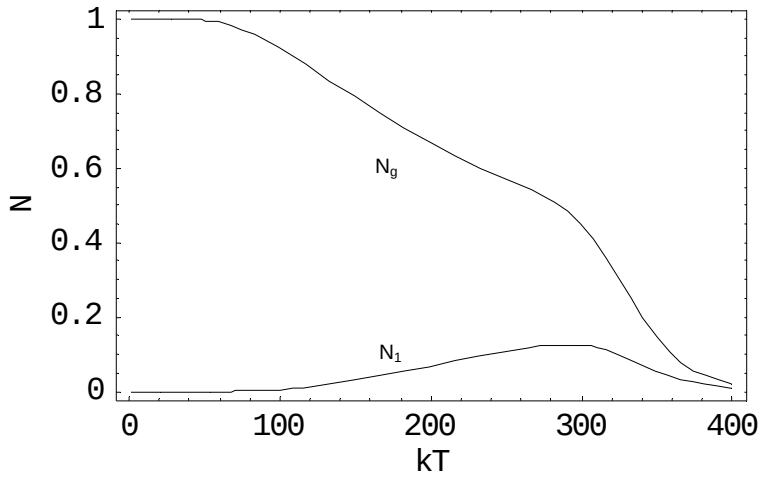

Figure 7.5. Probability of staying in the ground state with polaron correction (N_g) and probability of staying in the first excited state assuming one electron in a quantum dot.

Higher occupation probability of the initial state of the transition increases the absorption of the quantum dots and leads to higher responsivity.

The next important quantity in Eq (6.43) is the linewidth Γ of the transition. The linewidth is mostly due to inhomogeneities caused by quantum dot size variations. This implies that the measured lineshape is a Gaussian superposition of Lorenztians with different resonant energies. Each line basically has an intrinsic width which is a superposition of the same relaxation rates, or lifetime processes of the carrier from the photo-excited state down to the lower levels. The intrinsic broadening processes are divided up into the phonon assisted relaxation rates and the escape rate W_{ec}. The final absorption broadening is around 30 meV and in general larger than the intrinsic width. Photocurrent lineshapes in undoped quantum dot structures have been studied[63].

In order to appreciate the importance of individual design steps it is necessary to remind what the individual physical phenomena that occur during the detection process.

The first step is the photon absorption step. It is desirable to have the highest oscillator strength for the selected wavelength. Though it is possible to absorb directly into the continuum, the problems are that a) such detectors are limited to high energies (< 4 μm) and b) oscillator strengths for bound-to-bound transitions are normally higher. The InGaAs/InGaP QDIP falls into b), even though the escape energy is still quite high with the escape barrier (E_{ec}) which is around 136 meV as shown in Figure 7.3.

The peak responsivity is shown in Figure 7.6 for different temperatures as a function of bias. Note that the responsivity is strongly bias dependent, and changes over five orders of magnitude for negative bias. It is asymmetric in this particular device, but this is because the dot escape barrier is not symmetric and lower towards the apex[44].

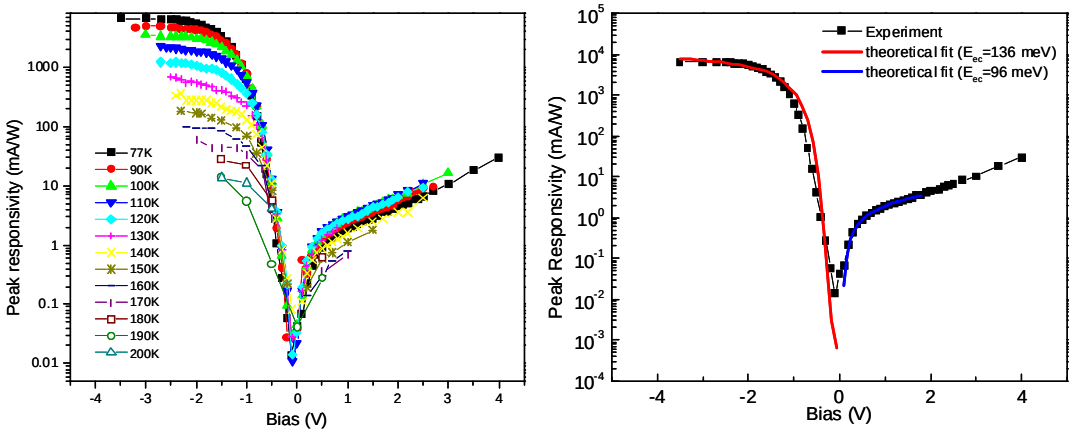

Figure 7.6 (Left) Experimental measurement of variation of peak responsivity as a function of bias at different temperatures (right) theoretical fits to peak responsivity at 77 K.

The exact shape of the offsets is a complex problem. It depends on the incidental barrier doping and dot growth conditions. The negative bias dependence is strongly tunnel-like and can be modeled by a simple formula which takes into account the sum total of all paths from the extreme activated (vertical) path, to the extreme tunnel path (horizontal) described in 6.3.1.

$$R = \left[\frac{e\alpha(\omega)L}{\hbar\omega}\right] g \left[\frac{\nu_{ec} e^{-E_{eff}/kT}}{\nu_0 + \nu_{ec} e^{-E_{eff}/kT} + \nu_t e^{-\Delta/kT}}\right] \qquad \text{Eq (6.45)}$$

According to Eq (6.45), the bias dependence of R(T,V) starts off very weakly until the bias reaches a critical value at which eFa is less than $\zeta\ kT(E_{ec})^{1/2}$, then the dependence is essentially that of Fowler Nordheim tunneling until the bias reaches eFa which is equal to $\zeta(E_{ec})^{3/2}$ at which point the barrier is destroyed and the bias dependence is now purely drift-limited ,which means R is proportional to μF.

$$R = const\left[\frac{W_{ec}}{\nu_0 + W_{ec} + \nu_t e^{-\Delta/kT}}\right] F^{\beta} \qquad \text{Eq (7.1)}$$

We have computed the bias dependence of R(T,V) at T=77K using Eq (7.1) with a field F which assumes that the absorption coefficient is essentially voltage independent in this range of interest. Indeed the normalized FTIR linewidth shows very small voltage dependence in this range. (see Figure 7.4)

The fit to the experimental data is shown in Figure 7.6 (right). The best escape energy for negative bias is 0.136 eV as predicted by theory and 0.095 eV at positive bias. The electric field factor was fixed to a power of $F^{0.6}$ rather than F. This gives a better fit at large F which suggests that the drift velocity V_d, which is equal to μF, is beginning to saturate at around $V_d \sim 10^7$ cm/s.

For the temperature dependence of R(T,V), the interplay between escape rate and absorption in the distribution is important both for the linewidth and the height. Here we note that when the responsivity reaches its voltage saturation region (see Figure 7.6 (left)) it results from mainly the lifetime shortening of the excited states due to faster multiphonon emission down in energy. This is especially true for those levels in the distribution of quantum dots which are more strongly bound, and which have a slower escape rate.

Gain, Dark and noise currents

The gain factor g in Eq (6.45)can be, in practice, deduced directly from experiment assuming the photoconductive gain and noise gain be same. To do this one uses the shot noise and generation-recombination (G-R) noise formula.

$$I_n^2 = 4eg_n I_{dark}\Delta f = 4eg_e FI_{dark}\Delta f \qquad \text{Eq (7.2)}$$

So if we know the noise currents and the corresponding dark current from the experiment, we can extract g(T,V) as a function of voltage and temperature. For InGaAs/InGaP/GaAs QDIP, the

noise is plotted against dark current in Figure 7.7. The noise and dark current were varied with voltage. Since the current is a strong function of V, we can write for the sake of argument

$$I_d = G_m V^m \qquad \text{Eq (7.3)}$$

where G_m is the corresponding proportionality constant. If the gain g stays linear in voltage, we can have the following relation.

$$g \propto V \propto (I_D)^{\frac{1}{m}} \qquad \text{Eq (7.4)}$$

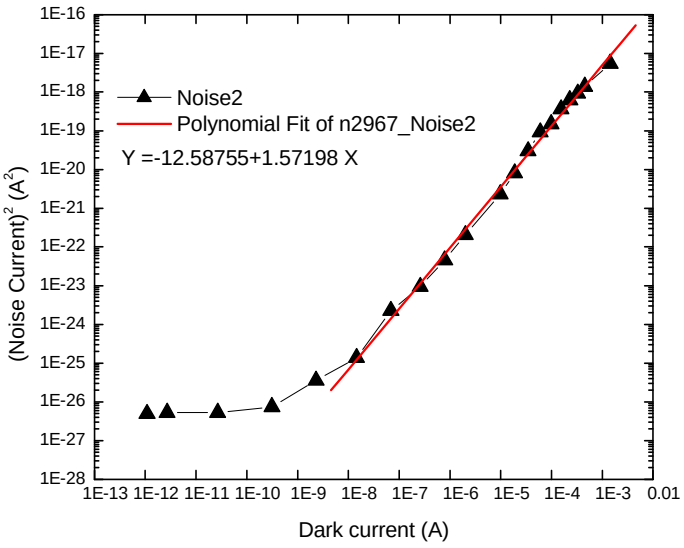

Figure 7.7. Noise current plotted as a function of dark current.

Then generally we can assume that the square of the noise is proportional to the power of p of the only dark current.

$$I_n^2 \propto (I_D)^p \propto gI_D \propto (I_D)^{\frac{1}{m}+1} \qquad \text{Eq (7.5)}$$

An effective exponent of the noise versus dark current of p=(1+1/m). In Figure 7.7, the linear fit over the high dark current region where the applied bias is high is very good and gives m=2 (1+1/m=1.57), which means the gain is proportion to the square root of the dark current.

Identifying the proportionality factor "g" with gain as defined by Eq (7.2) implies that the current really is one of generating and recombining carriers in a band. If as a result of inhomogeneous doping for example, the electrodes are not uniformly conducting and we have percolation paths, then the current density as defined as I_D/A can be seriously underestimated, giving anomalously large values of the gain. Note also that some authors, in analogy to QWIPs[50] assume that the recombination in QDIPs is drift limited. From this it would follow that the drift velocity dependence in the gain drops out and "g" can be a constant. This is however not justified in our devices, where the wetting layer scatters and reduces the band mobility, but is too thin to capture charge.

The actual voltage and temperature dependences of the dark current is shown in Figure 7.8. The dark current modeling is done in this section below.

Experimentally, in this device, a value of g=830 at V=-1.5 volts was derived. Given a band mobility of $\mu \sim 0.4\ m^2/Vs$, $L=10^{-6}$ m , we have a capture rate C_{be} of $\sim 10^{10}$ Hz, which agrees with the Monte Carlo estimates[56] and our own theoretical estimates,

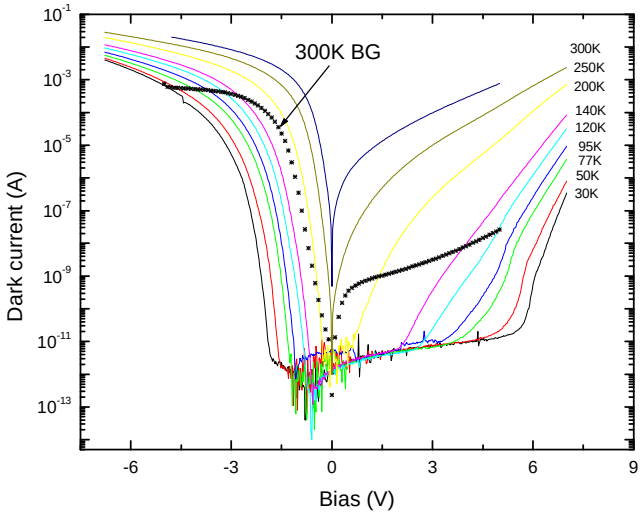

(a)

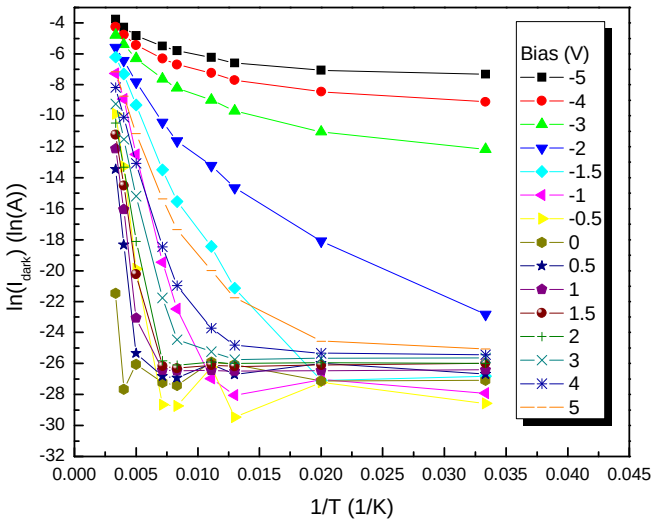

(b)

Figure 7.8. (a) Dark current as a function of bias for different temperatures (b) Arrhenius plots of the dark currents.

It means that with a field F of 2×10^6 V/m and a mobility μ of 0.5 $m^2/V\cdot sec$, a free charge will stay a time of 10^{-12} s before escaping to the electrode. In other words it takes much longer for the charge to be captured by a dot than to transfer across the device. It is also easy to see that with diffusivity D of 10^{-2} cm^2/s, the capture process is trapping limited and not diffusion limited, and that the rate C_{be} can therefore be calculated by taking the matrix element of an extended plane wave-like or Airy function with a localized dot eigenstate. The capture rate has been evaluated for a one-phonon optic and acoustic process. The answer is that the maximum rate C_{be} is a phonon frequency 10^{12}~10^{13} Hz multiplied by the probability that the electron localized in a quantum dot eigenstate ψ_e is sitting on a site or a bond in the quantum dot, i.e. $a^3\psi^*\psi$. This gives us C_{be} ~10^9 Hz which is the right answer as determined using the gain. In the limit of strong

electron -phonon coupling, the multiphonon relaxation step is not very different from this number, less than an order of magnitude slower[64, 65, 66].

$$I_{dot} = \frac{Ae\mu(F)FN_d}{(1-n_e)C_{be}} < g_s \nu_{sc} > \exp[-E_D(F)/kT], \qquad \text{Eq (6.64)}$$

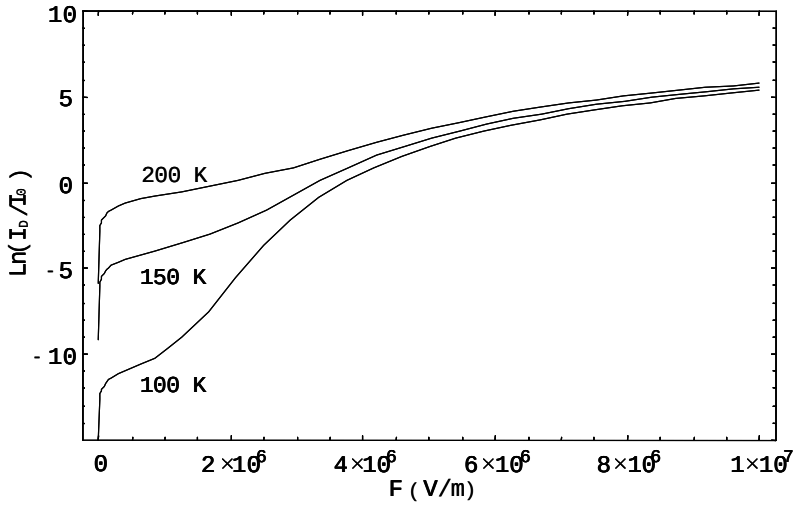

Figure 7.9. Calculated dark currents as a function of field with Fermi level fixed at -0.39 eV and electric field scaled by a factor of three.

The dark current, neglecting possible MY enhancement and the energy spread due to quantum dot size variations, from Eq (6.64) is plotted in Figure 7.9 as a function of field for three different temperatures. The Fermi level should in principle be evaluated self-consistently by matching injection current to dot escape current. The reason why this is necessary for a rigorous fit is that the barrier to injection is lower than the ground state ionization energy and extra charge is bound to accumulate in the dots, raising the Fermi level to a higher value. This implies that the assumption of neutrality is not completely satisfied and the Poisson field renormalization should also be included. For the simplicity, in order to show rough agreement and consistency, so we have fixed the Fermi level to -0.390 eV at V < -1V. The closest agreement is obtained if the

internal field across the quantum dot layers is assumed to be 3 times the average applied field. Note that the denominator $1+ f_s +[W_{sb_S} / C_{be}]$ in Eq (6.63) is taken ~ 1 because in this limit, the dots get replenished faster than charges escape. In the limit where the capture rate is faster than the release rate from a given quantum dot eigenstate, the denominators in Eq (6.63) can be neglected. In the opposite limit, at high fields for example, with shallow dot eigenstates, or when the quantum dot is boxed in and it is difficult to re-enter the quantum dot (i.e. when capture is slow compared to escape), we have the following picture:

Negative carriers enter the device to neutralize the positive charge of the ionized quantum dots and dopants, but instead of immediately recombining, most will simply now flow through the device, and produce a large dark current. The photocurrent is negligible in this limit because most of the dots are empty or nearly empty.

It is also important to note that the observed dark current is tunnel-like even at the highest temperatures. The change at T=300 K still involves seven orders of magnitude over a bias of 1 volt. This is a rare observation which also been made in a similar device[67] and can be understood from Eq (6.63) by noting that as the temperature, and probably also Fermi level, goes up, the occupation of higher quantum dot levels becomes likely, and the tunneling barrier decreases. Escape is tunnel limited from a given level when the escape energy E_{sb} satisfies (γa~0.45 from $\gamma a = a\sqrt{2m^*}/\hbar$)

$$\frac{eFa}{\gamma a E_{sc}^{1/2}} > kT \qquad \text{Eq (7.6)}$$

Looking at Figure 7.8, we see that for low temperatures the dark current does not change until the bias reaches a critical value, which itself decreases as we go up in temperature. The internal

field is of course somewhat space-charge renormalized so that a bias corresponds in reality to a higher tunneling field. In systems with more shallow bound states, and defect assisted escape, the dark current variation with voltage at similar temperatures is very much weaker[68].

Detectivity

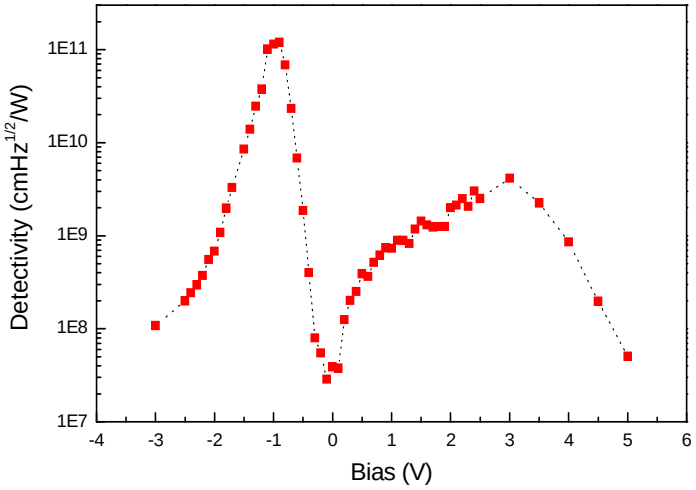

Figure 7.10. Specific detectivity of InGaAs QD/InGaP/GaAs QDIP as a function of bias at 77 K.

Depending on the device in question, the best D* is achieved at a given voltage and at a given temperature, the lowest temperature being 77K. The experimental data for InGaAs QD/InGaP/GaAs QDIP are shown in Figure 7.10. As we increase the bias the escape barrier from the excited state is eventually completely overcome and the responsivity saturates at -1.5V as shown in Figure 7.6. The noise is however more complex, since it involves dark current processes with higher escape barriers of up to 496 meV from the ground state, and much later bias saturation. The fact that the noise saturates later implies that the D* decreases again at a critical voltage as shown.

$$D^* = \left[\frac{\langle Q v_{ec} \rangle^{1/2}}{v_0 + v_t e^{-\Delta/kT} + \langle v_{ec} \rangle e^{-E_{ec}/kT}} \right] \frac{\langle \alpha(\omega,T) \rangle}{A^{1/2} N_d \hbar\omega} e^{(E_D/2kT - E_{ec}/kT)} \qquad \text{Eq (6.78)}$$

In the modeling of the peak detectivity Eq (6.78), the stronger temperature dependence at high bias (peak value) of D* is due to the dark current noise because the excited state escape barrier $E_{ec}(V)$ has been overcome. However, in our devices the exponential is not the only factor which controls the temperature dependence of D*. The decrease in D* is faster than what is expected just from the noise at peak bias, and involves unfortunately also the behavior of the absorbance with temperature. We have seen in Figure 7.6 that in our present category of strongly bias sensitive tunnel controlled devices, the responsivity R decreases very strongly with temperature, and we have argued that in these QDIPs with strongly bounded excited states, this is mainly due to the lifetime of the excited state becoming short compared to the escape time as we go up in temperature and multiphonon pathways override the low temperature bottleneck. In other words, the decrease is due to lifetime shortening, of which the lifetime shortening is the stronger one as we go beyond ~ 140 K. In QDIPs with shallow excited states[41], this problem has apparently been largely avoided, and the D*, though not better at low temperatures, maintains a high value of $D^* \sim 10^9$ $cmHz^{1/2}/W$ even at T= 200K. The temperature dependence of the devices of Ref 68 is indeed mainly due to the noise factor, as one would hope it to be, and as observed in the best QWIPs[60].

8 MWIR-QDIPs based on InAs Quantum dots on InP substrate

The most developed and researched material systems for QDIPs is InAs quantum dots with (Al)(In)GaAs matrix material[49, 69,70,71]. First the lattice mismatch between InAs and GaAs is around 7% and it is enough for self assembly method (SK growth mode). On the other hand, the lattice mismatch between InAs and InP is around 4 % and it is more than 3 % which is the lower limit required to have SK growth mode. Due to smaller mismatch between the quantum dot and substrate, narrower QD growth windows exist and thus make the optimum QD growth difficult. Another reason is that most quantum dot researches have been done with Molecular Beam Epitaxy (MBE) because it has more accurate control of the growth and in-situ characterization tool available such as RHEED (Reflection High Energy Electron Diffraction). So the quantum dot research or QDIP research using other materials are very limited, specially in InP system.

We have developed InAs/InP quantum dot infrared photodetectors by LP-MOCVD in Center for Quantum Devices.

Compared to the GaAs system, only a limited amount of work has been done on QDIP grown on InP substrates, and before we started InP based QDIP research, no device detectivity results have been reported [72,73]. In the case of QWIPs, high performance devices have been demonstrated with the InGaAs/InP system grown on InP substrates using metalorganic chemical vapor deposition (MOCVD)[74,75]. The high mobilities and low effective masses of the InGaAs/InP system give rise to high responsivity and long wavelength devices. Additionally, when compared to MBE epitaxy, MOCVD epitaxy has advantages such as relative simplicity, easy adaptability to industrial fabrication, and lower cost.[76]

Quantum dot is the key element of the QDIP device structure. Highly uniform high density quantum dots are required to achieve the predicted outstanding performance of QDIP. Ironically the major problem and challenge facing QDIPs come from the quantum dot growth. To detect a specific wavelength range, the appropriate dot parameters for that material system should be chosen based on the theoretical analysis. Especially, quantum dots with size and density required to achieve high detectivity at each detection wavelength should be grown.

Relationship between growth parameters and characteristics of quantum dots, such as dot size, dot density, dot size uniformity, should be studied in order to achieve high performance in QDIPs. Some important growth parameters such as temperature, the amount of material deposited, V/III ratio and ripening time can be optimized for quantum dots growth. For MOCVD, lowering the growth rate is limited technically (the smallest flow rate controlled by mass flow controller) in most cases. With systematic changes of those parameters, those effects are characterized with AFM, photoluminescence and TEM. The growth temperature is usually more complicated to determine the optimum range. The driving force behind QD nucleation and formation is the reduction of total energy in the strained material system. The nucleation rate is determined by deposition rate and surface coverage. Surface migration is determined by temperature and V/III ratio. The substrate temperature is a dominant factor for surface adatom energy during the quantum dot growth. The V/III ratio affects the incorporation of the surface adatom into the growth surface. The quantum dots can be initially grown on various matrixes such as InGaAs and InAlAs layers which are lattice-matched to InP. The thin layers play important roles. It is to prevent As/P exchange between the InAs quantum dot and InP barrier above.

8.1 Summary of previous work of growth and characterization of InAs quantum dots on InP

At the early stage of the study of InAs/InP quantum dot infrared photodetectors, we chose the quantum dot growth temperature at 500 °C after the effects of the growth temperature on the quantum dot formation were examined. In order to see the effects from the growth temperature, InAs quantum dot layers were grown at different temperatures such as 520 °C, 500 °C , 480 °C, 460 °C and 440 °C. During the QD growth, the flow rate is 50 sccm for TMIn (Trimethyle Indium) and 100 sccm for dilute arsine (5 % arsine in hydrogen). We observed that lower QD growth temperature caused lower mobility of the adsorbed atoms on the substrate surface and higher temperature caused higher coalescence rate between formed quantum dots. At high QD growth temperature such as 520 °C, the dot density was very low while at 440 °C, although the dot density was increased, the quantum dot starts to coalesce.

Another factor involved in determining the growth temperature of the quantum dots was the barrier quality. If the growth temperature of the barrrier above the quantum dots is lower than the optimum temperature of the barrier material, the performance of the device are strongly affected due to the degradation of structural, electrical and optical quality. Or if the growth temperature of the barrier is higher than the growth temperature of the quantum dot, careful growth should be made in order to avoid the evaporation of the quantum dot material while ramping up the growth temperature. At early stage of the work, the QD growth temperature 500 °C was also used as the optimium temperature for the barrier. It was found out that 500 °C was highest growth temperature with which we could obtain the high quality of quantum dots.

8.2 Low temperature growth of InAs quantum dots for MWIR QDIPs

8.2.1 Motivation

High QD growth temperature which was 500°C was used for the QDIP device at the early stage of my study. The QDIP devices utilizing 500°C QD growth temperature had a peak detection wavelength 6.4 µm. The peak detectoion wavelength 6.4 µm does not fall into the atmospheric windows whoes ranges are 3~5 µm (MWIR) and 8~12 µm(LWIR). Even though we demonstrated the first InAs QDIP and FPA whose peak detection wavelength was 6.4 µm, the practical application is very limited. Therefore we redirected our efforts to the development of high performance MWIR-QDIPs on InP substrates.

Through the optimization of the QD growth temperature, we observed the trend that the height of InAs quantum dots decreased as the QD growth temperature decreased but the lateral size did not change significantly. The typical lateral size of InAs quantum dots ranged from 30 nm to 40 nm, while the height ranged from 4 nm to 6 nm.

In Figure 8.1, the relative heights of quantum dots were shown. At 520 °C, the quantum dots were tallest while at 440 °C, the quantum dots were shortest. In the intermidiate temperature, the heights of quantum dots were stable to the growth temperature. Because the lateral size did not change signifcantly and the confinement is stronger in the growth directions than in the plane perpendicular to the growth direction, the strongest confinement was expected in the quantum dots grown at 440 °C.

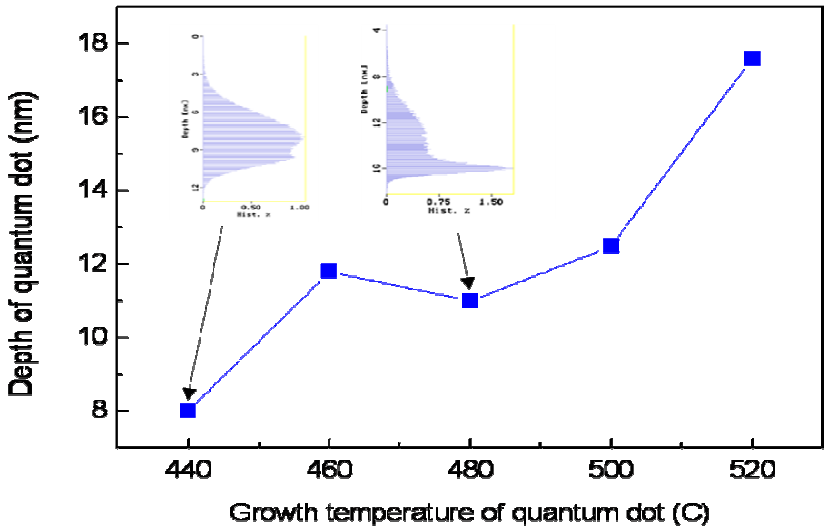

Figure 8.1. The relative heights of quantum dots grown at different temperatures.

This observation naturally made us think that the peak detection wavelength of QDIPs based on the low temperature QD growth might be shifted to shorter detection wavelength from 6.4 µm resulting from high QD growth temperature. As we optimized the InAs QDs grown at 440 °C, the optimized growth conditions for InAs QDs grown at 500 °C were examined first. The growth temperature is a global growth condition which affects the other growth condtions such as the growth rate, V/III ratio and ripening time. We studied and optimized the InAs quantum dot formation under different growth conditions at 440 °C. It was natural for us to start with the conditions which were used in the growth of InAs QD at 500 °C. First, the thin layer of GaAs was still grown at 440 °C. Later we will discuss the effect of the matrix on quantum dot formation.

8.2.2 Growth Rate

First we examined the effect of the growth rate on the quantum dot formation. The growth conditions for 500 °C were the flow rate of TMIn 50 sccm, the flow rate of dilute arsine 100 sccm and the growth time 12 seconds. The matrix was 1-nm thin GaAs layer on an InP buffer layer unless otherwise noted.

Starting from the optimized conditon for 500 °C, the 440 °C InAs QDs have been grown at the different growth rate by changing the flow rates of the TMIn and keeping the flow rate of the dilute arsine. Actually, we should have changed the flow rate of the dilute arsine in order to keep the same V/III ratio accordingly. For example, the V/III ratio of TMIn 50 sccm and dilute arsine 100 sccm is same as that of TMIn 100 sccm and dilute arsine 200 sccm. We used three different TMIn flow rates 50, 75 and 100 sccm and changed the growth time 12, 8 and 6 seconds respectively to ensure the amount of the InAs material was provided equally into the growth surface.

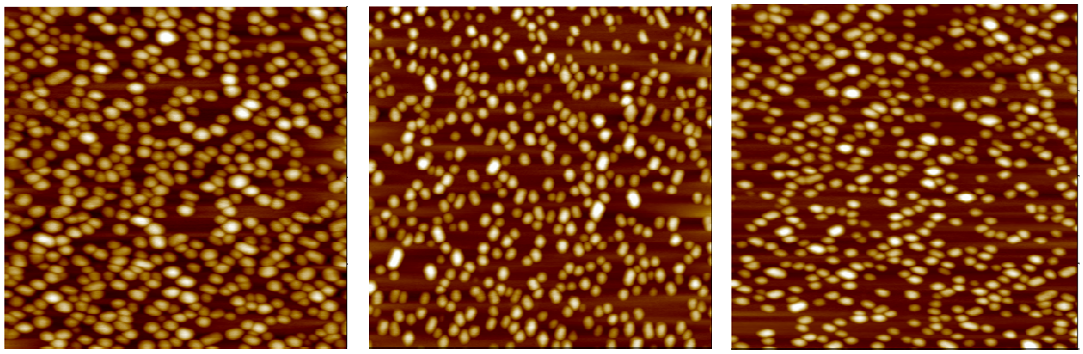

Figure 8.2. The AFM images (1×1 μm^2) of 440 °C InAs quantum dots on 1nm-GaAs on InP substrate with different TMIn flow rates and the flow rate of dilute arsine100 sccm. (Left) TMIn 50 sccm; (center) TMIn 75 sccm; (right) TMIn 100 sccm.

As shown in the Figure 8.2, the density of the quantum dots did not change very much. In order to investigate the quantum dot formation more carefully, we studied the statistics of the lateral size and the height of the quantum dots. The number of InAs quantum dots in 1×1 μm^2 were 396, 420 and 453.

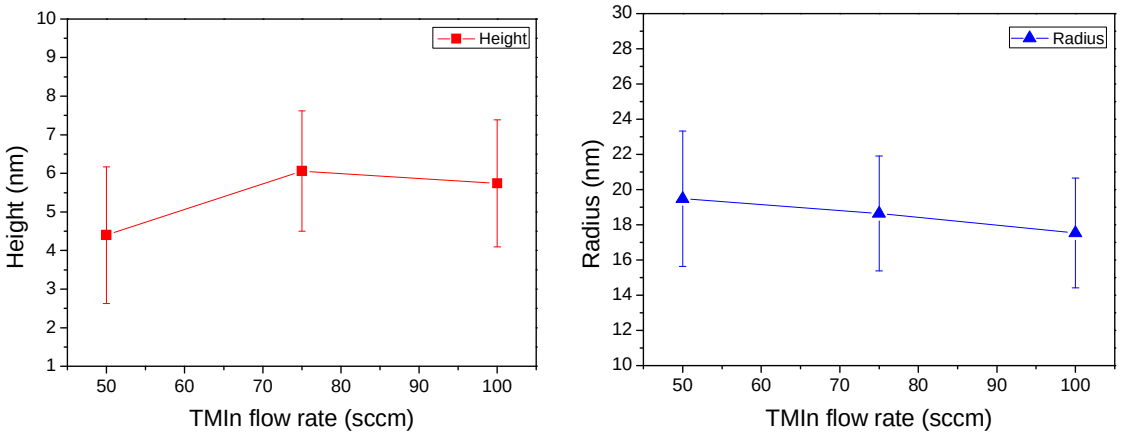

Figure 8.3. Statistics of the lateral size of InAs quantum dots under different growth rate.

In the Figure 8.3, the distributuions of the radius of the InAs quantum dots were shown. As shown in Figure 8.3, the clear trends of the height and the radius could be observed. The height seemed to increased and then decreased (or stablized), but the radius decreased as the QD growth rate was increased. Basically, as the QD growth rate was increased, the size of the quantum dots was decreased. The standard deviation of the radius and height were similar among the three samples. But the standard deviation of the QDs with highest growth rate was smallest among them. This was opposed to the observation where the higher growth rate leads to high density and less uniformity in the case of the conventional InAs quantum dots on GaAs substrates[77]. The change of the growth rate still was not significant in our case compared to the ones used in Ref. 77. In a MOCVD system, the actual growth rate of InAs quantum dots is difficult to find out

because there is no in-situ monitoring tool such as reflection high energy electron diffraction (RHEED) in MBE system. But we can guess the lower limit of the growth rate. The critical thickness of the InAs quantum dots on InP substrates is around 2.5 ML. If the amount of the InAs material provided were 3 ML during 12 seconds in case of the QD growth with TMIn 50 sccm, the lower limit of the growth rate would be 0.25 ML/s[78]. The change of the growth rate in this comparison ranged from 0.25 ML/s to 0.5 ML/s.

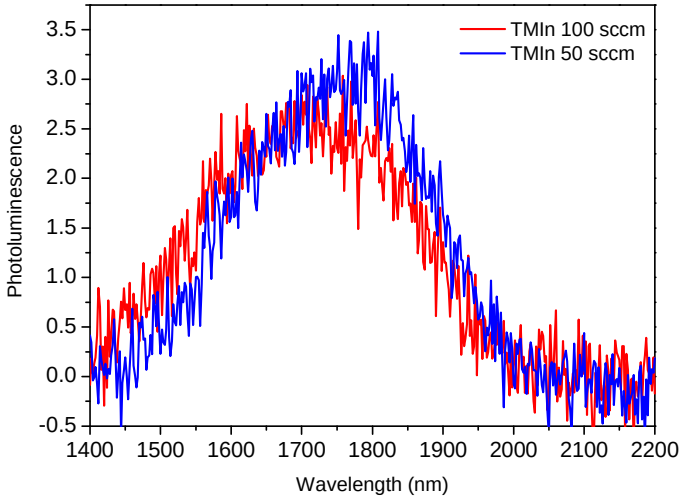

Figure 8.4. Room temperature photoluminescence from InAs quantum dots layers capped with InP. The quantum dot growth conditions are different in the TMIn flow rate.

The photoluminescence measurement can be a good tool to see the effect of the actual and capped quantum dot formation indirectly. We grew the InAs quantum dots layers capped with InP barrier material. The InAs quantum dot growth conditions were same as the ones with TMIn 50 and 100 sccm in Figure 8.2. As shown in Figure 8.4, the photoluminescence from two samples were very similar. The peak wavelength of InAs QDs grown at higher growth rate (100 sccm), was a little bit shifted to the higher energy side compared the one with slower growth rate

(50 sccm). This was consistent with the decrease of the size observed from AFM study. Because we prefer to have smaller quantum dots in the device, we chose TMIn 100 sccm for the InAs QD growth from now on unless otherwise.

8.2.3 V/III ratio

The V/III ratio is one of the important growth parameters to be optimized in order to grow a high quality of quantum dot layers. The effect of V/III ratio on the formation of QD was studied by changing the flow rate of dilute arsine. At the beginning of the InAs/InP quantum dot research, the pure arsine (AsH_3) was used. But with the change of the V/III ratio, the effect of the change was trivial. It was because the V/III ratio was as high as 500. It is well known that the high V/III ratio decreases the mobility of the adatom of indium and low V/III ratio is desirable for the quantum dot growth. The growth temperature was fixed at 440 °C. The growth structures and conditions were identical as above except that differetn flow rates of dilute AsH_3 were used during growth of InAs QDs. As shown in Figure 8.5, the dot density decreased while the V/III ratio increased.

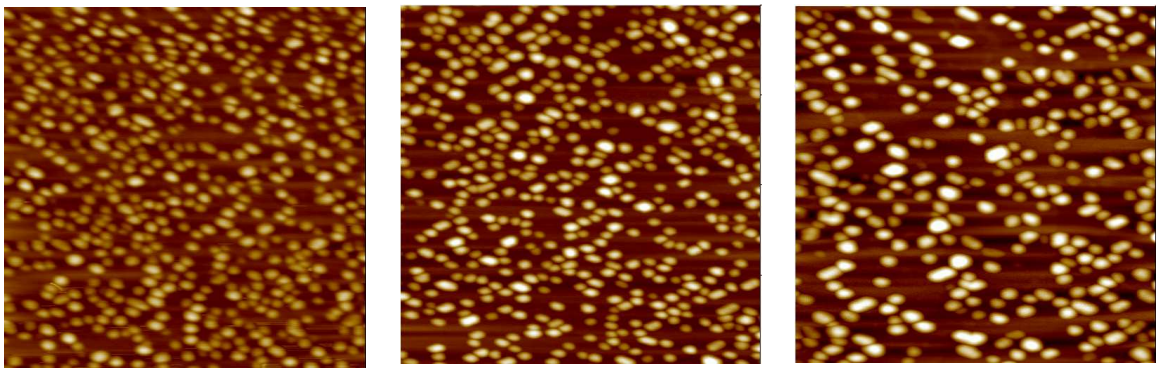

Figure 8.5. The AFM images (1×1 μm^2) of InAs QDs with different V/III ratio. (Left) V/III = 84; (center) V/III =126; (right) V/III = 168.

In order to quantify the V/III ratio, we can calculate the V/III ratio as follows. The V/III ratio is the ratio of the molar source flow rate of group V to the molar source flow rate of group III.

$$Z_a = \frac{10^6}{22400} \cdot \frac{P_{partial}}{P_{bubbler} - P_{partial}} \cdot \frac{T}{293} \cdot flowrate_a$$

$$Z_h = \frac{10^6}{22400} \cdot flowrate_h \qquad \text{Eq (8.1)}$$

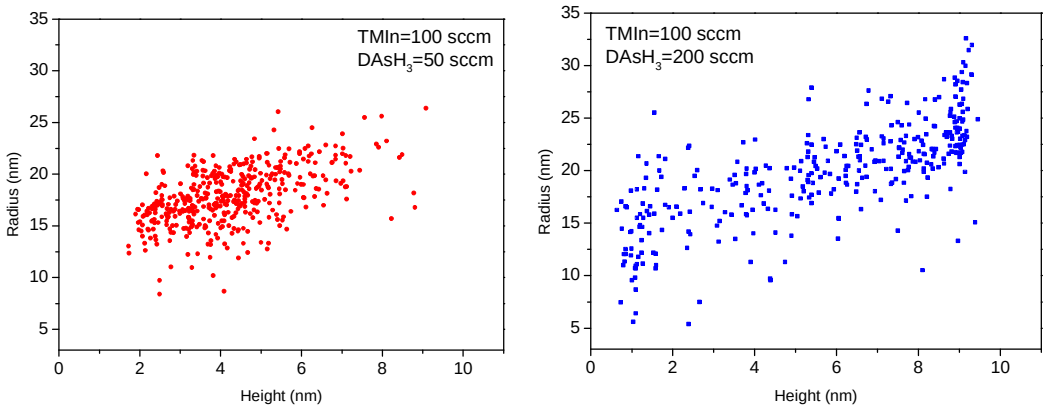

Figure 8.6. The correlation between the height and radius from the InAs QDs with (Left) V/III = 84 and (right) V/III = 168.

The molar flow rate of the group III (Z_a) is dependent on the group III bubbler pressure ($P_{bubbler}$), the partial pressure ($P_{partial}$), the bubbler temperature (T) and source flow rate ($flowrate_a$). The partial pressure of group III in Eq (8.1) is the vapor pressure (P_v) in the unit of mmHg (Torr) which can be obtained from $LogP_V = B - A/T$ where B is 10.52 and A is 3014 in case of TMIn. The resulting vapor pressure of TMIn is 1.73 mmHg with the bubbler temperature 20 °C. With the bubbler pressure 400 torr, the molar flow rate of TMIn 100 sccm is 1.32. The molar flow rate of 50 ssccm dilute arsine (5%) is 111.61. The resulting V/III is 84. As the V/III was increased,

the QD sizes got bigger and less uniform. The density also decreased. In high V/III such as 168, the bimodal distribution of InAs quantum dots was observed as shown in Figure 8.6. Therefore we chose the V/III ratio 84 as an optimum V/III ratio.

8.2.4 Ripening time

Ripening time is the time between the QD and the next layer when no growth occurs but the group V material is provided to protect the quantum dots. It gives time enough for adatoms of the quantum dot material to move around on the surface of the lowest energy and for the formation of the quantum dot. We grew the InAs quantum dots with different ripening times and under the other same growth conditions. The observed AFM images from those samples are shown in Figure 8.5. As the ripening time increased, the size of the quantum dots increased and the dot density decreased. When the ripening time increases, the time for the adatoms to migrate in the growth surface also increases. The indium adatoms try to find the lowest energy site to release the strain energy. When the growth temperature started to decrease, the mobile adatoms slow down and finally stop.

This is the case where uncapped InAs quantum dot layers form under different ripening times. But in the real device structures, the multiple stacks of the quantum dot and barrier layers are usually grown. In this case, the QD layers are covered with some part of the barriers which are grown at the same growth temperature as the QD growth temperature. The effect of the ripening time in the capped QD layers might be different.

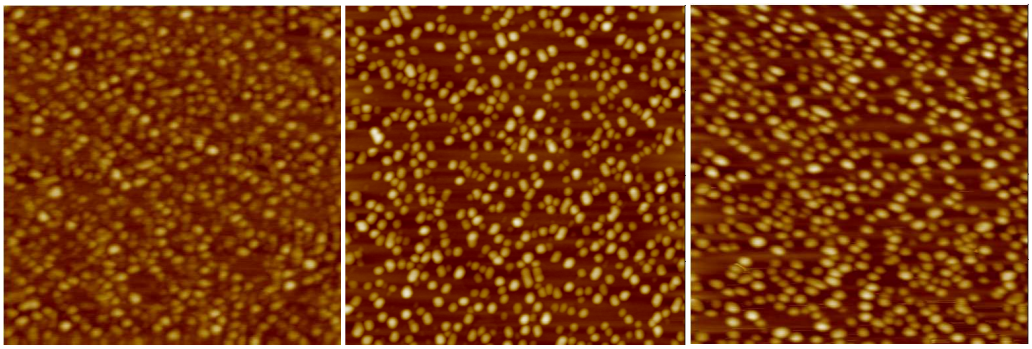

Figure 8.7. The AFM images (1×1 μm^2) of the InAs QD grown under different ripening times at the optimized conditions: T=440°C, TMIn=100 sccm, Dilute Arsine=50 sccm, growth time= 6s. (Left) 0 second; (center) 10 seconds; (right) 60 seconds.

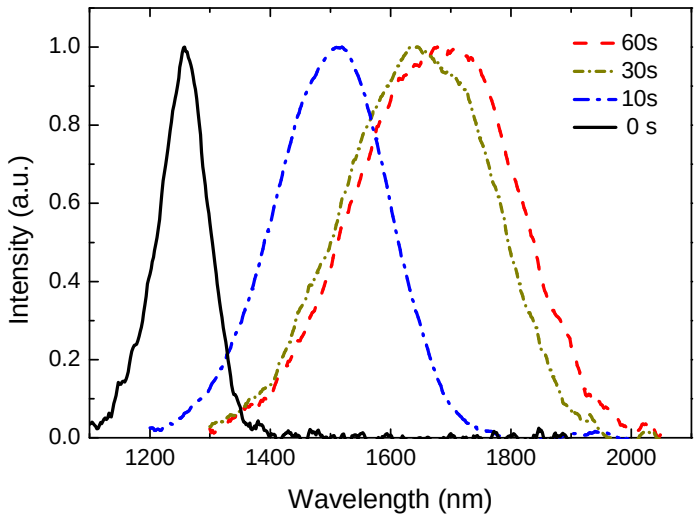

Figure 8.8. Room temperature photoluminescences of InAs QDs with InP cap layers. Different ripening times were used from 0 to 60 seconds.

In order to study the effect of capping process, cap layers were used after the QD growth otherwise during the cooling down the QDs on the surface might still be free to change. Photoluminescence (PL) was used for the characterizing the capped QDs with different ripening

times such as 60s, 30s, 10s and 0s. The growth temperature of InAs QDs and 40 nm-InP capping layers were 440 °C. Room temperature PL was measured as shown in Figure 8.8.

It can be seen that with the decrease of the ripening time, there is a continuous blue shift of the peak wavelength, decrease of FWHM and increase of the intensity, which may indicate that smaller size, better uniformity and higher density as observed in the AFM images of uncapped InAs QD layers in Figure 8.7.

Quantum dots mentioned above were grown at 440 °C for shorter wavelength QDIP device. For the quantum dots at grown at 500 °C with shorter ripening time, there is also a continuous blue shift of the peak wavelength as the quantum dots at grown at 440 °C as shown in Figure 8.9.

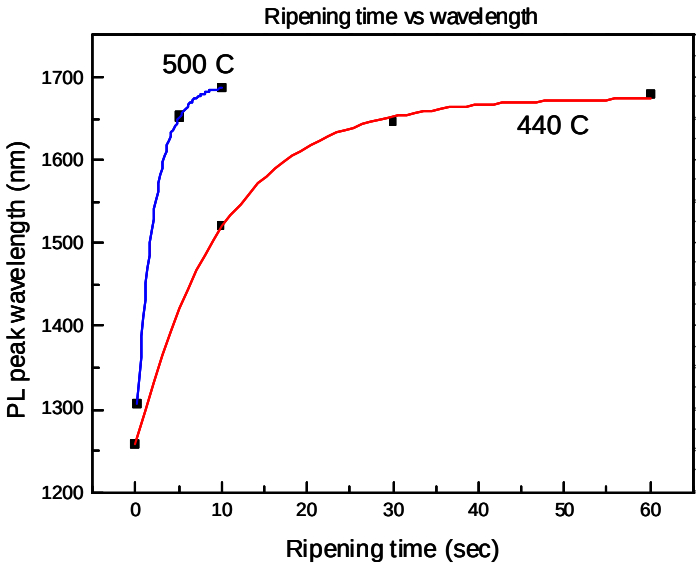

Figure 8.9. Photoluminescence wavelengthes as different ripening times and growth temperatures of InAs quantum dots.

At the QD growth temperature 500 °C, the PL peak wavelength increased more rapidly with the ripening time than at 440 °C because at the higher growth temperature of QDs, more energy was provided to the adatoms on the surface and the time of formation of quantum dots was reduced.

8.2.5 Comparison of different matrix material

From the early work of InAs QDs on InP substrates at CQD, it was found that the matrix underneath InAs QD layers could have significant effects on the dot formation. InAs QDs were grown on a 1 nm-$In_{0.53}Ga_{0.47}As$ matrix and on a 1 nm-GaAs matrix on an InP substrate. It was found that the InAs QD density and uniformity were improved by inserting a thin 10 Å strained GaAs layer between the InP barrier and InAs QD layer. The InAs QDs on a 1 nm-GaAs layer had higher dot density and better uniformity than on a 1 nm-$In_{0.53}Ga_{0.47}As$. It has been reported that such a thin GaAs layer could improve the uniformity and photoluminescence intensity from InAs QDs grown on InGaAs/InP matrix by preventing indium migration from the InGaAs layer to the InAs QDs[79]. So far we have characterized InAs QDs on a 1-nm GaAs layer grown on an InP buffer layer. In order to see the effect of the matrix on the quantum dot formation, we grew InAs QD layers on various matrix conditions. First, an InAs QD layer was grown on 1-nm GaP on an InP substrate. The 1-nm GaAs layer was replaced with a 1-nm GaP layer. In this case the more strain could be applied to the InAs QD layer due to the smaller lattice constant of GaP (5.45 Å) compared with that of GaAs (5.653 Å). As shown in Figure 8.7, the smaller and denser InAs QDs on a 1-nm GaP layer were observed in the AFM scan. Another matrix condition we investigated was 1-nm GaAs/3-nm $In_{0.52}Al_{0.48}As$/InP. The reason we investigated this condition

was due to the device structure we will discuss later. From the early work, it was found out that thin $In_{0.52}Al_{0.48}As$ layers underneath InAs QD layers could reduce the dark current and act as current blocking layers. There are studies about the effect of the buffer layer on the InAs QD formation on InP substrates[80,81]. It their studies, InAlAs and InGaAs buffer layers were used to compare InAs QD formations on buffer layers. They observed the blueshift and much narrower full width at half maximum.

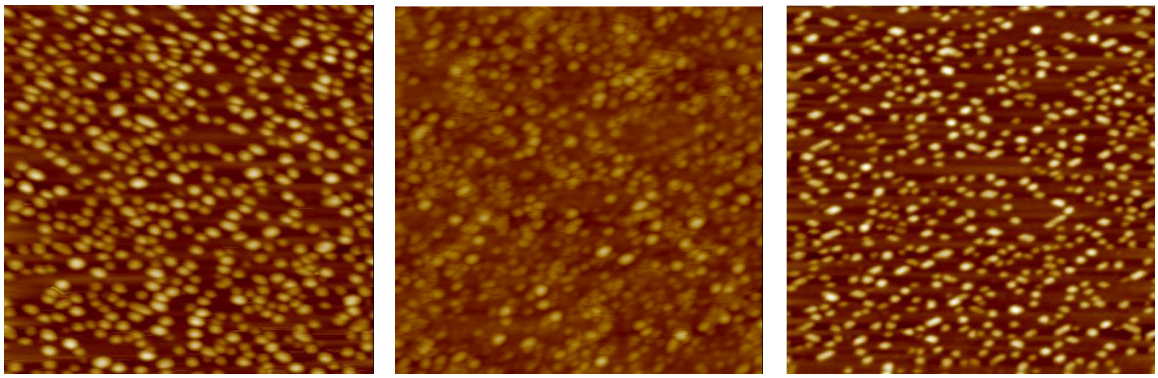

Figure 8.10. The AFM images (1×1 μm^2) of the InAs QD grown on different matrix conditions at the optimized conditions: T=440 °C, TMIn=100 sccm, Dilute Arsine=50 sccm, growth time= 6 s. (Left) InAs QDs/GaAs/InP; (center) InAs QDs/GaP/InP; (right) InAs QDs/GaAs/InAlAs/InP.

As shown in Figure 8.7, the AFM images of InAs QDs on different matrix conditions were compared. The InAs QDs grown on GaP/InP matrix showed different QD formation compared with the other InAs QDs. The density was very high and the sizes of InAs QDs were significantly small. The image processing program (SPM maginc) was used to calculate the distribution of the sizes. The height of InAs QDs/GaP/InP was 1.607±0.85 nm and the radius was 15.63±3.93 nm compared with 4.24±1.44 nm in the height and 17.85±2.76 nm in the radius in InAs QDs/GaAs/InP. On the other hand, InAs QDs on GaAs/InAlAs/InP had 3.75±1.56 nm of

the height and 14.31±2.58 nm of the radius. Especially the InAs QDs on GaP/InP was much shorter than the others. Actually we could observe the stronger confinement in InAs/GaP/InP in the photoluminescence as shown in Figure 8.8. The PL peak from InAs/GaP/InP was observed at 1.46 µm. The PL peaks from InAs/GaAs/InP and InAs/GaAs/InAlAs/InP were 1.7 µm and 1.65 µm. Later the energy difference 22 meV in the interband transition was the same as the difference in the intersubband transition from the devices with different matrix material. The difference might be caused by the stronger quantum confinement in GaAs/InAlAs/InP matrix.

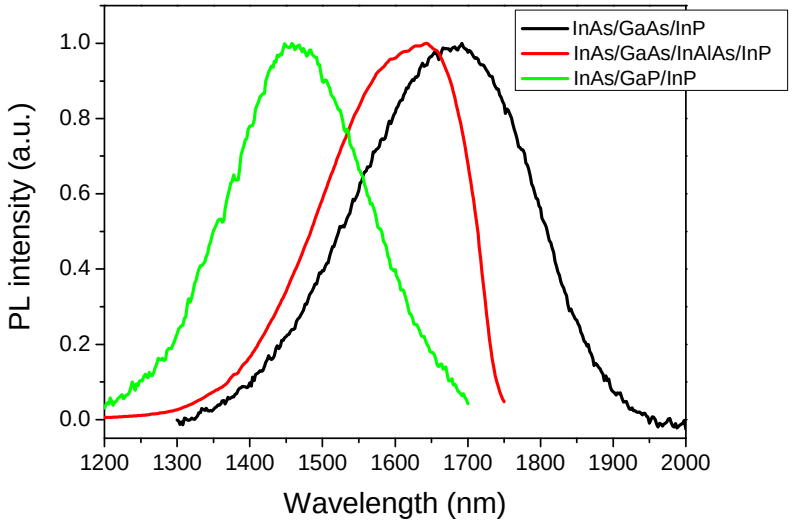

Figure 8.11. Room temperature photoluminescences of InAs QDs with different matrix conditions.

8.3 MWIR QDIPs based on low temperature grown InAs quantum dots

8.3.1 InAs/GaAs/InP-MWIR QDIP with two-step barrier growth

In the previous sections, low-temperature InAs quantum dots on various matrixes on InP substrates had been optimized through growth temperature, growth rate, V/III ratio and ripening time. In this section, we will discuss the QDIP device structure and their results.

At first we grew the active region (QD layer and barrier) at 440 °C. The device did not operate even at 77 K because of high dark current. The reason that the device did not operate ws that the quality of the barrier was so poor that the leakage current (dark current) was much larger than the photocurrent. It is well known that the quality of the barrier is important for the QDIP device to operate. In order to overcome the problem related to the poor quality of the barrier, we introduced the two-step barrier growth technique. This technique has been used to grow the multistack quantum dot layer with less defects and better quality of barrier than the normal growth technique. In our device structures, a thin layer of the barrier (capping layer), which covered the quantum dot layers, first was grown at the same growth temperature as the QD growth temperature (440 °C in our case). Then the growth was interupted with group V flowing and the tempearture was increased to the optimum temperature of the barrier (590 °C in our case). After the temperature got stablized, the rest of the barrier was grown. The two-step barrier growth was applied to each layer and repeated with a number of the stacks of the device. Due to the large number of the stacks (>10), it took long time to grow the device structure.

We grew two device structures with 5 nm and 10 nm of InP capping layers. The total thickness of the barrier was kept constant 40 nm as shown in Figure 8.12.

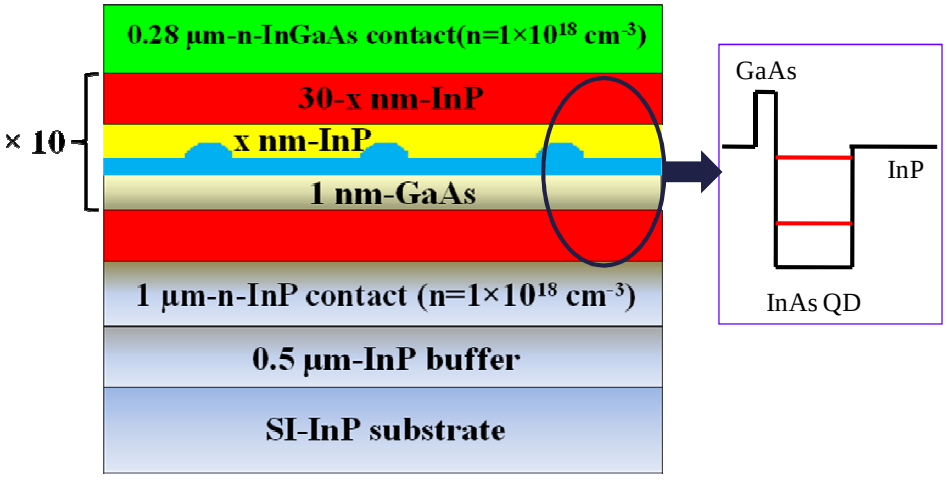

Figure 8.12. Schematic illustration of the MWIR-QDIP device structure grown with two-step barrier growth. x nm-InP capping layer was grown at the same temperature as the QD growth temperature 440 °C. The rest (30-x) nm-InP barrier was grown at high temperature 590 °C. Inset shows the schematic diagram of the conduction band alignment.

The InAs QD layers were grown on 1 nm-GaAs/InP matrix with 100 sccm of TMIn and 50 sccm of dilute arsine for 6 seconds. The ripening time was 30 second. The other device parameters were same including QD doping level and contact doping level.

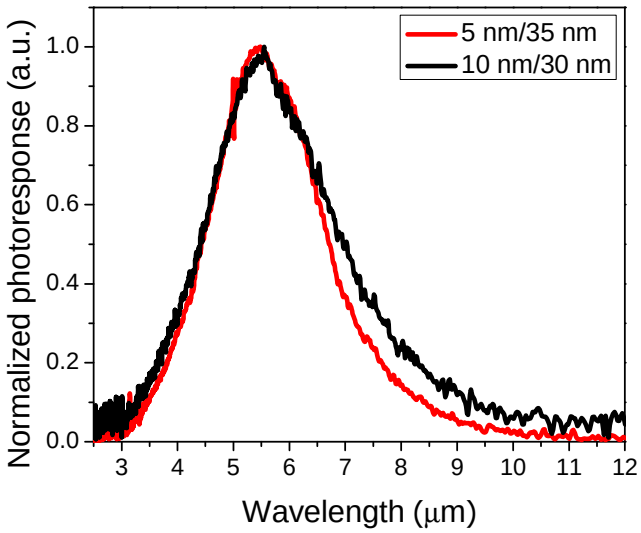

Figure 8.13. Normalized photoresponses at 77 K and and a bias of 0.2 V from MWIR-QDIP device structures grown with two-step barrier growth.

Due to the improvement of the material, we were able to observe the spectral response by Fourier transform infrared spectrometer (FTIR) for the normal incidence configuration. From both devices, the peaks were observed at 5.54 μm at 77 K and a bias of 0.2 V. The photoresponses were caused by the bound-to-continuum transition which usually results in the broad spectral response (>40 %).

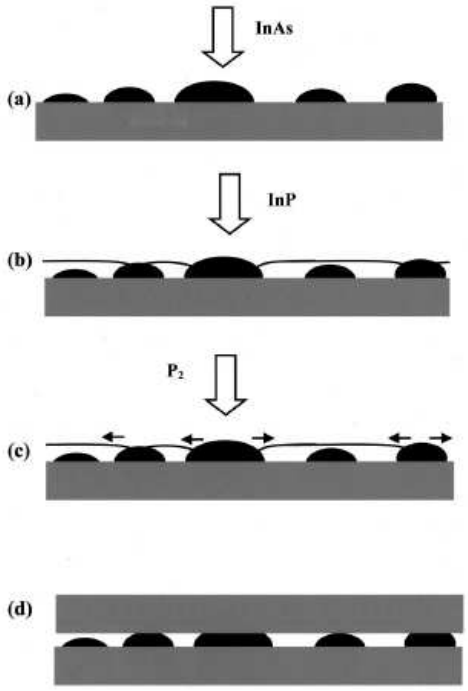

Figure 8.14. Schematic diagrams of the InAs QD growth with the overgrowth with a thin capping layer. (a) InAs QDs were formed on 1-nm GaAs/InP matrix. (b) A thin capping layer of InP which takes palce between islands, is deposited. (c) A growth interrupt under PH_3 overpressure on the growth front and the growth temperature was raised up to 590 . (d) The whole structure was capped with the rest InP layer [82].

There was a slight difference observed in the tales at long wavelength region in that the device with a 5 nm-InP capping layer had narrower response. The reason might be that the big InAs QDs which were taller than the thickness of InP capping layer (5 nm) would be capped and become smaller as illustrated in Figure 8.14. This process eventually made the InAs QDs more uniform..

Another effect of the two-step barrier growth on the device performances was lower dark and noise currents. As shown in Figure 8.15, the dark current and noise currents from two QDIP devices with different InP capping layers were compared. The dark current and noise current from the device with thinner capping layer (5 nm) and thicker high temperature barrier (35 nm) was lower by more than one order of magnitude compared to the device with 10 nm/30 nm barrier. Because the detectivity of the device with 5 nm/35 nm barrier had better than that of the device with 10 nm/30 nm barrier, we will mainly discuss the performance of the device with 5 nm/35 nm barrier.

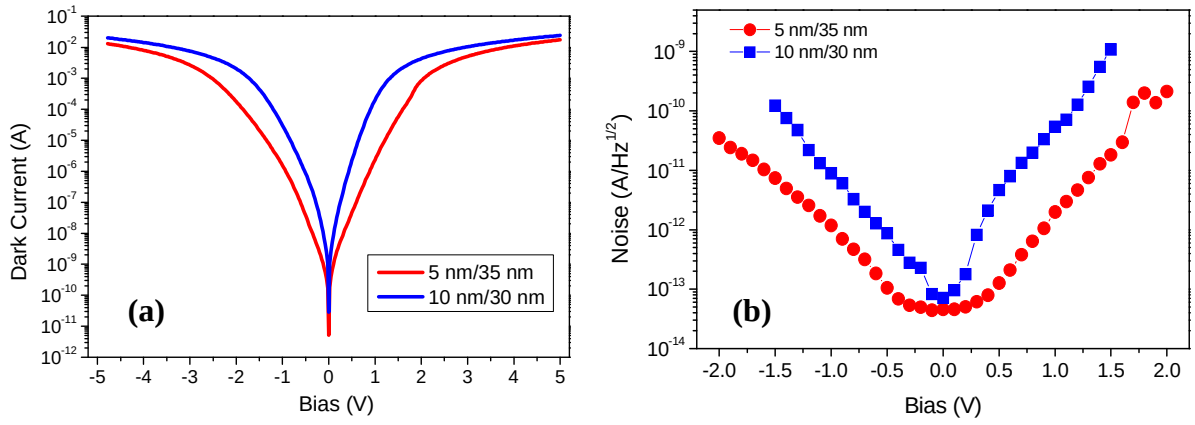

Figure 8.15. Comparison of the dark currents (a) and the noise current (b) from the devices with different two-step barrier growth (5 nm/35 nm and 10 nm/30 nm).

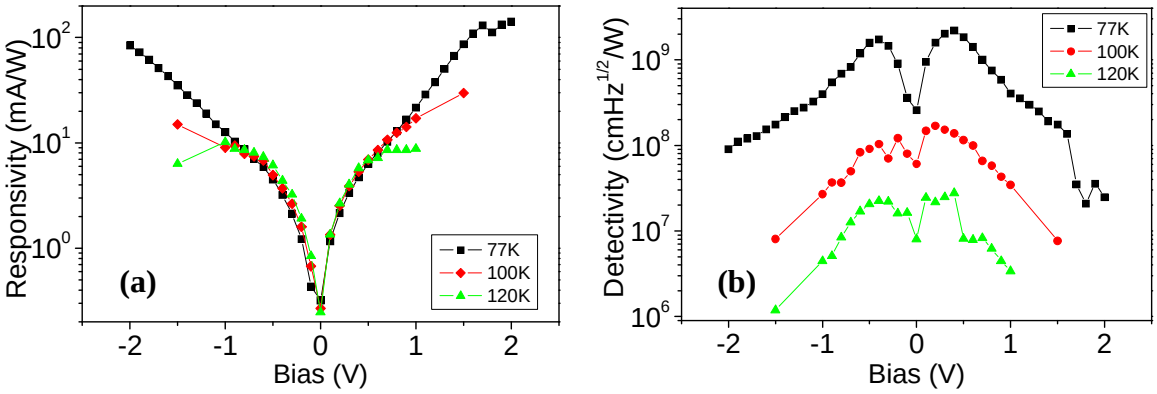

Figure 8.16. MWIR QDIP device performances from InAs QDs/GaAs/InP with 5/35 nm two-step barrier growth. (a) Peak responsivity (R_p) at different temperatures as a function of applied bias; (b) Dark current density at different temperatures as a function of applied bias.

The absolute magnitude of the blackbody responsivity (R_{bb}) was determined by measuring the photocurrent (I_p) with a calibrated blackbody source that was set at 800ºC. The test mesa was illuminated from top of mesa with normal incident infrared radiation. Peak responsivity (R_p) has been calculated in the same way as described in page 64, and the results at 77 K, 100 K and 120 K are shown in Figure 8.16 (a). At T=77 K and bias of 2V, a peak responsivity of 0.142 A/W was observed for this MWIR-QDIP. The peak responsivity at 100 K (120 K) didn't change around from -0.9 V to 0.8 V (0.5 V), but at higher biases, the responsivity decreased compared to that of 77 K. The detectivity (D*) can be calculated from $D^*=R_p(A\cdot\Delta f)^{1/2}/i_n$, where $A=1.375\times10^{-3}$ cm^2 is the illuminated detector area and Δf=1Hz is the bandwidth. The detectivity of the QDIP as a function of bias at both T=77 K, 100 K and 120 K are shown in Figure 8.16 (b). The highest detectivity of this QDIP was 2.2×10^9 cmHz$^{1/2}$/W and the quantum efficiency was 1 % at a bias of 0.4V at T=77K. The reason that the detectivity

changed significantly as a function of the operating temperature was that the noise current increased but the responsivity remained constant at the bias range between -0.9 V and 0.5 V.

8.3.2 InAs/GaAs/InAlAs/InP-MWIR QDIP with current blocking layer

The $In_{0.52}Al_{0.48}As$ current blocking layer (CBL) on top of the InAs QDs has been proved to be very effective in decreasing the dark current and noise current in 6.4 μm QDIP due to higher bandgap of InAlAs than that of InP[45]. The InAlAs CBLs were incorporated into the current MWIR-QDIP device in order to decrease the dark current and noise current further. Another motivation was to decrease the peak detection wavelength. The MWIR-QDIP based on InAs/GaAs/InP had a peak around 5.5 μm. Only 26 % of the photoresponse was covered between 3 to 5 μm. Each $In_{0.52}Al_{0.48}As$ CBL was grown below the quantum dot layer because good quality of the $In_{0.52}Al_{0.48}As$ could be grown at 590 ^{o}C.

The InAs QD growth condition on GaAs/InAlAs/InP matrix was described in 8.2.5. The device structure was shown in Figure 8.17.

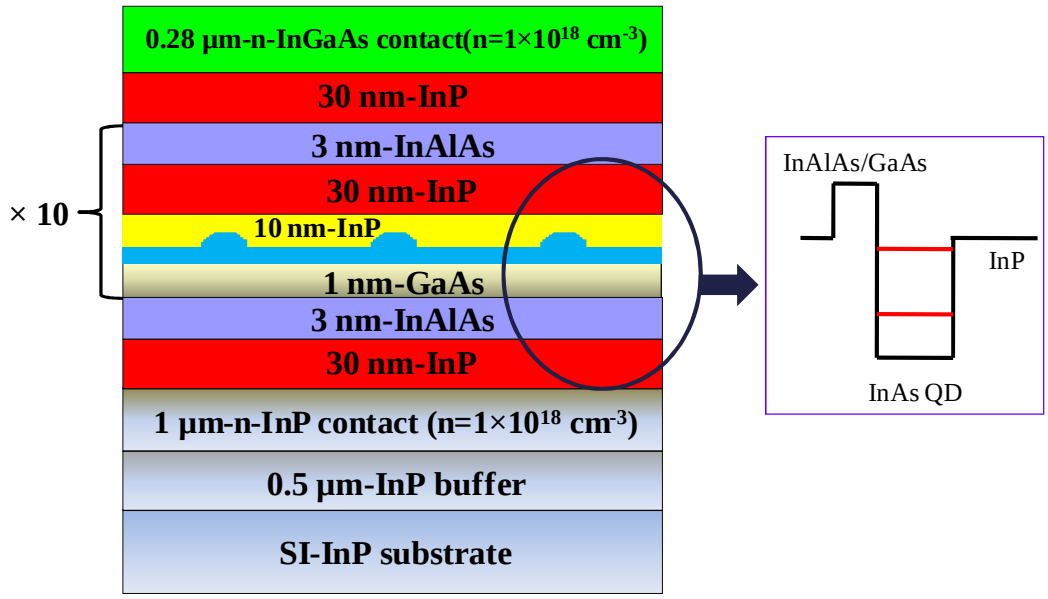

Figure 8.17. Schematic illustration of the MWIR-QDIP device structure grown with two-step barrier growth and InAlAs current blocking layers (CBLs). 10 nm-InP capping layer was grown at the same temperature as the QD growth temperature 440 °C. The 30 nm-InP barrier and 3 nm-InAlAs CBL was grown at high temperature 590 °C. Inset shows the schematic diagram of the conduction band alignment.

Before we discuss the device results, we will discuss the transmission electron microscope images showing the actual cross-section of the current device structure as shown in Figure 8.18. The bright field imaging condition is usually used to observe the quantum dots by the effect of the strain field on diffracted intensity. Due to the strain effect, careful analysis should be done in order to interpret the actual QD size and shape. It is well known that the bright field imaging is useful to observe the defects. While (200) dark field image can be used to analyze the shape and size of the quantum dots. The (200) dark field images of our MWIR-QDIP

are shown in Figure 8.18 (a) and (b). The InAs QDs appeared as bright regions with a dark halo, sitting on top of a thin wetting layer, which is dark thin layer in the picture.

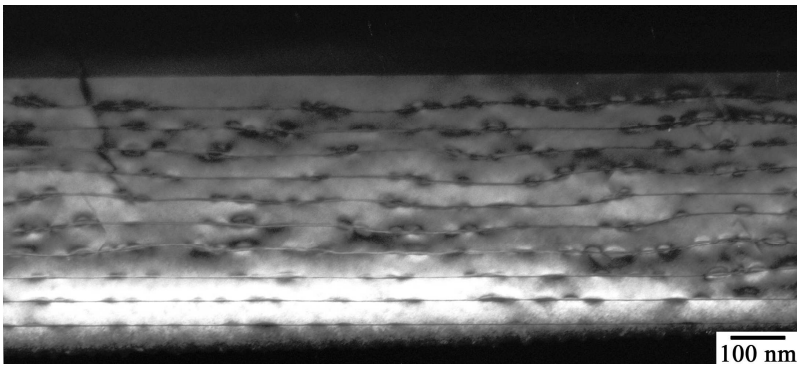

(a)

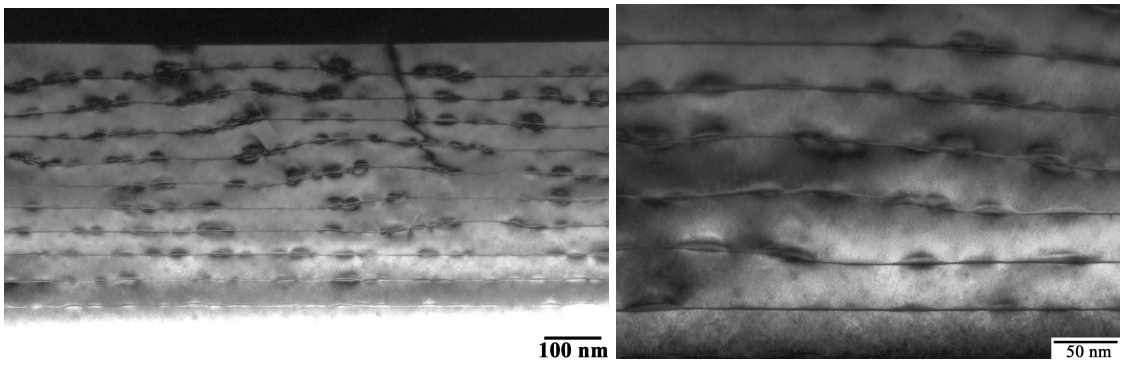

(b) (c)

Figure 8.18. Transmission electron microscope (TEM) images of MWIR-QDIP device with InAs QDs/GaAs/InAlAs/InP and 10/30 nm two-step barrier growth. (a) Bright-Field image showing overall structure; (b) (200) Dark-field image of the overall structure; (c) Magnified (200) dark-field image of the first few layers of the structure.

This contrast has its origin in the well-know compositional sensitivity of the 200 reflection. From the study of the experimental data and simulation of the 200 dark field image, the outside of the dark halo is known to be a better measure of the dot dimensions[83]. The estimated QD size is

around 30~40 nm in lateral dimension and 5~7 nm in height. In both cross-sectional bright and dark field images, the undulation in a quantum dot layer originated and propagated into the upper layers. The buried big defective QDs might be the reason for the undulation.

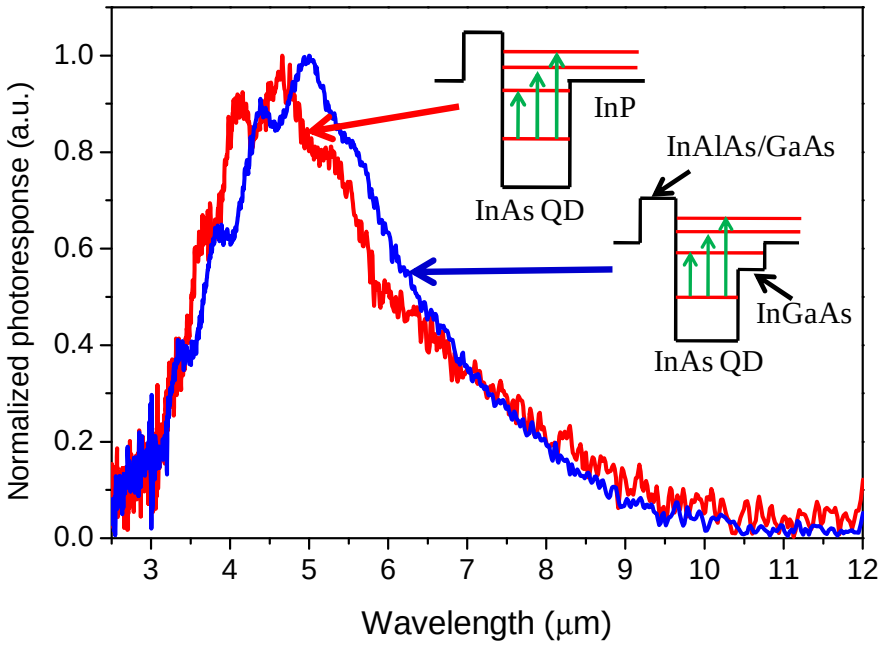

Figure 8.19. Normalized spectral photoresponses measured by FTIR at 77 K and a bias of 0.4 V. The red curve represents the spectral response from an InAs/GaAs/InAlAs/InP-QDIP. The blue curve represents the spectral response from a device with same structure except with 3nm-$In_{0.53}Ga_{0.47}As$ capping layers above the InAs QD layers.

We fabricated the single detector mesa in order to characterize the device performaces. First, we observed the relative photoresponse by Fourier transform infrared spectrometer (FTIR). In order to understand the origin of the peaks in the photoresponse, another device structure with 3nm-$In_{0.53}Ga_{0.47}As$ capping layers above the InAs QD layers was grown and its photoresponse was measured. The 3 nm-InGaAs layer was supposed to reduce the confinement of the InAs QDs

so that the red-shift of the photoresponse could be observed as shown Figure 8.19. As shown in the Figure 8.13, this broad photoresponse indicated that the transition fell into the category of the bound-to-continuum or quasi-continuum transition. But the multiple peaks occurred at 3.75, 4.1, 4.66 and 5.3 μm in the photoresponse of the InAs/GaAs/InAlAs/InP-QDIP. We suppose the multiple peaks were originated from the multiple minibands formed by periodic structure of alternating InP layer and InAlAs layer. The photoresponse from the device with the InGaAs capping layers also had similar multiple peaks but shifted to longer wavelength compared to that of the device without the InGaAs capping layers.

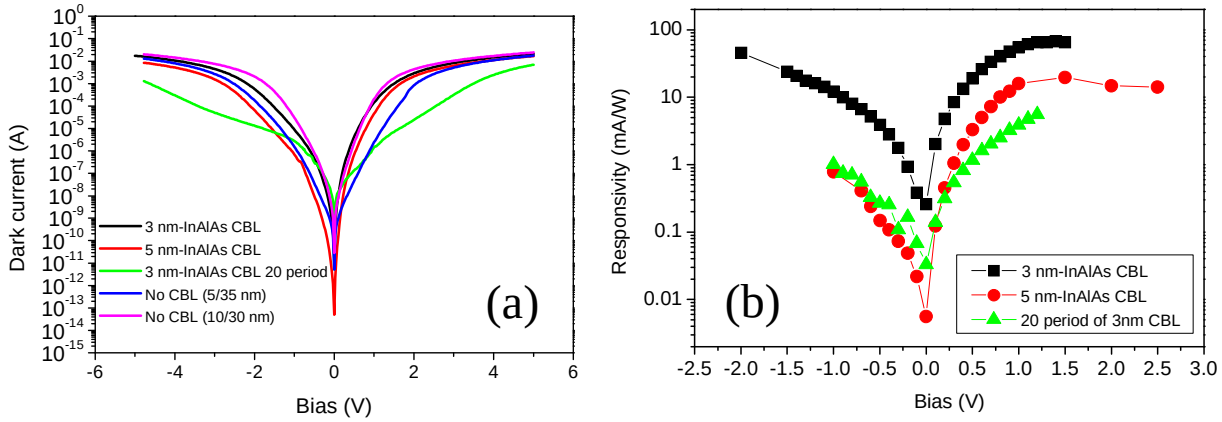

Figure 8.20. (a) Comparison of the dark current and (b) comparison of the peak responsivity at 77 K from the MWIR-QDIP with InAlAs CBLs with different thickness, no CBLs and 20 period of active region of 3 nm-CBL structure.

In order to optimize the thickness of the current blocking layer, the QDIP devices with different thickness of CBLs were compared. At the same time, the number of period of the 3 nm-CBL structure was doubled to 20. All the dark currents were compared at 77 K as shown in Figure 8.20. Actually the dark currents without CBLs were not significantly lower than the dark current with 3 nm-CBLs. But the dark current with 5 nm-CBLs was lower than any other device

structure with 10-period active region. The dark current of the device with 20-period CBLs seemed to be lowest, but if the applied electric field was considered instead of applied bias, the dark current was similar to those of 10-period CBLs. As seen from comparison of the dark currents, the lowest dark current could be realized with 5 nm thick InAlAs CBLs.

The peak responsivity was compared as shown in Figure 8.20. The 5 nm-InAlAs CBL device and 20-period device had lower responsivity than 3 nm-InAlAs CBL device. All of the above responsivities were lower than those of devices without InAlAs current blocking layers (CBLs) in Figure 8.16 (a). The reason was that the InAlAs CBLs did not only reduce the dark currents but also the photocurrent because the dark current and photocurrent follow same transport of the carriers in the devices. For the application of focal plane arrays, high responsivity and low dark current are preferred. If the dark current levels are similar, the device structure with high responsivity should be chosen.

The overall performance can be compared through the detectivity as shown in Figure 8.21.

The highest detectivity was obtained from the device with 3 nm-InAlAs CBLs among three different device structures. The detectivity of 1×10^{9} $cmHz^{1/2}/W$ was obtained at 77 K and a bias of 0.2 V.

In conclusion, we optimized the growth conditions of the InAs QDs such as the growth rate, V/III ratio and ripening time with fixed QD growth temperature (440 °C). The matrix condition underneath InAs QDs affected the dot formation. The matrixes we studied were 1 nm-GaAs, 1 nm-GaAs/3 nm-InAlAs and GaP on InP buffer layers. Those optimized conditions were used in the device structures and compared to find out the best condition.

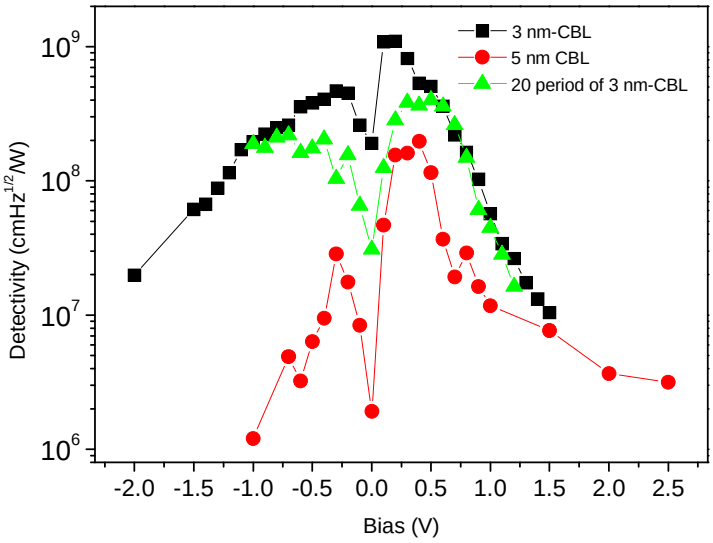

Figure 8.21. Comparison of the detectivity at 77 K from the MWIR-QDIP with InAlAs CBLs with different thickness, no CBLs and 20 period of active region of 3 nm-CBL structure.

Transmission electron microscope revealed the actual cross-sectional device structure. We could observe InAs QDs, some defects and specially undulation of the layers. We investigated two kinds of MWIR-InP based QDIP structures based on InAs QDs grown on InP substrates. One was 10 period of InAs QDs on 1 nm-GaAs/InP matrix. The barrier layers between InAs QD layers were grown at two different growth temperatures (440 °C and 590 °C) in order to have good quality of the barrier. The peak detection wavelength was 5.54 μm and $\Delta\lambda/\lambda$ was 41 %, which indicated the bound-to-continuum transition. The highest detectivity of this QDIP was 2.2×10^{9} cmHz$^{1/2}$/W and the quantum efficiency was 1 % at a bias of 0.4V at 77 K. The other structure we studied was based on InAs QDs on 1 nm-GaAs/3 nm-InAlAs on an InP buffer layer. The peak detection wavelength was 4.66 μm and $\Delta\lambda/\lambda$ was 55 %, which also indicated the bound-to-continuum transition. The highest detectivity of this QDIP was 1×10^{9} cmHz$^{1/2}$/W and the quantum efficiency was 1 % at a bias of 0.2V at 77 K.

9 High-performance InAs quantum-dot infrared photodetectors grown on InP substrate operating at room temperature

So far we have discussed the MWIR-QDIPs based on the InAs QDs on InP substrates. Although the performance of quantum dot infrared photodetectors is expected to be better than that of quantum well infrared photodetectors, the developed QDIPs were not better than the current state of the art QWIPs. The problems we had in the quantum dot system were following. First, it is very difficult to control the desired detection wavelength by adjusting the QD growth conditions and barrier material. Especially the growth condition which most affected the detection wavelength was QD growth temperature. In InAs/InP material system, it was found out that the low QD growth temperature was necessary to have the detection in MWIR range. When the QD growth temperature was far from the optimum temperature of the bulk material which usually was used in the barrier growth in the device structures, the material quality of the device structure could be degraded severely. Even though two-step barrier growth technique could be implemented to improve the barrier quality, it was not avoidable that the problem could come from the interface between the quantum dot and capping layer. In our TEM study, the defects related to the defective big QD were observed as shown Figure 8.18. The defects in the multi-quantum dot layer structure form percolating conducting channels through which the carriers can transport[84]. It also decreases the photocurrent by capturing the photoexcited carriers in the device. In order to realize the low dark current and high photocurrent in the QDIP system, we had to change our approach. One of the advantages that QWIPs have is the relative easiness of the control of the detection wavelength compared with QDIPs. By adjusting the thickness of

quantum well layers in the active region, the desired detection wavelength can be achieved. But the main disadvantage is difficulty of achieving high operation temperature due to the 1-dimensional confinement. In our novel approach, we tried to combine the quantum dot and quantum well in order to have high operating and high performance MWIR photodetectors. First we had to develop the quantum well infrared photodetector which detects the MWIR region.

9.1 MWIR-QWIP based on InGaAs/InAlAs/InP system

Previously at CQD, the MWIR-QDIP based on InGaAs/InAlAs/InP system was developed with gas-source molecular beam epitaxy[85]. In this section, we will discuss material growth by LP-MOCVD and characterization to have best material quality in this material system. Then, the resulting QWIP device structure and performance will be discussed.

9.1.1 Material growth and characterization

In the quantum well infrared system, all the material can be grown at the optimum conditions. Especially the growth temperature can be fixed to the optimum growth temperature of all bulk material 590 ^{o}C. Here we revisited the material (InGaAs and InAlAs) optimization for InGaAs/InAlAs/InP QWIP.

InGaAs

InGaAs is an important alloy because $In_{0.53}Ga_{0.47}As$ is lattice matched to InP and has a lower bandgap energy. It serves as quantum well absorbing infrared light in the QWIPs. It is very important to have high quality of the material.

In order to optimize the growth of InGaAs, 0.5 µm InP buffer layer was first grown at optimum condition. The growth temperature was 590 °C and bulk InGaAs was grown. The lattice match condition was obtained by adjustiing th flow rates of TMIn (90 sccm) and TEGa (46 sccm) and arsine (100 sccm). The growth rate was 0.8 µm/h.Under the optimized condition, the as grown sample showed excellent morphology with very few defects. X-ray diffraction show near lattice match as shown in Figure 9.1 The 10 µm × 10 µm AFM shows stomic steps and a RMS of 1.4 Å, as shown in Figure 9.1.

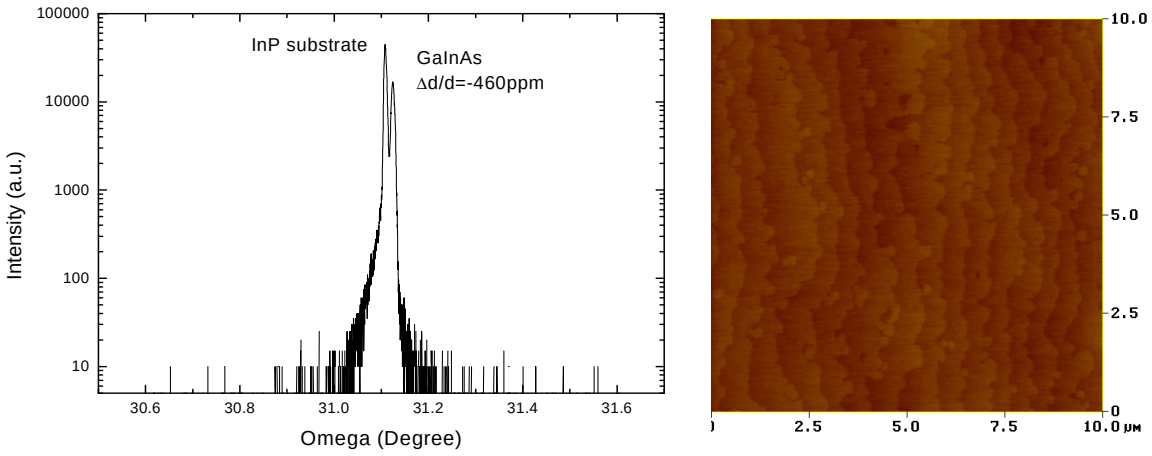

Figure 9.1. X-ray diffraction and surface morphology of InGaAs grown at 590 °C.

Hall measurements have been done at both room temperatures (RT) and liquid nitrogen (LN) temperature-77K. For the 0.5 µm-InGaAs sample grown at 590 ^{o}C, RT Hall measurement shows a mobility of $\mu=1.05\times10^{4}$ cm^2/Vs with carrier concentration $n= 5.13\times10^{15}cm^{-3}$. At 77K, it shows a mobility of $\mu=1.1\times10^{5}$ cm^2/Vs with carrier concentration $n= 4.54\times10^{15}cm^{-3}$.

1000 and 200 ppm Silane/Hydrogen mixture gases were used as n-typed dopant for InP contact layer and InGaAs quantum well. For doping profile calibration, usually a step structure is grown with different silane flow rates, high to from bottom to top then measured by ECV. A typical

ECV calibration of such structure is shown in Figure 9.2. The structure consists of 3 half-micron InP layers grown at 590 ^{o}C with 50 ppm dilute silane flow rate of 400, 200 and 100 sccm. It can bee seen that the carrier concentration is linearly proportional to the silane flow rate within this range. This ensures good control of the doping profile. Specifically, 400 sccm gives a carrier concentration of about 10^{18} cm^{-3}, which is the proper level for contact layer.

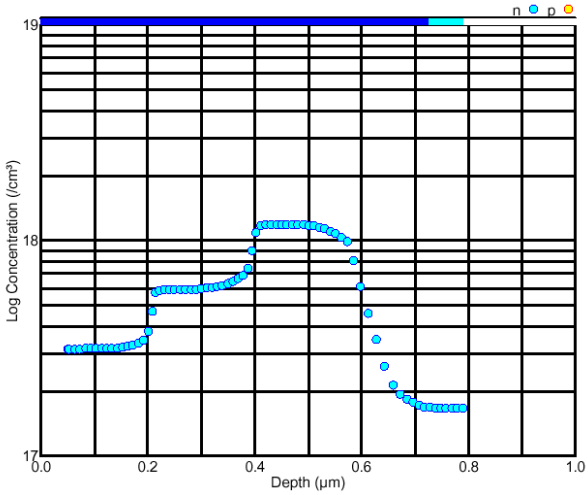

Figure 9.2. ECV profile of a InP “steps” with differetn dilute silane flow rates.

InAlAs

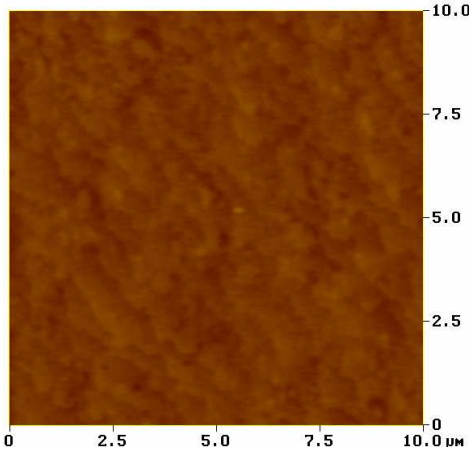

Figure 9.3. Surface morphology of InAlAs grown at 590 °C from AFM.

$In_{0.52}Al_{0.48}As$ layer was used as the barrier layer in the device structure. It is very important to have high quality material in the device structure. We optimized the growth conditions in order to have good structural and electrical qualities.

9.1.2 MWIR-QWIP structure

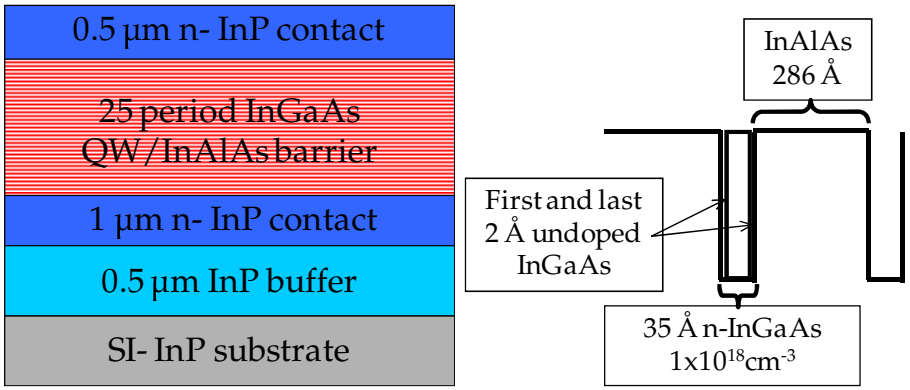

Figure 9.4. (Left) Schematic of InGaAs/InAlAs QWIP structure and (right) detailed structure of an InGaAs QW layer and an InAlAs barrier layer.

The design of the QWIP structure was shown in Figure 9.4. This design was developed by C.L. Jelen[85]. The bottom and top InP contact layers had a doping concentration of 1×10^{18} cm^{-3}. The number of the InGaAs layers was 25 and the barrier thickness was nominally 28.6 nm. In order to have the MWIR detection whose peak is 4 µm, the thickness of InGaAs QW was nominally 3.5 nm. Only 3.1 nm of the center of InGaAs QW was doped to 1×10^{18} cm^{-3}. The structural quality of the QWIP structure was excellent as shown in Figure 9.5.

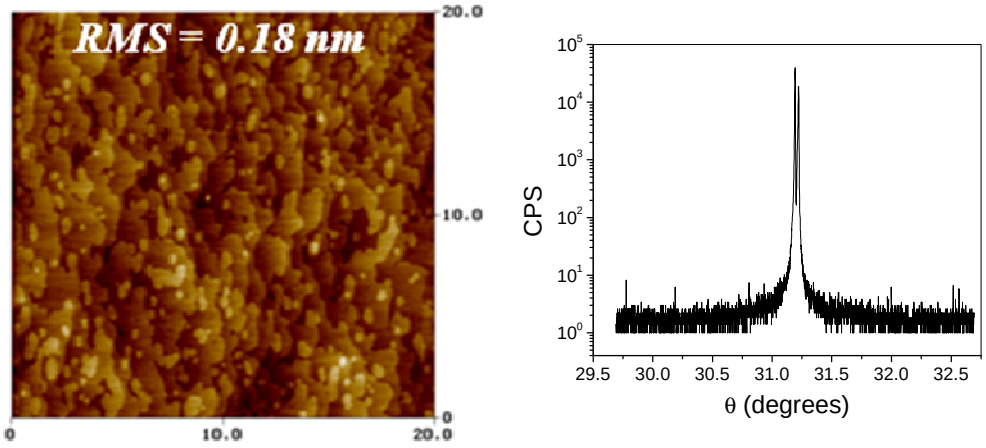

Figure 9.5. (Left) top surface morphology of the grown QWIP device structure and (right) x-ray diffraction of the grown QWIP structure.

The 20 µm× 20 µm AFM of the top surface of the device showed very smooth morphology with RMS roughness 0.18 nm. The x-ray diffraction revealed almost perfect lattice match of InGaAs and InAlAs to InP substrates because no satellite peak was observed.

9.1.3 MWIR-QWIP device result

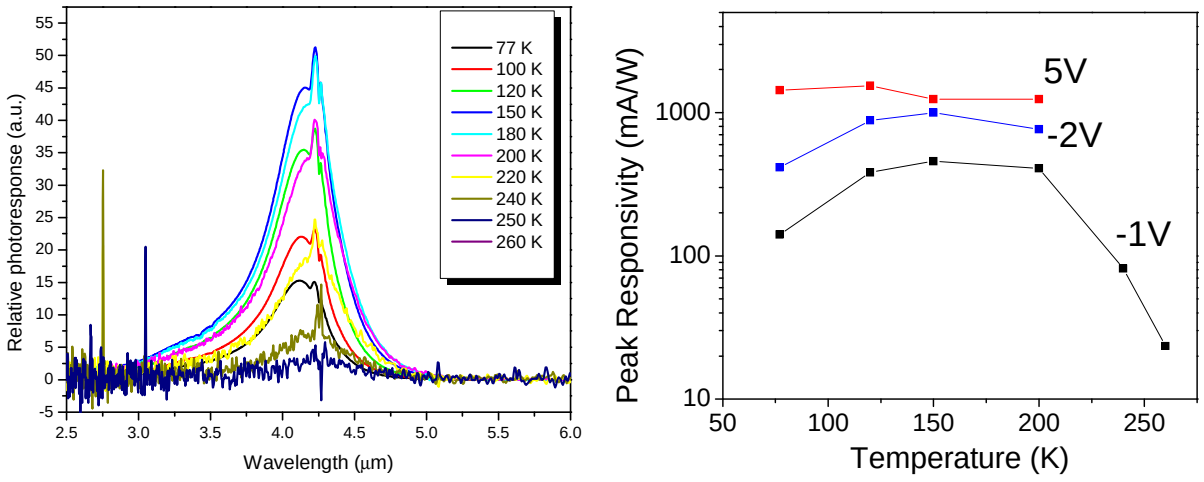

Figure 9.6. (Left) Relative photoresponse of MWIR-QWIP measured as a function of the temperature at a bias of -1 V and (right) peak responsivity as a function of temperature at some biases.

The MWIR InGaAs/InAlAs/InP QWIP has a peak wavelength of 4.1μm with a full width at half maximum of 0.116μm. The peak shape was relatively independent of the temperature. The peak responsivity as a function of temperature for various biases is shown in Figure 9.12. The peak responsivity was as high as 1 A/W at higher biases and maintained this value at high temperatures.

The temperature dependent detectivity is also shown in Figure 9.7. The detectivity values at each temperature were presented at the bias that gave the highest detectivity. Despite the relatively weak dependence of responsivity on temperature, the detectivity decreases steadily with temperature due to the increase in noise and dark current as a function of temperature. The detectivity at 77 K was 2.7×10^{11} $cmHz^{1/2}/W$ with quantum efficiency of 3.3 %.

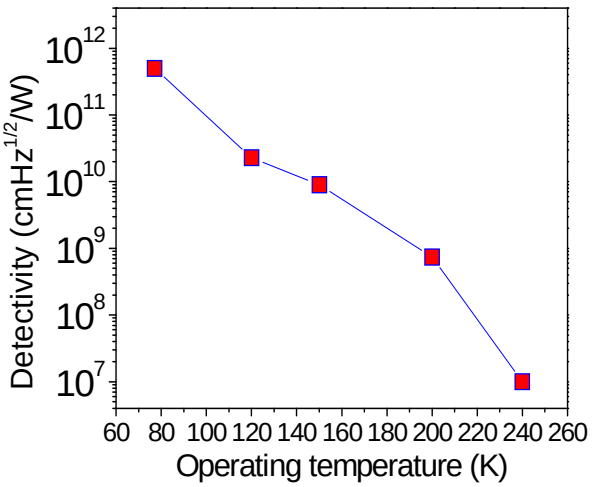

Figure 9.7. Maximum detectivity as a function of temperature.

The reasons that we had such a good temperature behavior even with this QWIP structure are following. First, the InGaAs/InAlAs/InP material system has a very large conduction band-offset which is favorable to the reduction of the dark current. Second we had high quality material. But the temperature performance of the QWIP had still room to be improved.

9.2 MWIR-QDWIP based on InAs/InGaAs/InAlAs/InP system

Even with the quantum well, we had an excellent MWIR-photodetector. The highest operating temperature was 240 K. In order to improve the performance of the QWIP further, the InAs QD layers were inserted below InGaAs quantum well layers in the device structure. From now on, we call it quantum dot-quantum well infrared photodetector (QDWIP). The motivations of inserting the InAs QDs in the QWIP structure were two-fold. One was the decrease of the dark current and the other one was the increase of the quantum efficiency.

The decrease of the dark current could be expected due to the fact that the undoped QD layers constituted highly resistive materials. The InAs QD layers play the same role as current blocking layers. However they do not significantly decrease the photocurrent because the escape of the photoexcited carriers is not seriously affected and the recombination time is longer than in simple QDs.

The increase of the quantum efficiency can be expected due to the fact that the hybridization of the quantum dot and quantum well wavefunctions in the ground state might lead to higher oscillator strength to the incident infrared light. We will discuss more physics related to the device performance later.

One of the challenges we had in order to realize the quantum dot-quantum well system was the growth of the InAs quantum dot layer at high temperature. In conventional QDIP structures, the QD growth temperature is typically lower than the optimum bulk growth temperature. In the new system, the InAs QDs were grown at the same temperature as the barrier layer and the quantum well layer at 590 ^{o}C. The other challenge was that we did not want to shift the detection wavelength of the device due to the existence of the InAs QD layers. Therefore, the size of the InAs quantum dots should be small enough not to change the intersubband transition significantly.

9.2.1 High temperature growth of InAs QDs for QD-QW system

In order to determine the matrix material for the InAs QDs, we grew the InAs quantum dot layers on 3 nm-InGaAs/3 nm-InAlAs layers and 3 nm-InAlAs/3 nm-InGaAs. The big differences between InAs/InAlAs and InAs/InGaAs were observed in terms of the dot density and the size as shown in Figure 9.9. They are mainly associated with the indium surface segregation on the front growth of the two matrix materials[86]. The great intrinsic surface InAs enrichment of the InAlAs buffer will go against alloying with the InAs deposit. The intrinsic surface roughness due to surface segregation, which is higher for the InAlAs layer than for InGaAs layer, favors nucleation because of the sites provided. This explains the higher density and smaller size of the InAs quantum dots on an InAlAs layer compared to those on an InGaAs layer. Obviously the InAs QDs on InGaAs/InAlAs matrix were much bigger than the InAs QDs on InAlAs/InGaAs matrix. Therefore we determined InAlAs/InGaAs as a matrix for the quantum

dot growth. Its determination naturally leaded to the device structure. The InAs QDs should be below the InGaAs quantum well layer and on InAlAs barrier layer.

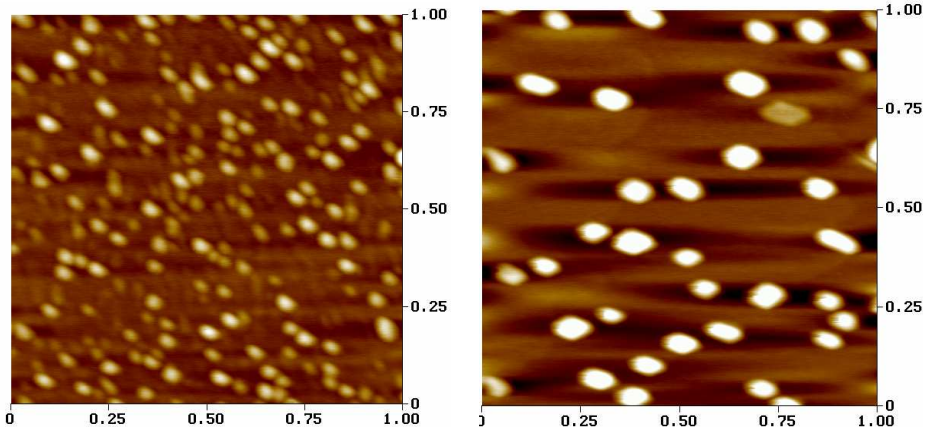

Figure 9.8. AFM images of the InAs quantum dots with TMIn 120 sccm and 2.7 s grown on (left) an InAlAs layer; (right) an InGaAs layer.

Next, we studied the effect of various quantum dot growth conditions on the quantum dot formation. The growth parameters we investigated were the growth rate and amount of quantum dot material.

First, in order to see the effect of the QD growth rate, we changed the growth rate and growth time while compensating the growth time to deposit nominally the same amount of InAs material. We started with the original growth conditions from a flow rate of 70 sccm TMIn and a growth time of 3.6 seconds.

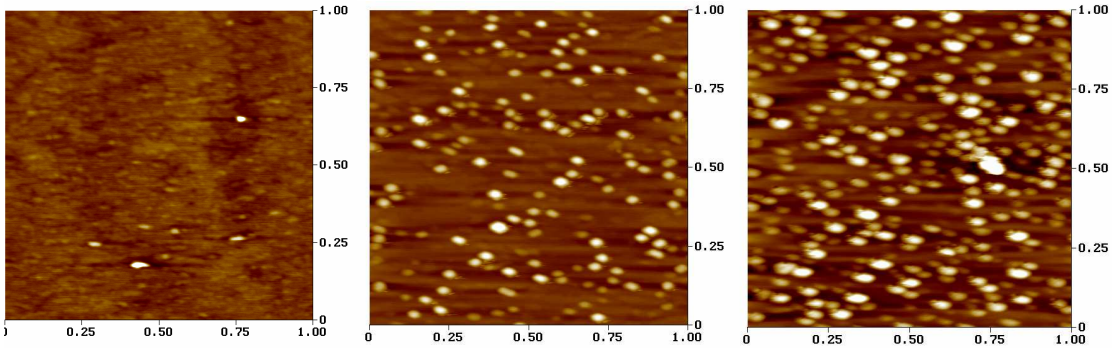

Figure 9.9. AFM images of the InAs quantum dots on InAlAs with different growth rates (left) TMIn 70 sccm and 3.6 s; (center) TMIn 35 sccm and 7.2 s; (right) TMIn 17.5 sccm and 14.4 s.

Then the flow rate of TMIn was decreased to 35 and then 17.5 sccm, and the growth time was increased to 7.2 and 14.4 seconds, respectively. As shown in Figure 9.12 as the growth rate decrease the number of quantum dots increased from 94 to 260 in a 1 μm region and the lateral size increased from 31.2 nm to 36.8 nm. With the lowest growth rate, extremely larger islands, which can form defects, started to form. Those changes led to slightly larger and denser quantum dots. This result illustrates the importance of quantum dot engineering.

We increased the TMIn flow rate from 70 to 90 sccm for 3.6 seconds. As expected, the dot density increased compared to that of the quantum dots with 70 sccm. The results of the complete series of growth are shown in Figure 9.10. In this set of growth rate conditions, the optimum condition was the one with 120 sccm TMIn flow for 2.7 seconds. The dot density was 2.4×10^{10} cm^{-2} (240 in 1 μm^2 surface). The average dot lateral size was 20±4 nm and the average height was 5±2 nm. The relation between the growth rate and the dot density in the InAs/InAlAs/InP system was opposite to that in the conventional InAs/GaAs system where higher growth rates give higher dot densities[87]. The reason for this abnormality might be related

to the non-linearity of the amount of the material deposited on the surface as a function of the growth time.

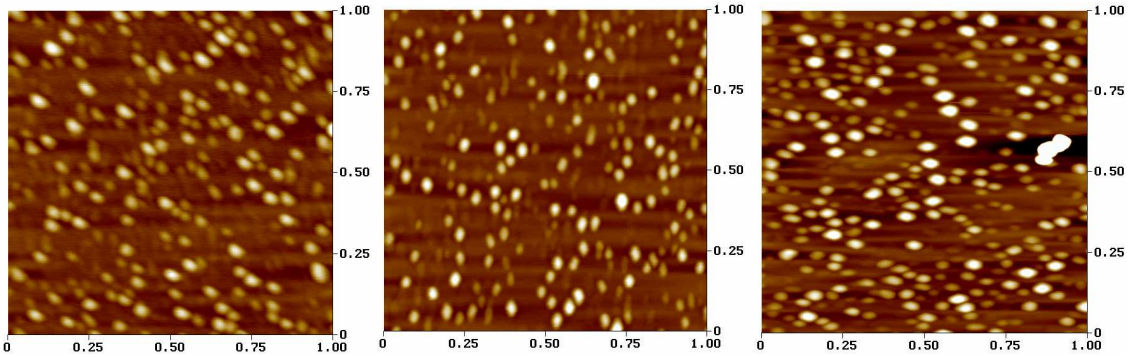

Figure 9.10. AFM images of the InAs quantum dots on InAlAs with different growth rates (left) TMIn 120 sccm and 2.7 s; (center) TMIn 90 sccm and 3.6 s; (right) TMIn 45 sccm and 7.2s.

In summary, we investigated the effect of the growth rate, the amount of the QD material and the matrix material on the formation of the quantum dots. With these optimized conditions, the devices were grown and tested.

9.2.2 InAs/InGaAs/InAlAs/InP QDWIP structure

Self-assembled semiconductor quantum dots (QDs) [88] have attracted much attention because of their interesting properties and possible applications such as quantum dot infrared photodetectors (QDIPs) [44,68,67,89]. QDIPs can be building blocks of focal plane arrays (FPAs) in infrared imaging systems which have been widely investigated for mid-infrared (3~5 μm) and long-infrared (8~12 μm) applications[90,91,92]. QDIPs have been subject to intensive research because they are expected to outperform current quantum well infrared photodetectors (QWIPs)[93,94], due to their i) intrinsic sensitivity to normal incidence light, ii) longer life time of the photo-excited electrons due to the reduced recombination rate associated with a multi-phonon

relaxation step, and iii) lower dark and noise currents[17]. In particular, the lower dark currents enable higher operating temperatures. However, most of the QDIPs reported so far in the literature have been working at temperatures in the range 77K~200 K[44,67,89]. Here, we present a high-performance, room temperature operating mid-infrared photodetector based on InAs QDs embedded in $Ga_{0.47}In_{0.53}As$ QWs grown on top of $Al_{0.48}In_{0.52}As$ barriers on an InP substrate.

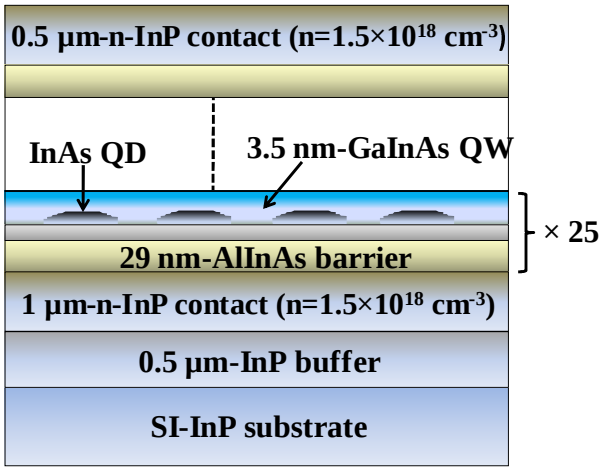

Figure 9.11. Schematic illustration of the device structure grown with low-pressure metalorganic chemical vapor deposition.

The device structure was grown by low-pressure metalorganic chemical vapor deposition (Figure 9.11). Trimethylindium, triethylgallium and trimethyaluminuim were used as group III precursors while pure phosphine, pure arsine and 5% dilute arsine were used as group V precursors. The growth temperature of the whole device structure was 590 °C. First, a 0.5 µm-thick undoped InP buffer layer followed by a 1.0 µm-thick bottom InP contact layer n-type doped to $n=1.5\times10^{18}cm^{-3}$ was grown. Then the active region was grown, consisting of 25 stacks of InAs QD/InGaAs QW layers with 29 nm InAlAs barrier layers. The 3.5 nm-InGaAs QW layer on top of each QD layer had a doping level of $n=1\times10^{18}cm^{-3}$. Finally, we grew a 0.5 µm-thick

top InP contact layer doped to $n=1.5\times10^{18}cm^{-3}$. The InAs QDs on the InAlAs barrier layers were obtained by self-assembly based on the Stranski-Krastanow epitaxial growth mode. The nominal QD growth rate was 0.5 monolayer per second (ML/s) and the growth time was 3.6 seconds with 70 sccm of TMIn flow rate.

An array of 400×400 μm^2 detector mesas was fabricated using conventional photolithography, dry etching with electron cyclotron resonance reactive ion etching, and lift-off techniques in order to test the characteristics of the devices. Ti/Pt/Au bottom and top metal contacts were made via e-beam metallization, lift-off, and alloying at 400ºC for 2 minutes. The sample was then mounted to a copper heatsink and attached to the cold finger of a liquid nitrogen cryostat equipped with a temperature controller.

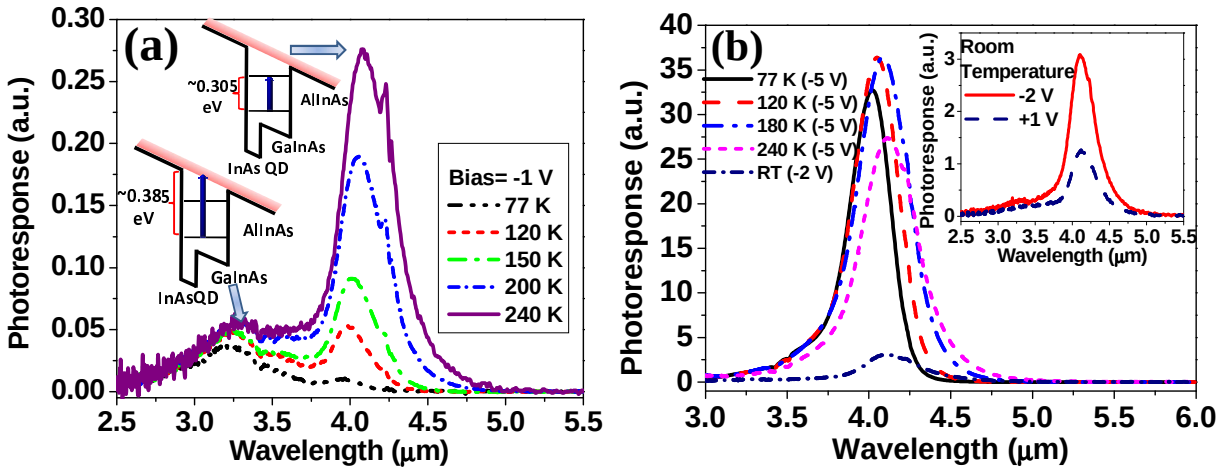

Figure 9.12. (a) Photoresponses at different temperatures for -1 V bias; (b) photoresponses at different temperatures for -5 V applied bias and -2 V for room temperature (RT). The inset shows the photoresponses measured at RT for various biases.

We observed the spectral response at several temperatures and applied biases by using a Fourier transform infrared spectrometer in the normal incidence configuration without any

optical coupling structures (Figure 9.12). In this device structure, both the InAs QD layers and InGaAs QW layers are involved in the infrared absorption process. The coupling of QDs and QWs has been used in other QDIP device structures, such as dot-in-a-well (DWELL)[67,95] where the intersubband transition occurs between the hybrid states of the quantum dot and the quantum well. In our device structure, we believe the initial state is not necessarily from a localized "pure" quantum dot state but from a delocalized "mixed" state of the quantum well and the quantum dot as shown in the inset of Figure 9.12(a). At an applied bias of -1 V, there are two peaks, around 3.2 μm and 4.1 μm as shown in Figure 9.12(a).

The intensity of the peak around 3.2 μm does not increase significantly as the temperature increases. The peak around 3.2 μm comes from a bound-to-continuum transition where the electrons are photo-excited from the ground state to a continuum state as depicted in the inset of Figure 9.12(a). That is the reason why the increase of the temperature does not improve the photoresponse around 3.2 μm. On the other hand, the photoresponse around 4.1 μm increases significantly with the temperature because it comes from a bound-to-bound transition in the InAs QD/GaInAs QW hybrid states and thus the temperature can help the photo-excited electrons escape to the continuum as depicted in the inset of Figure 9.12(a). For all temperatures except room temperature, at an applied bias of -5 V (-2 V for room temperature), the peak around 4.1 μm was dominant in the spectral response, as shown in Figure 9.12(b). The strong sensitivity to the applied bias is another indicator that the transition of the photo-excited electrons takes place between bound states of the QD/QW hybrid.

The peak responsivity (R_p), which is a measure of the photocurrent response per unit optical power, was measured as a function of bias and temperature as shown in Figure 9.13(a).

The responsivity increased with temperature from 120 K to 200 K and started decreasing above 200 K. The peak responsivity was measured to be 822 mA/W at 150 K and -5 V. In QDIPs or QWIPs, the photocurrent can increase or decrease with the temperature depending on whether the relaxation to the lower state or the escape to the continuum state is favorable.

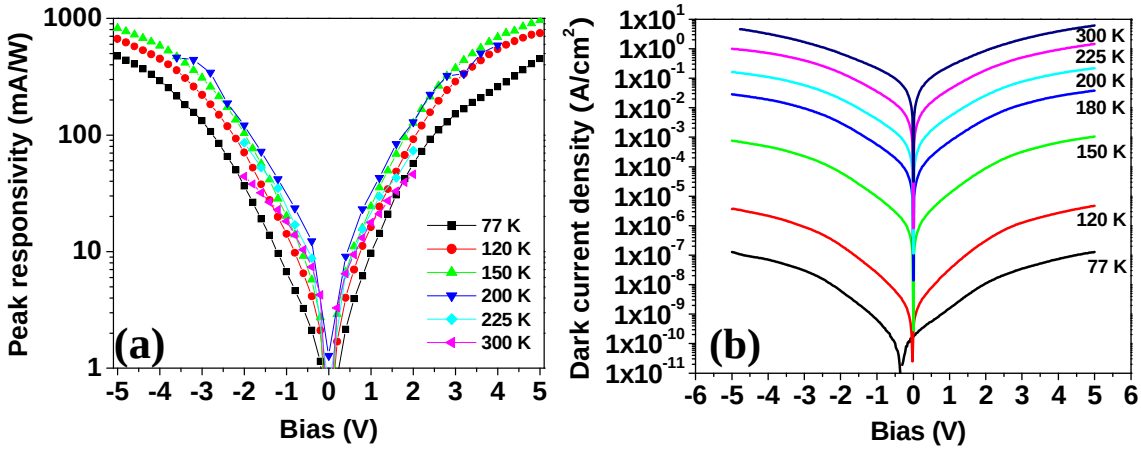

Figure 9.13. (a) Peak responsivity at different temperatures as a function of applied bias; (b) Dark current density at different temperatures as a function of applied bias.

Above a certain temperature, the adverse thermal increase of the relaxation of the photo-excited electrons back to the lower state dominates any improvement in escape[57]. In our system, that turnover is believed to take place at around 200 K, above which the responsivity starts decreasing with increasing temperature.

The dark current density of this device was measured as functions of bias and temperature (Figure 9.13(b)). A remarkably low dark current density was obtained in this device. At 200 K and -5 V, the dark current density was measured to be 163 mA/cm^2. High dark current usually limits the capability for high temperature operation in photoconductors. Therefore, it is crucial to achieve a low dark current with a reasonable photocurrent at high temperature. In QDIPs, low

dark currents can be engineered by introducing a current blocking layer[96]. But this current blocking layer will also decrease the photocurrent because the dark current and photocurrent follow the same transport path. In our device, the QD layers decrease the dark current without significantly compromising the photocurrent. We think the InAs QD layers act as mobility traps for the dark carriers, but do not seriously affect the escape of the photo-excited carriers.

The specific detectivity (D*), which is calculated by $R_pA^{1/2}/S^{1/2}$, was obtained from the measured peak responsivity, the illuminated area of the detector (A), and noise density spectra (S) (Figure 9.14). The noise spectra were measured with a fast Fourier transform signal analyzer and a low noise pre-amplifier. The maximum D* of 2.8×10^{11} $cmHz^{1/2}/W$ was measured at 120 K. The room temperature detectivity was 6×10^{7} $cmHz^{1/2}/W$.

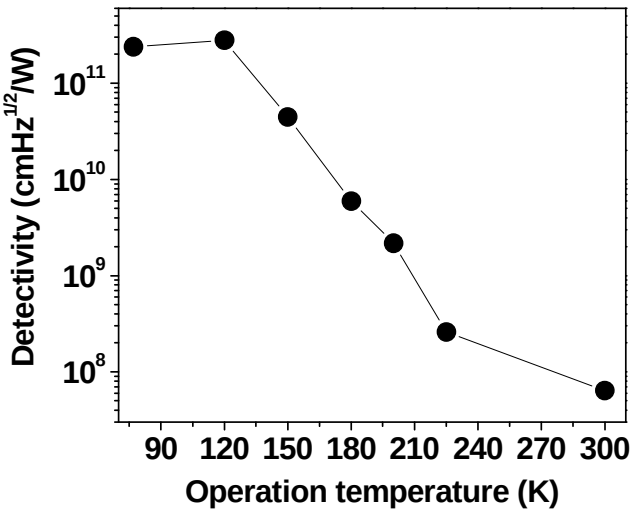

Figure 9.14. Maximum detectivity at different temperatures.

Another important device parameter is the quantum efficiency (η), which can be obtained from the relation $\eta=R_p h\nu/qg$ where hν is the incoming photon energy, q is the charge of the carrier, and g is the photoconductive gain. As a good approximation, the noise gain can be used

instead of the photoconductive gain[50]. The noise gain was extracted from the noise (i_n) and dark current (I_d) using the expression $g=i_n^2/4eI_d$. A very high quantum efficiency of 35 % was obtained in this device for normal incidence. This high quantum efficiency might be due to the high oscillator strength for the normal incident light and a higher number of carriers available for the absorption compared to conventional QDIPs where the number of photoactive carriers is limited by the number of QDs.

In conclusion, we demonstrated a high-performance InAs quantum-dot/quantum-well mid-infrared photodetector grown on InP substrate, which operates up to room temperature. The peak detection wavelength was observed at 4.1 μm. The peak responsivity and the specific detectivity at 120 K were 667 mA/W and 2.8×10^{11} cmHz$^{1/2}$/W respectively. Low dark current density and a high quantum efficiency of 35 % were obtained in this device.

9.2.3 Demonstration of high temperature operating QDWIP Focal Plane Array (FPA)

Having the InAs/InGaAs/InAlAs/InP QDWIP structure discussed so far, it was natural for us to develop an infrared imaging system with FPA. The first demonstration of the QDWIP FPA was mainly done by my colleague (S. Tsao)[97]. A 320 × 256 focal plane array had 30 μm pitch and 25 μm × 25 μm mesa detectors. A detailed fabrication steps and analysis can be found in Ref. 97. The focal plane array had a peak detection wavelength of 4 μm, a responsivity of 34 mA/W, a conversion efficiency of 1.1 %, and a noise equivalent temperature difference of 344 mK at an operating temperature of 120 K.

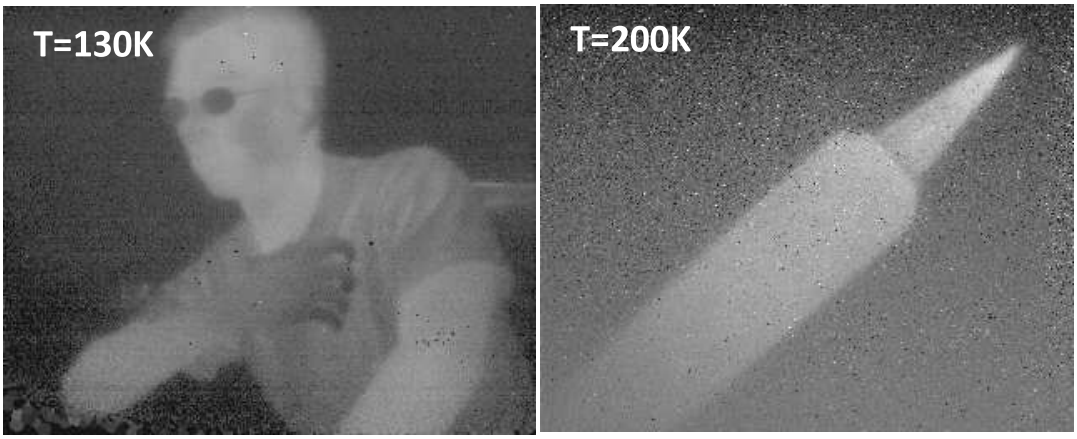

Figure 9.15. Focal plane array imaging taken at 130K and 200K, which was also the maximum operating temperature of the array.

The device's low dark current density and the persistence of the photocurrent up to room temperature enabled the high temperature imaging as shown in Figure 9.15. Especially 200 K was the highest operation temperature reported so far in QDIP- and QWIP- based FPAs.

9.2.4 Improvement of InAs/InGaAs/InAlAs/InP QDWIP device performance via quantum dot engineering

After high performance InAs/InGaAs/InAlAs/InP QDWIP was demonstrated for the first time, the efforts to improve the device performance were made through quantum dot engineering. The quantum dot engineering is meant by the process of changing the shape, size and density of the quantum dots with growth conditions. In the section of 9.2.1, the various growth conditions for InAs quantum dots were discussed.

We optimized the InAs quantum dot growth condition by increasing the flow rate of the trimethylindium (TMIn) from 70 sccm to 90 sccm. The size and density of InAs QDs were increased as shown in Figure 9.16. Under both conditions, the QDs have a bimodal size

distribution. With a TMIn flow rate of 70 sccm, most of the quantum dots are the very small kind around 1 nm height. These smaller dots are indicated in Figure 9.16 by the yellow circle. For the 90 sccm-TMIn growth condition the number of large dots, indicated by the red circle, is significantly increased. Those QDs are about 20 nm in diameter and 4 nm in height.

The device grown with the bigger and denser QDs just described had the same structure as our previous best device, namely 25 period-InAs QDs/InGaAs QWs/InAlAs barriers/InP substrate. The barrier, spacer, and QW thicknesses were kept the same, as were the doping levels. Only the QD growth conditions were changed as described above. The InGaAs QWs are 3.5 nm thick with $1\times10^{18}cm^{-3}$ doping. The InP contact layers have a doping level of 1.5×10^{18} cm^{-3}. The schematic diagram of the device structure was same as the one described in Figure 9.11.

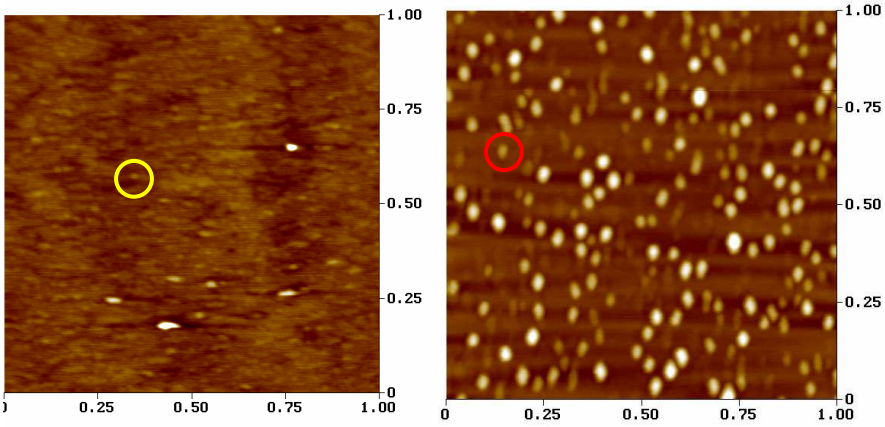

Figure 9.16. AFM images of the InAs quantum dots on InAlAs with different growth rates (left) TMIn 70 sccm and 3.6 s; (right) TMIn 90 sccm and 3.6 s.

After the test mesas were fabricated, the temperature dependent device performance of this device structure with the new QD growth conditions was measured. The photoresponse was very similar to that of the previous best result and with a peak detection wavelength at 4μm as shown in Figure 9.17.

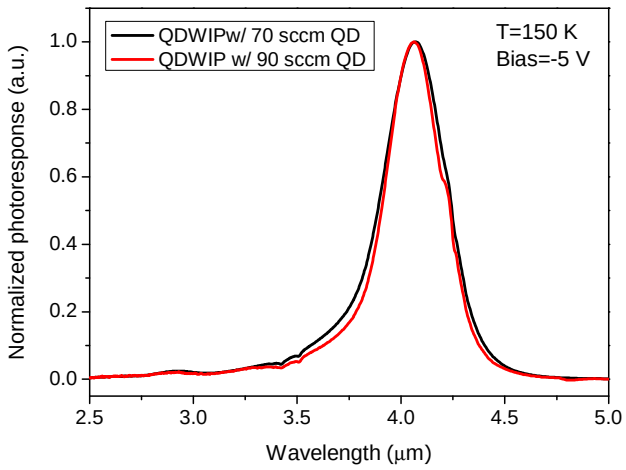

Figure 9.17. Comparison of the normalized photoresponses at 150 K and -5 V from QDWIPs with 70 sccm and 90 sccm InAs QDs.

The reason that the peak detection wavelength did not change was that the ground state of the hybridized state might be so slightly changed that the energy separation between the hybridized ground state and quantum well excited state did not change significantly.

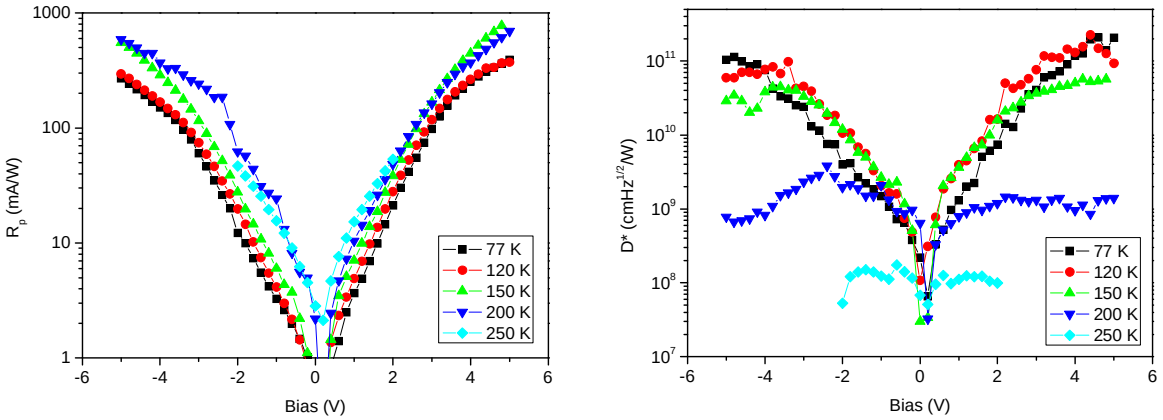

Figure 9.18. Performance of a QDWIP device with 90 sccm InAs QDs. (Left) peak responsivity at different temperatures as a function of applied bias; (right) peak detectivity at different temperatures as a function of applied bias.

The device performances were measured at different temperatures as a function of applied bias. At 150 K, the specific detectivity was 5.7×10^{10} cmHz$^{1/2}$/W and the quantum efficiency was 48 %. The specific detectivity was 3.8×10^{9} cmHz$^{1/2}$/W at 200 K. Even though the peak responsivity did not change very much compared with that of QDWIP with 70 sccm InAs QDs, the quantum efficiency was improved from 35 % to 48 %. The bigger and denser InAs QDs caused basically two changes in the device operation. One is the change of the electronic structure of QD-QW system. The strength of the hybridization might be stronger in the case of the bigger and denser QDs buried in QW. The stronger hybridization is possible to induce stronger oscillator strength. The other change occurs in the transport of the photoexcited electrons. The stronger hybridization might shift the ground and excited state slightly down so that the photoexcited electrons should overcome the higher tunneling barrier at any applied bias.

The stronger oscillator strength and higher tunneling barrier might result in the higher quantum efficiency and lower photoconductive gain respectively. Therefore similar peak responsivity was observed from two devices because the higher quantum efficiency and lower gain are compensated.

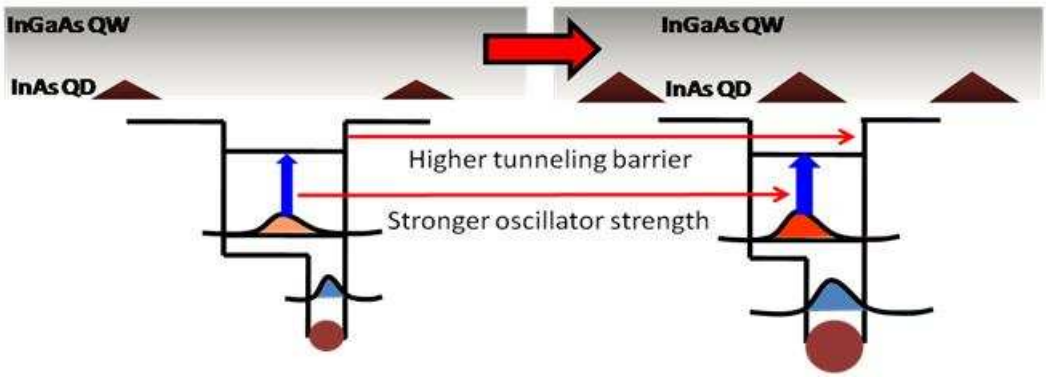

Figure 9.19. Schematic diagram show how the quantum efficiency and the height of the tunneling barrier increase with bigger and denser InAs QDs buried in InGaAs QW.

In conclusion, we investigated adjusting the quantum dot growth conditions in the device. The new quantum dot growth condition improved the infrared absorption leading to the increase of the detectivity and quantum efficiency. We think the larger and denser InAs quantum dots could increase the interaction with the InGaAs quantum well through stronger hybridization. The stronger mixture of QD and QD states may result in stronger oscillator strength for normal incident light. This situation is not applicable to a pure quantum dot system, where smaller quantum dots are desired for higher oscillator strengths.

9.2.5 Comparison between QWIP and QDWIP

In order to better understand the device operation of QDWIP, the device performance of QWIP and QDWIP will be compared in this section. First, the photoresponses of QWIP and QDWIP were compared at the various conditions.

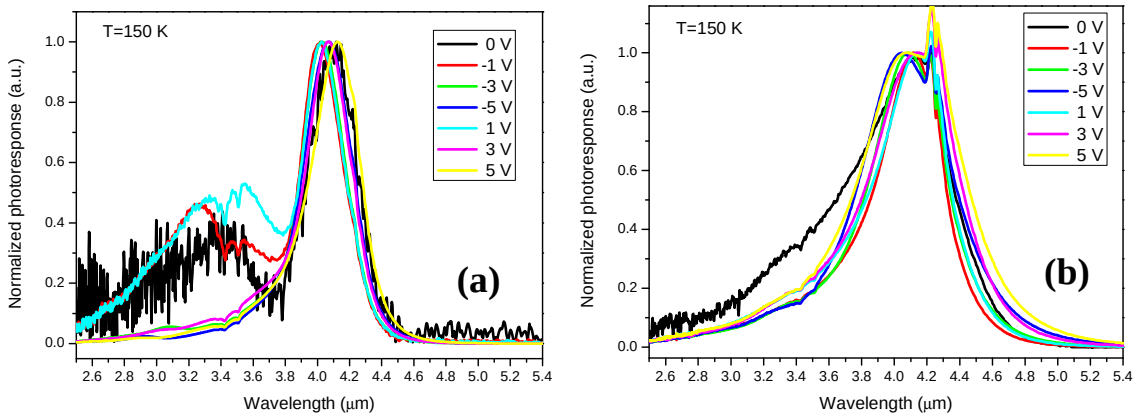

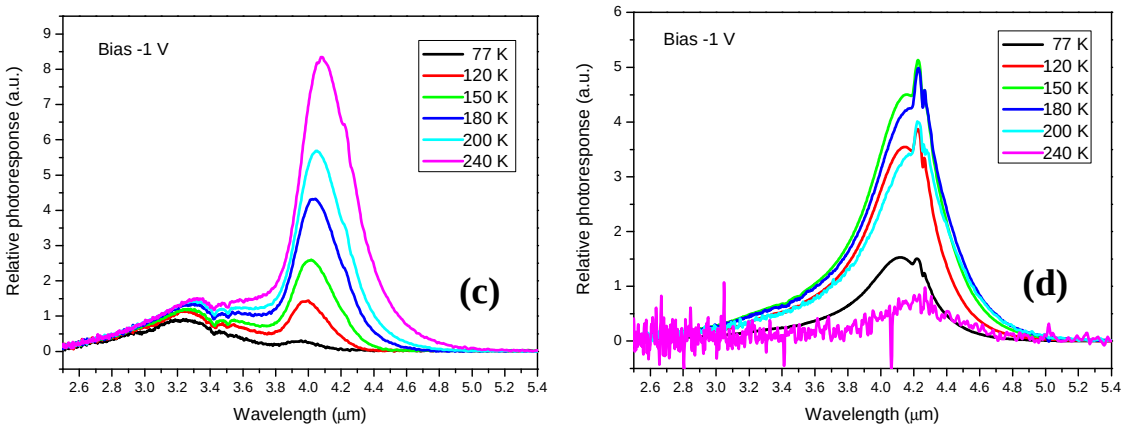

Figure 9.20. Comparison of the photoresponses from QDWIP and QDIP at various temperature and applied bias. (a) The bias-dependent photoresponses at 150 K from QDWIP (b) The bias-dependent photoresponses at 150 K from QWIP (c) The temperature-dependent photoresponses at -1 V from QDWIP (d) The temperature-dependent photoresponses at -1 V from QWIP.

The photoresponses from QDWIP and QWIP were very different at low bias and/or high temperature while they were similar at high bias and/or high temperature. This difference in the photoresponses came from the difference in the energy levels and the escape of the photoexcited electrons. The energy levels of InGaAs QW/InAlAs barrier were calculated using single-band effective mass approximation with with $m_w=0.041m_e$, $m_b=0.075m_e$, and V=473 meV. The intersubband transitions in InGaAs QW were supposed to be bound-to-quasibound transition and bound-to-continuum transition as described in Figure 9.19.

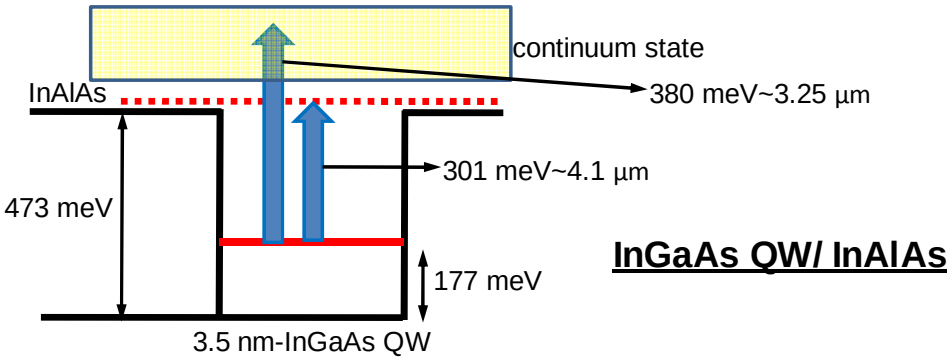

Figure 9.21. Schematic diagram of calculated energy levels and possible intersubband transitions of InGaAs QW/InAlAs barrier.

Compared to the photoresponse of the QWIP, the QDWIP had the photoresponses which were more sensitive to the bias and temperature. In case of QWIP, the photoexcited electrons are easily escaped from QWs and transport through the device. In the QDWIP, the bias and temperature sensitive photoresponse could be explained with the different escape path of the photoexcited electrons.

Another difference between QWIP and QDWIP was the activation energy extracted from the dark current as shown in Figure 9.27. We assumed that above high temperature such as 100 K, the dark current of the devices was generated by the thermionic emission from QW and QD/QW system. The activation energy of QDWIP was higher than that of QWIP by around 100 meV. This indicated that the Fermi level of QDWIP was much lower than that of QWIP by around 100 meV.

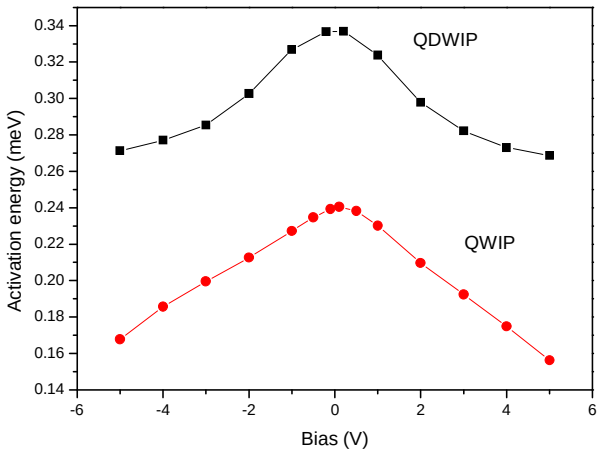

Figure 9.22. Comparison of the activation energy between QWIP and QDWIP, which were extracted the temperature dependent dark currents as a function of bias.

From the differences in the experimental data such as the photoresponses and activation energy, the QDWIP photocurrent is therefore mainly due to escape from a bound state even if the original excitation may have been to a quasi bound level as in the QWIP. In the previous section, it was said that the electronic state of QD/QW system was a hybrid state of QD and QW. Since the energy level calculation of QD/QW system requires full 3-dimensional consideration, the 2-dimensional approximation was made in order to model QD/QW system.

In order to model the QD/QW system, 2 nm-InAs layer was added to InGaAs QW layer. We assumed that the 2-dimensional InAs layer would play a similar role as 3-dimensional InAs QD would in reality. In the calculation, the effective mass of InAs layer was used as 0.05 m_e and its potential was deeper by 80 meV than InGaAs QW's potential. The result of the calculation showed that the overall shift-down of energy levels and the quasibound state became deeply bound state in Figure 9.28. But the problem of this model is that actually in the active region, we

can divide the active region into two regions such as QD and hybrid regions as shown in Figure 9.28. We can speculate a following model.

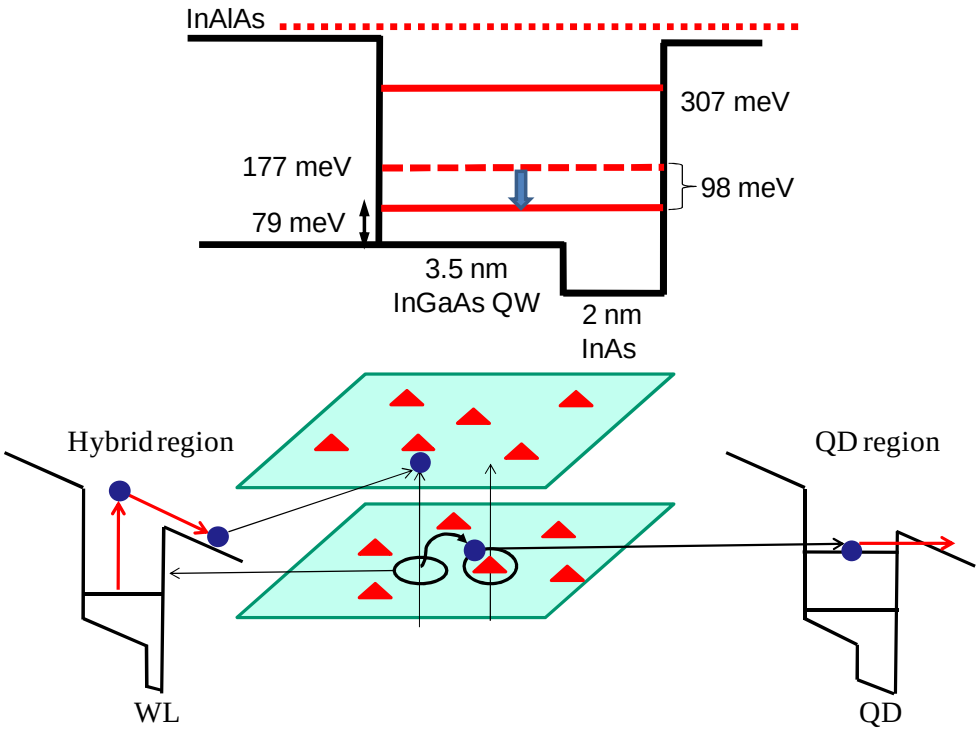

Figure 9.23. (Top) Schematic diagram of calculated energy levels of InAs/InGaAs QW/InAlAs barrier. The dotted line indicates the ground state of the InGaAs QW/InAlAs barrier. (Bottom) Two regions in the active region of the QDWIP: Intermediate (QW) region and the QD regions.

The photoexcited electrons are generated in the hybrid region which is not pure quantum well state but still hybrid state of QD/QW. And then the photoexcited electrons fall into the QD region which has a deeply bound state and stay there until they escape and become the photocurrent. Since the generated photoexcited electrons are bound, the higher bias is required to have similar photocurrent than in case of QWIP.

Another which should be noticed was that the ground state of the QD/QW system was lowered from 177 meV to 79 meV by almost 100 meV. If the Fermi level of the QD/QW system were determined mostly by the position of the ground state, then this could explain the higher activation energy in QDWIP device. Even though this 2-dimensional approximation was not

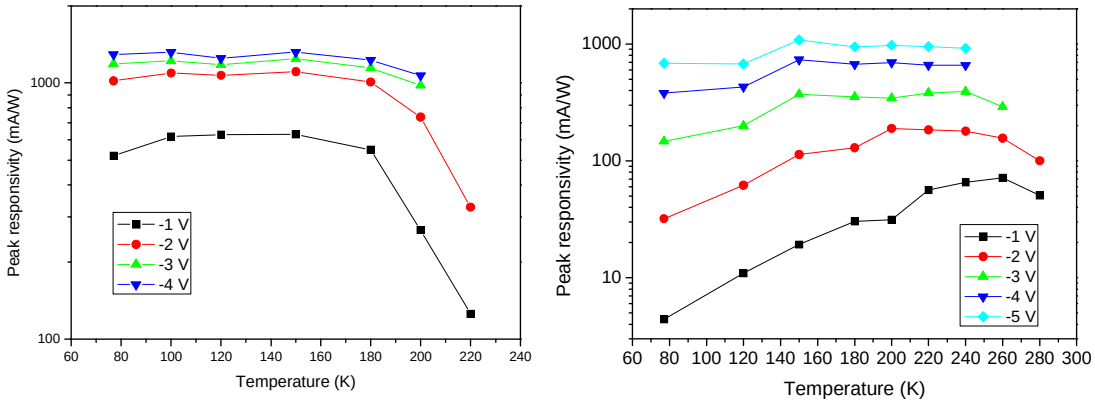

Figure 9.24. Peak responsivity as a function of temperature from QWIP (left) and QDWIP (right).

accurate to model the QD/QW system, it proved the idea that the InAs QD layer could shift the entire energy level down.

The benefit of the quantum dot in the device is the high temperature operation. The peak responsivities from QDWIP and QWIP were compared as a function of the applied bias in Figure 9.24. The temperature dependent responsivity of QDWIP had a tendency of increase as a function of temperature up to 260 K at -1 V and around 220 K at other biases while the responsivity of QWIP increased from 77 K to 180 K and decreased from 180 K to higher temperature. The reason is because the relaxation time of QDWIP did not change up to above 200 K and those of QWIP started to change from 180 K. This proved the QDWIP has a long lived bound state for the photoexcited electrons.

In conclusion, by inserting the InAs QDs in the InGaAs/InAlAs QWIP structure, we were able to achieve the higher temperature operation and higher bias operation due to the hybridization of quantum dot and quantum well state. The new hybrid states were shifted down and the final state became the deeply bound state. The deeply bound state had a longer life time than that of QWIP and thus the QDWIP had better temperature performance.

9.2.6 Lowering the operating bias for infrared imaging application

The motivation to lowering the operating bias is solely to optimize the infrared imaging with FPA. A FPA is usually integrated with a ROIC (readout integrated circuit) which is used to multiplex or read out the signals from the detector elements. Each ROIC has a different biasing capability. In our case, the Indigo ISC9705 ROIC was hybridized to our QDWIP FPA. The problem came from a high optimum operating bias (±5 V) of our device which exceeds the bias capability of the ROIC in use (-3 V). The modification of the ROIC requires the work which cannot be done in our current research. Another drawback of high operating bias in FPAs is high power consumption. High power consumption is not desired in the space application. Different QDWIP structures were tested with the aim of decreasing the operating bias.

First we will discuss the theoretical background of decreasing the operating bias while minimizing any performance reductions. Then, the device structures and their performance will be discussed.

The operating bias is related to the transport of the carriers (electrons) inside the device structures. The carriers include the dark carriers and photo carriers which generate the dark- and photo-currents respectively. In any case, the bias dependent current depends on the tunneling

probability of the electron from the quantum confined states. The photocurrent is proportional to the tunneling probability D(V, E_1+hω) where V is the voltage drop per period. For example, if 5 V is applied to a 50 period-device, V will be 0.1.

In the WKB approximation, D(V, E_1+hω) is equal to

$$D(V, E_1 + \hbar\omega) = \exp\left(\frac{-4B}{3e\hbar V}\right)(2m_b)^{1/2} \left[(H - E_1 - \hbar\omega)^{3/2} - (H - eV - E_1 - \hbar\omega)^{3/2}\right] \quad \text{Eq (9.1)}$$

where B is the barrier thickness, m_b is the effective mass of the barrier, H is the barrier height and $E_1 + \hbar\omega$ is the energy of the photoexcited electron. If we plot this equation as a function of V, the tunneling probability strongly depends on V as shown in Figure 9.25.

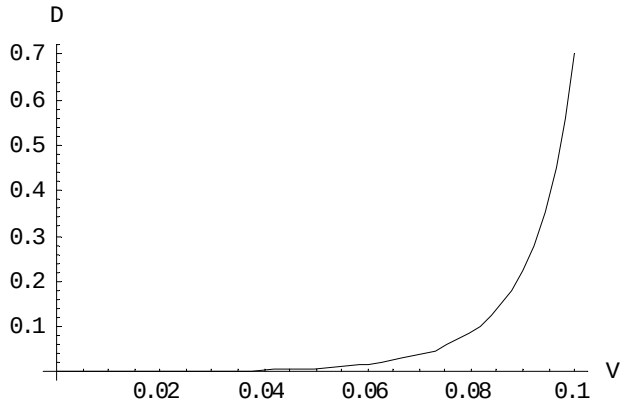

Figure 9.25. Tunneling probability as a function of the voltage drop per period.

By increasing the voltage drop per period or decreasing the barrier thickness, we can increase the tunneling probability and thus the photocurrent. Another way to increase the voltage drop is to reduce the thickness of the active region by decreasing the number of periods.

We grew two device structures, one with a fewer periods and another with thinner barriers (17.2 nm). The device structures are shown in Figure 9.26.

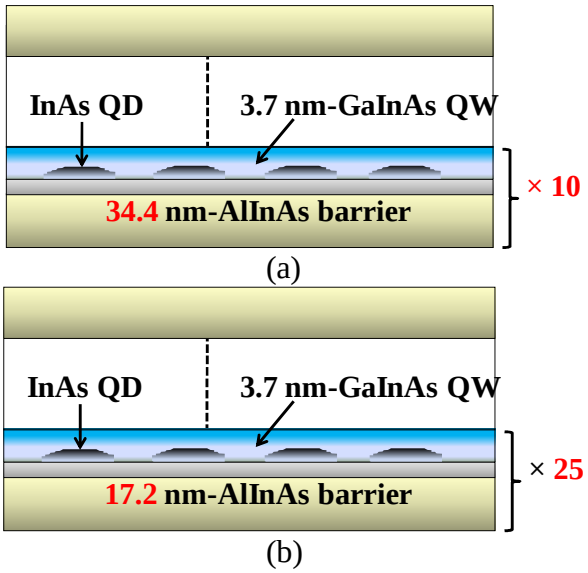

Figure 9.26. Device structures to reduce operating bias. (a) 10 period QDWIP structure with thick barriers; (b) 25 period-QDWIP with thinner barriers.

First, we grew the device structure with a 10 period-QD/QW active region. The other device structural parameters such as the quantum dots, contact layers and barrier layers were kept the same as in the previous best device except the thickness of the quantum well layer (3.7 nm). Second, we decreased the thickness of the InAlAs barrier almost by half and kept the same number of QD/QW periods (25).

Due to the slightly thicker quantum well layers in the active regions, the peak detection wavelength from both devices shifted to 4.2 μm from 4.1 μm of the previous devices. The peak responsivity showed higher values at smaller bias from the device with 10 periods as shown in Figure 9.27.

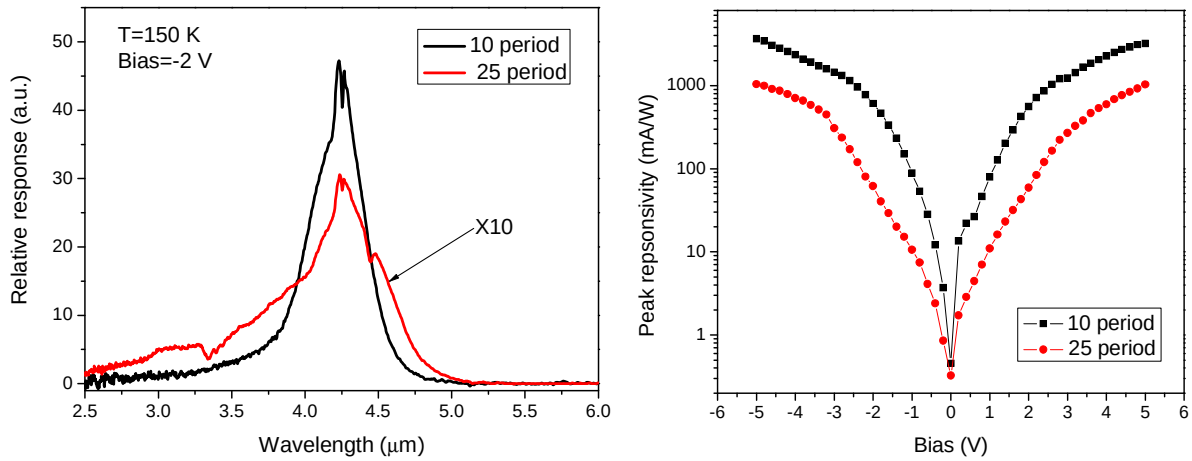

Figure 9.27. (Left) relative photoresponses and (right) peak responsivity of the QDWIP devices with 10 periods of thick barrier and 25 periods of thin barrier at 150 K.

At -2 V, the peak responsivity was 606 mA/W compared to 30 mA/W at the same bias from the previous best device. In terms of the voltage drop per period, -2 V in a 10-period device corresponded to -5 V in 25-period device. Actually the peak responsivity of 10-period current device at -2 V and 25-period best device at -5 V are similar.

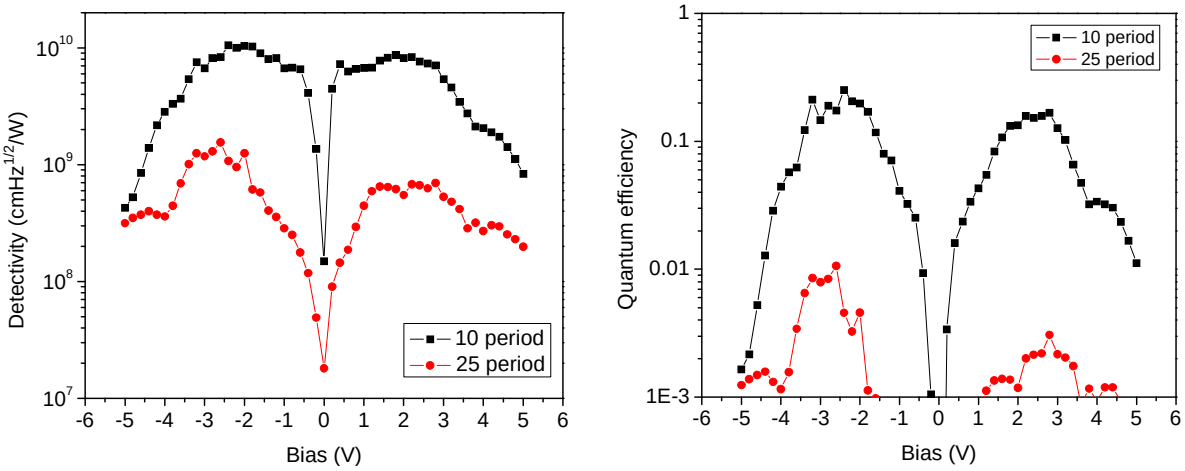

Figure 9.28. (Left) detectivity and (right) quantum efficiency of the QDWIP devices with 10 periods of thick barrier and 25 periods of thin barrier at 150 K.

For the 10-period device, the detectivity was calculated to be 1×10^{10} cmHz$^{1/2}$/W and the quantum efficiency was 25 % at -2.4 V. For the 25-period device with thin barriers, the performance was not good because the thinner barriers are more vulnerable to the noise generated from the device.

We conclude that using thinner barriers is not a good approach to reduce the operation bias because it compromised the device performance significantly. On the other hand, optimization of the number of layers seems promising as an approach to reduce the operating bias. The performance was as good as the previous best, but we can still improve it by optimizing other device structure parameters.

10 Conclusions and Future work

The objective of this work was the combination of the experiments, modeling and their analyses of the QDIP devices in order to achieve the high performance and high operating temperature for infrared imaging application.

As of the theoretical modeling part, the energy levels and oscillator strengths have been calculated via single band effective mass envelope function method. Responsivity and dark current also have been modeled by detailed balance equation considering the energy levels of the quantum dots. Especially it was found that the decrease of the responsivity as a function of temperature was related to the increase of the relaxation rate of the photoexcited carriers. A theory of diffusion and recombination which was an attempt to explain the high values of gain in QDIPs was developed. The analysis was carried out on one of the QDIPs based on the developed theoretical modeling.

As of the experimental part, In(Ga)As quantum dots with different matrix materials were grown and optimized by MOCVD with various conditions. The focus has been made on the development of InAs/InP based MWIR-QDIP. We optimized the growth conditions of the InAs QDs such as the growth rate, V/III ratio and ripening time with fixed QD growth temperature (440 °C). The matrixes we studied were 1 nm-GaAs, 1 nm-GaAs/3 nm-InAlAs and GaP on InP buffer layers. We investigated two kinds of MWIR-InP based QDIP structures based on InAs QDs grown on InP substrates. Those QDIP structures based on the lnAs QDs grown at low temperature had a peak detection wavelength around 4~5 μm and a detectivity around ~2×10^{9} $cmHz^{1/2}/W$ at 77 K.

In order to overcome the difficulties related to controlling the detection wavelength and poor performance due to low material quality, the new device structures utilizing the quantum well and quantum dot have been developed. The device structure which we named as quantum dot quantum well infrared photodetector (QDWIP) had 25-period InAs QD layers which were grown on lattice-matched InAlAs barrier and covered with lattice-matched InGaAs quantum well on InP substrate. The peak detection wavelength was observed at 4.1 μm. The peak responsivity and the specific detectivity at 120 K were 667 mA/W and 2.8×10^{11} $cmHz^{1/2}/W$ respectively. A high quantum efficiency of 35 % was obtained in this device. Due to low dark current density, a detectivity of 6×10^{7} $cmHz^{1/2}/W$ could be obtained even at room temperature. Based on the developed QDWIP, we demonstrated a 320 × 256 focal plane array which could operate up to 200 K.

By increasing the size and density of InAs QDs in InAs/InAlAs/InGaAs/InP QDWIP, the quantum efficiency was improved from 35 % to 48 %. We think the larger and denser InAs quantum dots could increase the interaction with the InGaAs quantum well through stronger hybridization. The stronger mixture of QD and QD states may result in stronger oscillator strength for normal incident light. We also demonstrated QDWIP device working at lower bias in order to be optimized in FPA application.

Our ultimate goal in the research on the quantum dot based infrared photodetector is the realization of room temperature operation maintaining high performance such as high quantum efficiency and detectivity. In order to achieve the goal, we should focus on the improvement of the interface between the quantum dot and an adjacent capping layer which can be a quantum well layer or a barrier layer. In the system where quantum dots are coupled with quantum wells,

a slightly different approach should be made. Defect issues associated with multiple stacking should be addressed and solved. With developed methods to improve the defects, a large number of stacks might be possible without degrading the device performance. It naturally translates into higher QE, D* and operating temperature.

11 References

[1] Y. Arakawa, H. Sakaki, *Appl. Phys. Lett.* **40**, 939 (1982)

[2] D. Leonard, M. Krishnamurthy, C. M. Reaves, S. P. Denbaars, P. M. Petroff, *Appl. Phys. Lett.* **63**, 3203 (1993)

[3] R. D. Hudson, *Infrared System Engineering*, John Wiley and Sons, New York, (1969).

[4] M. Schlessinger, *Infrared Technology Fundamentals* Marcel Dekker, Inc., New York, (1995).

[5] D. Chandra, IEEE T Aero Elec Sys **34**, 1009 (1998).

[6] M. Whiteley, Roggemann M., Johnson R Opt. Eng. **35**, 3531(1996).

[7] E. Wormser Appl. Opt. **7**, 23 (1968).

[8] F. Quin, P. Steele, R. Shumulsky, Forest Prod. J. **48**, 80 (1998).

[9] J. Debruijn , "Near-infrared spectroscopy in the beet sugar-industry," Int. Sugar J. **97**, pp. 147-152 (1995).

[10] M. Meurens, J. Walleon, and J. Tong, Vib Spectrosc **10**, 341 (1996).

[11] P. Biagioni, R. Longmore, and J. McGimpsey, Dentomaxillofac Rad **25**, 119 (1996).

[12] F. Chan, A. So, and A. Kung, Bio-med Mater Eng **5**, 169 (1995).

[13] G. Nollert, T. Shinoka, and R. Jonas, Thorac Cardiov. Surg. **46**, 167 (1998).

[14] A. Samann, U. Muller, and C. Fischbacher, Diabetologia **41**, A45 (1998).

[15] L. Esaki, R. Tsu, Superlattice and negative conductivity in semiconductors, IBM Journal of Research and Development, **14**, 61 (1970).

[16] H. Mosheni, E. Michel, J. Sandven, M. Razeghi, W. Mitchel and G. Brown, Appl. Phys. Lett. 71, 1403 (1997)

[17] V. Ryzhii, Semicond. Sci. Technol. 11, 759 (1996)

[18] V. Ryzhii, I. Khmyrova, V. Mitin and M. Stroscio, and M. Willander, Appl. Phys. Lett. 78, 3522 (2001).

[19] N. W. Ashcroft and N. D. Mermin, *Solid State Physics*, Saunders College Publishing, U.S.A., 1976

[20] U. Bockelmann and G. Bastard, Phys. Rev. B **42** 8947 (1990).

[21] H. Bestiny, C. M. Sottomayor-Torres, and C. Weisbuch, Phys. Rev. B **44**, 10945 (1991).

[22] J. Urayama, T. B. Norris, J. Singh, P. Bhattacharya, Phys. Rev. Lett. **86**, 4930 (2001).

[23] D. Bimberg, M. Grundmann, N. N. Ledentsov, S. S. Ruvimov, P. Werner, U. Richter, J. Heydenreich, V. M. Ustinov, P. S. Kop'ev, P. S., Thin Solid Films (1995), 267(1-2), 32-6.

[24] J. D. Vincent, Fundamentals of Infrared Detector Operation and Testing, Wiley & sons, New York. (1990).

[25] E. O. Kane, J. Phys. Chem. Solids **1**, 249 (1957).

[26] S. L. Chuang, *Physics of Optoelectronic Devices* (Wiley, New York, 1995).

[27] J. M. Luttinger and W. Kohn, Phys. Rev. 97, 869 (1955).

[28] T. B. Bahder, Phys. Rev. B **41**, 11992 (1990).

[29] O. Stier and D. Bimberg, Phys. Rev. B **59**, 5688 (1999).

[30] N.W. Ashcroft, Electron-ion pseudopotential in metals, Physics Letters **23**, 48 (1966)

[31] L.-W. Wang, A. Zunger, Phys. Rev. B **54**, 11417 (1996)

[32] A. Franceschetti and A. Zunger, Phys. Rev. B **62**, 2614 (2000)

[33] D. Gershoni, H Temkin, G.J. Dolan, J. Dunsmuir, S.N.G. Chu, and M.B. Panish, Appl. Phys. Lett. **53**, 995 (1998)

[34] S. Gangopadhyay and B.R. Nag, Nanotechnology **8**, 14 (1997)

[35] M. Califano and P. Harrison, Phys. Rev. B **61**, 10959 (2000)

[36] E. P. Pokatilov, V. A. Fonoberov, V. M. Fomin, J. T. Devreese, Phys. Rev. B **64**, 245328 (2001).

[37] J. Williamson, L. Wang, A. Zunger, Phys. Rev. B **62**, 12963 (2000).

[38] B. F. Levine, A. Zusman, S. D. Gunapala, M. T. Asom, J. M. Kuo, W. S. Hobson, J. Appl. Phys.72, 4429 (1992).

[39] Ryzhii, V. Jpn. J. Appl. Phys. **40**, L148 (2001).

[40] V. Ryzhii, I. Khmyrova, V. Mitrin, Semicon. Sci. Technol. **19**, 8 (2004).

[41]A. D. Stiff-Roberts, X. H. Su, S. Chakrabarti, P. Bhattacharya, IEEE Photon. Technol. Lett. **16**, 867 (2004).

[42] A. Yelon, B. Movaghar, Phys. Rev. Lett. **65**, 618 (1990).

[43] B. R. Trenhaile, V. N. Antonov, G. J. Xu, S. Koji, S. Nakayama and J. H. Weaver (2004) in press

[44] J. Jiang, S. Tsao, T. O'Sullivan, W. Zhang, H. Lim, T. Sills, K. Mi, M. Razeghi, G. J. Brown, and M. Z. Tidrow, Appl. Phys. Lett. **84**, 2166 (2004).

[45] Wei Zhang, Ho-Chul Lim, Maho Taguchi, Alain Quivy, and Manijeh Razeghi, Proc. of SPIE **6127**, p 144, (2006).

[46] Dong Pan, Elias Towe, and Steve Kennerly, Appl. Phys. Lett. **75**, 2719 (1999).

[47] A. D. Stiff, S. Krishna, P. Bhattacharya, and S. Kennerly, Appl. Phys. Lett. **79**, 421 (2001).

[48] K. Hirakawa, S.-W. Lee, Ph. Lelong, S. Fujimoto, K. Hirotani, and H. Sakaki, Microelectronic Engineering **63**, 185 (2002).

[49] S. Raghavan, P. Rotella, A. Stintz, B. Fuchs, S. Krishna, C. Morarh, D. A. Cardimona, and S. W. Kennerly, Appl. Phys. Lett. **81**, 1369 (2002).

[50] Zhengmao Ye, J. C. Campbell, Z. Chen, Eui-Tae Kim, and A. Madhukar, Appl. Phys. Lett. 83, 1234 (2003).

[51] Chuang-Chi Liao, Shiang-Feng Tang, Tzu-Chiang Chen, Cheng-Der Chiang, San-Te Yang, and Wen-Kuan Su, Proc. of SPIE **6119**, 611905 (2006).

[52] K. K. Ghosh, L. -H. Zhao, and D. L. Huber, Phys. Rev. B **25**, 3851 (1982).

[53] P. Grassberger and I. Proccacia, Phys. Rev. A **26**, 3683 (1982).

[54] A. Sergeev, V. Mitin, and M. Stroscio, Physica B **316-317**, 369 (2002).

[55] K. K. Choi, Appl. Phys. Lett. **65**, 1266 (1994).

[56] B. Kochman, A. Stiff Roberts, J. Phillips, S Chakrabarti, J Sprint , B Bhattcharya and S. Krishna, IEEE J. Quantum Electron. **39**, 459 (2003).

[57] H. Lim, W. Zhang, S. Tsao, T. Sills, J. Szafraniec, K. Mi, B. Movaghar, and M. Razeghi, Phys. Rev. B. **72,** 085332 (2005).

[58] E. Rosencher, B. Vinter, *Optoelectronics*, Cambridge University Press: Cambrigde, 2002

[59] J. Z. Zhang, I. Galbraith, Appl. Phys. Lett., **84** 1934 (2004).

[60] H. C. Liu, R. Dudek, A. Shen, E. Dupont, *International Journal of High Speed Electronics and Systems*, **12**, 803 (2002).

[61] F. Bras, P. Boucaud, S. Sauvage, G. Fishman, Appl. Phys. Lett. **80**, 4620 (2002).

[62] S. Sauvage, P. Boucaud, F. H. Julien, J. –M. Gerard, Appl. Phys. Lett. **71**, 2785 (1997).

[63] Z. Chen, O. Baklenov, E. T. Kim, I. Mukhametzhanov, J. Appl. Phys. **89,** 4558 (2001).

[64] A. W. Adawi, E. Zibik, L. R. Wilson, A. Lemaitre, J. W. Cockburn, M. Hopkinson, and G. Hill, Appl. Phys. Lett. **83**, 602 (2003).

[65] B. Movaghar, J. Leo, J. Appl. Phys. **65**, 5019 (1989).

[66] S. Hameau, Y. Guldner, O. Verzelen, R. Ferreira, Phys. Rev. Lett. **83**, 4152 (1999).

[67] E-T. Kim, A. Madhukar, Z. Ye, J. C. Campbell, Appl. Phys. Lett. **84,** 3277 (2004).

[68] S. Chakrabarti, A. D. Stiff Roberts, P. Bhattacharya, S. Gunapala, S. Bandara, S. B. Rafol, S. W. Kennedy, IEEE Phot. Tech. lett. **16**, 1361 (2004).

[69] L. Jiang, S. S. Li, N.-T. Yeh, J.-I. Chyi, C. E. Ross, and K. S. Jones, Appl. Phys. Lett. **82**, 1986 (2003).

[70] D. Pan, E. Towe, and S. Kennerly, Appl. Phys. Lett. **73**, 1937 (1998).

[71] Z. Chen, E.-T. Kim, and A. Madhukar, Appl. Phys. Lett. **80**, 2490 (2002).

[72] E. Finkman, S. Maimon, V. Immer, G. Bahir, S. E. Schacham, F. Fossard, F. H. Julien, J. Brault and M. Gendry, Phys. Rev. B **63**, 045323 (2001)

[73] H. Hwang, K. Park, S. Yoon, E. Yoon, H. Cheong, and Y. Kim, Proc. of SPIE **4999**, 229 (2003).

[74] M. Erdtmann, A. W. Matlis, C. L. Jelen, M. Razeghi, and G. J. Brown, Proc. SPIE Int. Soc. Opt. Eng. **3948**, 220 (2000).

[75] J. Jiang, K. Mi, R. McClintock, M. Razeghi, C. Jelen, G. Brown, IEEE Phot. Tech. Lett. 15, 1273 (2003).

[76] M. Razeghi, *The MOCVD Challenge* ***Vol 1*** (Adam Hilger, Bristol, 1989).

[77] P. B. Joyce, T. J. Krzyzewski, G. R. Bell, T. S. Jones, S. Malik, D. Childs. and R. Murray, Phys. Rev. B **62**, 10891 (2000).

[78] J. Lefebvre, P. J. Poole, G. C. Aers, D. Chithrani, and R. L. Williams, J. Vac. Sci. Technol. B 20, 2173 (2002).

[79] Y. M. Qiu and D. Uhl, J. Cryst. Growth **257**, 225 (2003).

[80] J. Brault, M. Gendry, G. Grenet, G. Hollinger, Y. Desières, and T. Benyattou, Appl. Phys. Lett. **73,** *73*, 2932 (1998).

[81] V. M. Ustinov, E. R. Weber, S. Ruvimov, Z. Liliental-Weber, A. E. Zhukov, A. Yu. Egorov, A. R. Kovsh, A. F. Tsatsul'nikov, and P. S. Kop'ev, *Appl. Phys. Lett.* **72,** 362 (1998).

[82] C. Paranthoen, N. Bertu, O. Dehaese, A. Le Corre, S. Loualiche, B. Lambert, G. Patriarche, Appl. Phys. Lett. **78**, 1751 (2001).

[83] R. Beanland, Ultramicroscopy, **102**, 115-125 (2005).

[84] J. F. Chen, P. Y. Wang, J. S. Wang, C. Y. Tsai and N. C. Chen, *J. Appl. Phys.* **87**, 1369-1373 (2000).

[85] C. L. Jelen, Thesis (Ph.D.)--Northwestern University, 1998.

[86] J. Brault, M. Gendry, G. Grenet, G. Hollinger, Y. Desie`res and T. Benyattou, Appl. Phys. Lett. **73**, 2932 (1998).

[87] G. S. Solomon, J. A. Trezza, and J. S. Harris, Jr., Appl. Phys. Lett. **66**, 3161 (1995).

[88] V. A. Shchukin, D. Bimberg, Rev. Mod. Phys. **71,** 1125-1171 (1999).

[89] W. Zhang, H. Lim, M. Taguchi, S. Tsao, B. Movaghar, and M. Razeghi, Appl. Phys. Lett. **86**, 191103 (2005).

[90] J. Jiang, K. Mi, S. Tsao, W. Zhang, H. Lim, T. O'Sullivan, T. Sills, M. Razeghi, G. J. Brown, M. Z. Tidrow, Appl. Phys. Lett. **84**, 2232 (2004).

[91] S. Krishna, D. Forman, S. Annamalai, P. Dowd, P. Varangis, T. Tumolillo, A. Gray, J. Zilko, K. Sun, M. Liu, J. Campbell, D. Carothers, Appl. Phys. Lett. **86**, 193501 (2005).

[92] S. Tang, C. Chiang, P. Weng, Y. Gau, J. Luo, S. Yang, C. Shih, S. Lin, S. Lee, IEEE Photo. Technol. Lett. **18**, 986 (2006).

[93] B. F. Levine, J. Appl. Phys. **74**, R1-R81 (1993).

[94] S. D. Gunapala, S. V. Bandara, J. K. Liu, C. J. Hill, S. B. Rafol, J. M. Mumolo, J. T. Trinh, M. Z. Tidrow and P. D. LeVan, Semicond. Sci. Technol. **20**, 473-480 (2005)

[95] S. Krishna, J. Phys. D: Appl. Phys. **38,** 2142-2150 (2005).

[96] S. Y. Wang, S. D. Lin, H. W. Wu, and C. P. Lee, Appl. Phys. Lett. **78,** 1023 (2000).

[97] S. Tsao, H. Lim, W. Zhang, and M. Razeghi, Appl. Phys. Lett., 201109 (2007).

12 Appendix

12.1 Quantum dot energy level and wavefunction calculation under bias

```
/* to run the program, type gcc -c filename1.c */

/* gcc filename1.o -o filename2 -lgsl -lgslcblas -lm */

/* then execute with ./filename2 */

/* Be careful : divide the matrix par 10000 before using it */


#include <stdio.h>

#include <gsl/gsl_sf_bessel.h>

#include <gsl/gsl_integration.h>

#include <gsl/gsl_math.h>

#include <gsl/gsl_matrix.h>

#include <math.h>


/* GaInAs QD on GaInP barrier on GaAs substrate */

/* length unit is Bohr radius 0.529177A */

/* energy unit is Rydberg 13.6058 eV */

/* Ga_0.348In_0.652As lattice constant 5.917A  2ML   */

/* ---------- Parameters ---------- */

/* geometric parameters */
```

```
#define R_C 1511.78150        /* Radius of boundary cylinder 4*r_QD */
#define H_C 604.71264         /* height of boundary cylinder 8*h_QD */
#define h_OQD 0               /* distance of the QD from the center of the cylinder */
#define r_QD 377.94538        /* base radius of quantum dot 20nm */
#define h_QD 75.58908         /* height of quantum dot 4nm */
#define Radius_QD 982.65798   /* Radius_QD (r_QD*r_QD+h_QD*h_QD)/(2*h_QD) */
#define h_WL 8.38614          /* 1.5 ML GaInAs */

/* physical parameters */

#define m_B 0.11              /* effective mass of GaInP barrier */
#define m_W 0.05              /* effective mass of GaInAs quantum dot */
#define V_0 0.05144865        /* conduction band offset between GaInAs and GaInP 0.70eV */

/* calculation parameters */

#define N_l 10                /* number of sinus functions */
#define N_m 3                 /* number-1 of bessel functions */
#define N_n 10                /* number of zeros pro bessel function */

/* ---------- Functions for the calculation of the intergrands ---------- */
```

```
/* Z_rho(r) calculation of the height of the QD according to r */

double Z_rho(double r)
{
  return sqrt(Radius_QD*Radius_QD-r*r) - sqrt(Radius_QD*Radius_QD-r_QD*r_QD);
}

/* Radial function R_0(r,K,m) */

double R_0(double r,int m,double K)
{
  return gsl_sf_bessel_Jn(m,K*r);;
}

/* R_1(r,K,m) */

double R_1(double r,int m,double K)
{
  return gsl_sf_bessel_Jn(m-1,K*r) - gsl_sf_bessel_Jn(m+1,K*r);
}

/* function F_ll'H(z) with la=l and lb=l' */
```

```
double F_lalbH(double z,int la,int lb,double H)
{
  double a;
  if (la!=lb)
    a = 1/(M_PI*(la+lb)) * (sin((la+lb)*M_PI*(0.5-(z+H)/H_C)) - sin((la+lb)*M_PI*(0.5-
H/H_C)))
        - 1/(M_PI*(la-lb)) * (sin((la-lb)*M_PI*(0.5-(z+H)/H_C)) - sin((la-lb)*M_PI*(0.5-
H/H_C)));
  else
    a = 1/(M_PI*(la+lb)) * (sin((la+lb)*M_PI*(0.5-(z+H)/H_C)) - sin((la+lb)*M_PI*(0.5-
H/H_C)))
        + z/H_C;
  return a;
}

/* function G_ll'H(z) with la=l and lb=l' */

double G_lalbH(double z,int la,int lb,double H)
{
  double a;
  if (la!=lb)
```

```
    a = - 1/(M_PI*(la+lb)) * (sin((la+lb)*M_PI*(0.5-(z+H)/H_C)) - sin((la+lb)*M_PI*(0.5-
H/H_C)))
        - 1/(M_PI*(la-lb)) * (sin((la-lb)*M_PI*(0.5-(z+H)/H_C)) - sin((la-lb)*M_PI*(0.5-
H/H_C)));
  else
    a = - 1/(M_PI*(la+lb)) * (sin((la+lb)*M_PI*(0.5-(z+H)/H_C)) - sin((la+lb)*M_PI*(0.5-
H/H_C)))
        + z/H_C;
  return a;
}

/* Croneker function */

double Crodelta(int a,int b)
{
  double c;
  if(a==b)
    c=1.0;
  else
    c=0.0;
  return c;
}
```

```
/* ---------- Calculation of the intergrands ---------- */

/* structure of parameters for the integrands Blnl'n',mi */

struct I_params {int la;int lb;int m;int na;int nb;double Kmna;double Kmnb;double
Cmnanb;double F_WL;double G_WL;};

/* Integrand in QD */

double I_QD(double r,void *p)
{
  struct I_params *params=(struct I_params *)p;
  int la=(params->la);
  int lb=(params->lb);
  int m=(params->m);
  int na=(params->na);
  int nb=(params->nb);
  double Kmna=(params->Kmna);
  double Kmnb=(params->Kmnb);
  double Cmnanb=(params->Cmnanb);
  return -V_0*Cmnanb*r*R_0(r,m,Kmna)*R_0(r,m,Kmnb)*F_lalbH(Z_rho(r),la,lb,h_OQD)
```

```
        + (1/m_W-1/m_B)*Cmnanb *
(Kmna*Kmnb/4*r*R_1(r,m,Kmna)*R_1(r,m,Kmnb)*F_lalbH(Z_rho(r),la,lb,h_OQD)
        + m*m/r*R_0(r,m,Kmna)*R_0(r,m,Kmnb)*F_lalbH(Z_rho(r),la,lb,h_OQD)
        +
M_PI*M_PI*la*lb/(H_C*H_C)*r*R_0(r,m,Kmna)*R_0(r,m,Kmnb)*G_lalbH(Z_rho(r),la,lb,h_
OQD));
}

/* Integrand in WL */

double I_WL(double r,void *p)
{
  struct I_params *params=(struct I_params *)p;
  int la=(params->la);
  int lb=(params->lb);
  int m=(params->m);
  int na=(params->na);
  int nb=(params->nb);
  double Kmna=(params->Kmna);
  double Kmnb=(params->Kmnb);
  double Cmnanb=(params->Cmnanb);
  double F_WL=(params->F_WL);
```

```
  double G_WL=(params->G_WL);
  return (1/m_W-1/m_B)*Cmnanb *
(Kmna*Kmnb/4*F_WL*r*R_1(r,m,Kmna)*R_1(r,m,Kmnb)
        + m*m/r*R_0(r,m,Kmna)*R_0(r,m,Kmnb)*F_WL);
}

/* ---------- Function main ---------- */

int
main (void)
{
  char filename[13];    /* output filename */
  int e,m,la,lb,na,nb,n;
  double alphamna,alphamnb,Kmna,Kmnb,Jmna,Jmnb,Cmnanb,F_WL,G_WL,matrixelement;
  double alphamn[N_n];
  double result1,result2,result3,error1,error2;
  for(e=-10;e<11;e++)
  {
    /* constant electric field along the z-axis, in E5 Volt */
    E_el = e*0.2;
  for(m=0;m<N_m;m++)
  {
```

```
gsl_matrix *A_m;

int dim=N_l*N_n;

A_m = gsl_matrix_alloc(dim,dim);   /* create a matrix */


/* calculation of the alphamn */

for(n=1;n<N_n+1;n++)

{

  alphamn[n-1] = gsl_sf_bessel_zero_Jnu(m,n);

}

for(na=1;na<N_n+1;na++)

{

for(nb=1;nb<na+1;nb++)

{

  alphamna = alphamn[na-1];

  alphamnb = alphamn[nb-1];

  Kmna = alphamna/R_C;

  Kmnb = alphamnb/R_C;

  Jmna = gsl_sf_bessel_Jn(m+1,alphamna);

  Jmnb = gsl_sf_bessel_Jn(m+1,alphamnb);

  Cmnanb = 2/(R_C*R_C*Jmna*Jmnb);


  if (na==nb)
```

```
{
 for(la=1;la<N_l+1;la++)
 {
 for(lb=1;lb<la+1;lb++)
 {
  F_WL = F_lalbH(h_WL,la,lb,h_OQD-h_WL);
  G_WL = G_lalbH(h_WL,la,lb,h_OQD-h_WL);

  /* calculation of the intergrals */

  gsl_integration_workspace *w1=gsl_integration_workspace_alloc (1000);
  gsl_integration_workspace *w2=gsl_integration_workspace_alloc (1000);
  struct I_params params={la,lb,m,na,nb,Kmna,Kmnb,Cmnanb,F_WL,G_WL};

  gsl_function F1;
  F1.function = &I_QD;
  F1.params=&params;

  gsl_function F2;
  F2.function = &I_WL;
  F2.params=&params;
```

```
        gsl_integration_qag(&F1,0,r_QD,1e-10,1e-
10,1000,GSL_INTEG_GAUSS61,w1,&result1,&error1);
        gsl_integration_qag(&F2,0,R_C,1e-10,1e-
10,1000,GSL_INTEG_GAUSS61,w2,&result2,&error2);
        result3 = R_C*R_C/2*Jmna*Jmna;

        /* calculation of the matrix element Alnl'n',m */

matrixelement = 1/m_B * (Kmna*Kmna + (M_PI*M_PI*la*la)/(H_C*H_C)) * Crodelta(la,lb)
                + result1
                + result2
                - V_0*Cmnanb*F_WL*result3
                + (1/m_W-1/m_B)*M_PI*M_PI*la*lb/(H_C*H_C)*Cmnanb*G_WL*result3;

        /* bias */

        lalb = (la+lb)/2;
        lalb = la+lb - 2*lalb;
        if(lalb==1)
        {
          lad = la;
          lbd = lb;
```

```
          matrixelement = matrixelement
                        + 2*E_el*H_C/(M_PI*M_PI)*(1/((lad-lbd)*(lad-lbd)) -
1/((lad+lbd)*(lad+lbd)))
                        *0.529177/13.6058*0.00001;
        }
        /* matrixelement is multiplied by 10000 in order not to have inaccurate approximation
while displaying */

        matrixelement = matrixelement * 10000;

        /* construction of the symetric matrix */

        gsl_matrix_set(A_m,N_l*(na-1)+(la-1),N_l*(nb-1)+(lb-1),matrixelement);
        gsl_matrix_set(A_m,N_l*(nb-1)+(lb-1),N_l*(na-1)+(la-1),matrixelement);

        /* release memory */

        gsl_integration_workspace_free(w1);
        gsl_integration_workspace_free(w2);
      }
      }
    }
```

```
else
{
 for(la=1;la<N_l+1;la++)
 {
 for(lb=1;lb<N_l+1;lb++)
 {
  F_WL = F_lalbH(h_WL,la,lb,h_OQD-h_WL);
  G_WL = G_lalbH(h_WL,la,lb,h_OQD-h_WL);

  /* calculation of the intergrals */

  gsl_integration_workspace *w1=gsl_integration_workspace_alloc (1000);
  gsl_integration_workspace *w2=gsl_integration_workspace_alloc (1000);

  struct I_params params={la,lb,m,na,nb,Kmna,Kmnb,Cmnanb,F_WL,G_WL};

  gsl_function F1;
  F1.function = &I_QD;
  F1.params=&params;

  gsl_function F2;
```

```
F2.function = &I_WL;
F2.params=&params;

gsl_integration_qag(&F1,0,r_QD,1e-10,1e-
10,1000,GSL_INTEG_GAUSS61,w1,&result1,&error1);
gsl_integration_qag(&F2,0,R_C,1e-10,1e-
10,1000,GSL_INTEG_GAUSS61,w2,&result2,&error2);

/* calculation of the matrix element Alnl'n',m */

matrixelement = result1 + result2;

/* matrixelement is multiplied by 10000 in order not to have inaccurate approximation
while displaying */

matrixelement = matrixelement * 10000;

/* construction of the symetric matrix */

gsl_matrix_set(A_m,N_l*(na-1)+(la-1),N_l*(nb-1)+(lb-1),matrixelement);
gsl_matrix_set(A_m,N_l*(nb-1)+(lb-1),N_l*(na-1)+(la-1),matrixelement);
```

```
      /* release memory */

      gsl_integration_workspace_free(w1);
      gsl_integration_workspace_free(w2);
    }
    }
  }
 }
 }

 /* print matrix the easy way */

 printf("e=%d Matrix m=%d\n",e,m);
 sprintf(filename,"m_e%d_m%d.dat",e,m);
 FILE *s=fopen(filename,"wb");
 gsl_matrix_fprintf(s,A_m,"%f");
 fclose(s);

 /* release memory */

 gsl_matrix_free(A_m);
}
```

```
  }
}
```

12.2 Double quantum dot energy level and wavefunction calculation under bias

```
/* to run the program, type gcc -c filename1.c */
/* gcc filename1.o -o filename2 -lgsl -lgslcblas -lm */
/* then execute with ./filename2 */

#include <stdio.h>
#include <gsl/gsl_sf_bessel.h>
#include <gsl/gsl_integration.h>
#include <gsl/gsl_math.h>
#include <gsl/gsl_matrix.h>
#include <math.h>

/* GaInAs QD on GaInP barrier on GaAs substrate */
/* length unit is Bohr radius 0.529177A */
/* energy unit is Rydberg 13.6058 eV */
/* Ga_0.348In_0.652As lattice constant 5.917A  2ML   */

/* ---------- Parameters ---------- */
```

```
/* geometric parameters */

#define R_C 1511.78150        /* Radius of boundary cylinder 4*r_QD */
#define H_C 302.35630         /* height of boundary cylinder 4*h_QD */
#define h_OQD 94.48634        /* distance of the QD from the center of the cylinder */
#define r_QD 377.94538        /* base radius of quantum dot 20nm */
#define h_QD 75.58908         /* height of quantum dot 4nm */
#define Radius_QD 982.65798   /* Radius_QD (r_QD*r_QD+h_QD*h_QD)/(2*h_QD) */
#define h_WL 8.38614          /* 1.5 ML GaInAs */

/* physical parameters */

#define m_B 0.11              /* effective mass of GaInP barrier */
#define m_W 0.05              /* effective mass of GaInAs quantum dot */
#define V_0 0.05144865        /* conduction band offset between GaInAs and GaInP 0.70eV */
#define E_el 0                /* constant electric field along the z axis, in E5 Volt */

/* calculation parameters */

#define N_l 10                /* number of sinus functions */
#define N_m 1                 /* number of bessel functions */
```

```
#define N_n 10                /* number of zeros pro bessel function */

/* ---------- Functions for the calculation of the intergrands ---------- */

/* Z_rho(r) calculation of the height of the QD according to r */

double Z_rho(double r)
{
  return sqrt(Radius_QD*Radius_QD-r*r) - sqrt(Radius_QD*Radius_QD-r_QD*r_QD);
}

/* Radial function R_0(r,m,K) */

double R_0(double r,int m,double K)
{
  return gsl_sf_bessel_Jn(m,K*r);;
}

/* R_1(r,m,K) */

double R_1(double r,int m,double K)
{
```

```
  return gsl_sf_bessel_Jn(m-1,K*r) - gsl_sf_bessel_Jn(m+1,K*r);
}
/* function F_ll'H(z) with la=l and lb=l' */
double F_lalbH(double z,int la,int lb,double H)
{
  double a;
  if (la!=lb)
    a = 1/(M_PI*(la+lb)) * (sin((la+lb)*M_PI*(0.5-(z+H)/H_C)) - sin((la+lb)*M_PI*(0.5-
H/H_C)))
        - 1/(M_PI*(la-lb)) * (sin((la-lb)*M_PI*(0.5-(z+H)/H_C)) - sin((la-lb)*M_PI*(0.5-
H/H_C)));
  else
    a = 1/(M_PI*(la+lb)) * (sin((la+lb)*M_PI*(0.5-(z+H)/H_C)) - sin((la+lb)*M_PI*(0.5-
H/H_C)))
        + z/H_C;
  return a;
}
/* function G_ll'H(z) with la=l and lb=l' */
double G_lalbH(double z,int la,int lb,double H)
{
  double a;
  if (la!=lb)
```

```
    a = - 1/(M_PI*(la+lb)) * (sin((la+lb)*M_PI*(0.5-(z+H)/H_C)) - sin((la+lb)*M_PI*(0.5-
H/H_C)))
        - 1/(M_PI*(la-lb)) * (sin((la-lb)*M_PI*(0.5-(z+H)/H_C)) - sin((la-lb)*M_PI*(0.5-
H/H_C)));
  else
    a = - 1/(M_PI*(la+lb)) * (sin((la+lb)*M_PI*(0.5-(z+H)/H_C)) - sin((la+lb)*M_PI*(0.5-
H/H_C)))
        + z/H_C;
  return a;
}
/* Croneker function */
double Crodelta(int a,int b)
{
  double c;
  if(a==b)
    c=1.0;
  else
    c=0.0;
  return c;
}

/* ---------- Calculation of the intergrands ---------- */
```

```
/* structure of parameters for the integrands Blnl'n',mi */

struct I_params {int la;int lb;int m;int na;int nb;double Kmna;double Kmnb;double
Cmnanb;double F_WL1;double F_WL2;double G_WL1;double G_WL2;};

/* Integrand in QD */
double I_QD(double r,void *p)
{
  struct I_params *params=(struct I_params *)p;
  int la=(params->la);
  int lb=(params->lb);
  int m=(params->m);
  int na=(params->na);
  int nb=(params->nb);
  double Kmna=(params->Kmna);
  double Kmnb=(params->Kmnb);
  double Cmnanb=(params->Cmnanb);
  return -V_0*Cmnanb*r*R_0(r,m,Kmna)*R_0(r,m,Kmnb)*(F_lalbH(Z_rho(r),la,lb,-
h_OQD)+F_lalbH(Z_rho(r),la,lb,h_OQD))
        + (1/m_W-1/m_B)*Cmnanb *
(Kmna*Kmnb/4*r*R_1(r,m,Kmna)*R_1(r,m,Kmnb)*(F_lalbH(Z_rho(r),la,lb,-
h_OQD)+F_lalbH(Z_rho(r),la,lb,h_OQD))
```

```
        + m*m/r*R_0(r,m,Kmna)*R_0(r,m,Kmnb)*(F_lalbH(Z_rho(r),la,lb,-
h_OQD)+F_lalbH(Z_rho(r),la,lb,h_OQD))
        +
M_PI*M_PI*la*lb/(H_C*H_C)*r*R_0(r,m,Kmna)*R_0(r,m,Kmnb)*(G_lalbH(Z_rho(r),la,lb,-
h_OQD)+G_lalbH(Z_rho(r),la,lb,h_OQD)));
}

/* Integrand in WL */
double I_WL(double r,void *p)
{
  struct I_params *params=(struct I_params *)p;
  int la=(params->la);
  int lb=(params->lb);
  int m=(params->m);
  int na=(params->na);
  int nb=(params->nb);
  double Kmna=(params->Kmna);
  double Kmnb=(params->Kmnb);
  double Cmnanb=(params->Cmnanb);
  double F_WL1=(params->F_WL1);
  double F_WL2=(params->F_WL2);
  double G_WL1=(params->G_WL1);
```

```
  double G_WL2=(params->G_WL2);

  return (1/m_W-1/m_B)*Cmnanb *
(Kmna*Kmnb/4*(F_WL1+F_WL2)*r*R_1(r,m,Kmna)*R_1(r,m,Kmnb)
        + m*m/r*R_0(r,m,Kmna)*R_0(r,m,Kmnb)*(F_WL1+F_WL2));
}

/* ---------- Function main ---------- */

int
main (void)
{
  char filename[20];    /* output filename */
  int m,la,lb,lalb,na,nb,n;
  double
lad,lbd,alphamna,alphamnb,Kmna,Kmnb,Jmna,Jmnb,Cmnanb,F_WL1,F_WL2,G_WL1,G_WL2,
matrixelement;
  double alphamn[N_n];
  double result1,result2,result3,error1,error2;

  for(m=0;m<N_m;m++)
  {
```

```
gsl_matrix *A_m;

int dim=N_l*N_n;

A_m = gsl_matrix_alloc(dim,dim);   /* create a matrix */


/* calculation of the alphamn */


for(n=1;n<N_n+1;n++)

{

  alphamn[n-1] = gsl_sf_bessel_zero_Jnu(m,n);

}


for(na=1;na<N_n+1;na++)

{

for(nb=1;nb<na+1;nb++)

{

  alphamna = alphamn[na-1];

  alphamnb = alphamn[nb-1];

  Kmna = alphamna/R_C;

  Kmnb = alphamnb/R_C;

  Jmna = gsl_sf_bessel_Jn(m+1,alphamna);

  Jmnb = gsl_sf_bessel_Jn(m+1,alphamnb);

  Cmnanb = 2/(R_C*R_C*Jmna*Jmnb);
```

```
if (na==nb)
{
 for(la=1;la<N_l+1;la++)
 {
 for(lb=1;lb<la+1;lb++)
 {
  F_WL1 = F_lalbH(h_WL,la,lb,-h_OQD-h_WL);
  F_WL2 = F_lalbH(h_WL,la,lb,h_OQD-h_WL);
  G_WL1 = G_lalbH(h_WL,la,lb,-h_OQD-h_WL);
  G_WL2 = G_lalbH(h_WL,la,lb,h_OQD-h_WL);

  /* calculation of the intergrals */

  gsl_integration_workspace *w1=gsl_integration_workspace_alloc (1000);
  gsl_integration_workspace *w2=gsl_integration_workspace_alloc (1000);

  struct I_params
params={la,lb,m,na,nb,Kmna,Kmnb,Cmnanb,F_WL1,F_WL2,G_WL1,G_WL2};

  gsl_function F1;
  F1.function = &I_QD;
```

```
        F1.params=&params;


        gsl_function F2;
        F2.function = &I_WL;
        F2.params=&params;


        gsl_integration_qag(&F1,0,r_QD,1e-10,1e-
10,1000,GSL_INTEG_GAUSS61,w1,&result1,&error1);
        gsl_integration_qag(&F2,0,R_C,1e-10,1e-
10,1000,GSL_INTEG_GAUSS61,w2,&result2,&error2);
        result3 = R_C*R_C/2*Jmna*Jmna;


        /* calculation of the matrix element Alnl'n',m */


        matrixelement = 1/m_B * (Kmna*Kmna + (M_PI*M_PI*la*la)/(H_C*H_C)) *
Crodelta(la,lb)
                        + result1
                        + result2
                        - V_0*Cmnanb*(F_WL1+F_WL2)*result3
                        + (1/m_W-
1/m_B)*M_PI*M_PI*la*lb/(H_C*H_C)*Cmnanb*(G_WL1+G_WL2)*result3;
```

```
        /* bias */

        lalb = (la+lb)/2;
        lalb = la+lb - 2*lalb;
        if(lalb==1)
        {
          lad = la;
          lbd = lb;
          matrixelement = matrixelement
                    + 2*E_el*H_C/(M_PI*M_PI)*(1/((lad-lbd)*(lad-lbd)) -
1/((lad+lbd)*(lad+lbd)))
                    *0.529177/13.6058*0.00001;
        }

        /* construction of the symetric matrix */

        gsl_matrix_set(A_m,N_l*(na-1)+(la-1),N_l*(nb-1)+(lb-1),matrixelement);
        gsl_matrix_set(A_m,N_l*(nb-1)+(lb-1),N_l*(na-1)+(la-1),matrixelement);

        /* release memory */

        gsl_integration_workspace_free(w1);
```

```
    gsl_integration_workspace_free(w2);
  }
  }
}

else
{
  for(la=1;la<N_l+1;la++)
  {
  for(lb=1;lb<N_l+1;lb++)
  {
    F_WL1 = F_lalbH(h_WL,la,lb,-h_OQD-h_WL);
    F_WL2 = F_lalbH(h_WL,la,lb,h_OQD-h_WL);
    G_WL1 = G_lalbH(h_WL,la,lb,-h_OQD-h_WL);
    G_WL2 = G_lalbH(h_WL,la,lb,h_OQD-h_WL);

    /* calculation of the intergrals */

    gsl_integration_workspace *w1=gsl_integration_workspace_alloc (1000);
    gsl_integration_workspace *w2=gsl_integration_workspace_alloc (1000);

    struct I_params params={la,lb,m,na,nb,Kmna,Kmnb,Cmnanb,F_WL,G_WL};
```

```
        gsl_function F1;
        F1.function = &I_QD;
        F1.params=&params;

        gsl_function F2;
        F2.function = &I_WL;
        F2.params=&params;

        gsl_integration_qag(&F1,0,r_QD,1e-10,1e-
10,1000,GSL_INTEG_GAUSS61,w1,&result1,&error1);
        gsl_integration_qag(&F2,0,R_C,1e-10,1e-
10,1000,GSL_INTEG_GAUSS61,w2,&result2,&error2);

        /* calculation of the matrix element Alnl'n',m */

        matrixelement = result1 + result2;

        /* construction of the symetric matrix */

        gsl_matrix_set(A_m,N_l*(na-1)+(la-1),N_l*(nb-1)+(lb-1),matrixelement);
        gsl_matrix_set(A_m,N_l*(nb-1)+(lb-1),N_l*(na-1)+(la-1),matrixelement);
```

```
      /* release memory */

      gsl_integration_workspace_free(w1);
      gsl_integration_workspace_free(w2);
    }
    }
  }
}
}

/* print matrix the easy way */

printf("Matrix m=%d\n",m);
sprintf(filename,"m_%d_GaInAs_GaInP.dat",m);
FILE *s=fopen(filename,"wb");
gsl_matrix_fprintf(s,A_m,"%f");
fclose(s);

/* release memory */

gsl_matrix_free(A_m);
```

```
  }
}
```

13 List of publications, conferences and awards

Publications

- S. Tsao, **H. Lim**, W. Zhang, and M. Razeghi, "High operating temperature 320 × 256 middle-wavelength infrared focal plane array imaging based on an InAs/InGaAs/InAlAs/ InP quantum dot infrared photodetector", Appl. Phys. Lett. 90, 201109 (2007).

- **H. Lim**, S. Tsao, W. Zhang, and M. Razeghi, "High-performance InAs quantum-dot infrared photodetectors grown on InP substrate operating at room temperature", Appl. Phys. Lett. 90, 131112 (2007).

- M. Razeghi, W. Zhang, **H. Lim**, S. Tsao, M. Taguchi and A. A. Quivy, "Infrared Imaging with Self-assembled In(Ga)As Quantum Dot Infrared Photodetectors", Proceedings of 25th Army Science Conference (2006).

- **H. Lim**, B. Movaghar, S. Tsao, M. Taguchi, W. Zhang, Alain Andre Quivy and Manijeh Razeghi, "Gain and recombination dynamics of quantum-dot infrared photodetectors", Physical Review B 74, 205321 (2006).

- M. Razeghi, **H. Lim**, S. Tsao, M. Taguchi, W. Zhang and A.A. Quivy, "High performance mid-wavelength quantum dot infrared photodetectors for focal plane arrays", *Proc. of SPIE*, Vol. 6297, 62970C (2006).
- **H. Lim**, S. Tsao, M. Taguchi, W. Zhang, A. A. Quivy, M. Razeghi, "Quantum Dots in GaInP/GaInAs/GaAs for Infrared Sensting", Advances in Science and Technology 51, 201 (2006).

- M. Razeghi, **Ho-Chul Lim**, S. Tsao, M. Taguchi, W. Zhang, and A.A. Quivy, "Quantum-dot infrared photodetectors and focal plane arrays", *Proc. of SPIE*, Vol. 6206, 62060I (2006).

- J. Szafraniec, S. Tsao, W. Zhang, **H. Lim**, M. Taguchi, A. A. Quivy, B. Movaghar, and M. Razeghi , "High-detectivity quantum-dot infrared photodetectors grown by metalorganic chemical-vapor deposition ", Appl. Phys. Lett. 88, 121102 (2006).

- **H. Lim**, S. Tsao, M. Taguchi, W. Zhang, A. Quivy and M. Razeghi, "InGaAs/InGaP Quantum-Dot Photodetector with a High Detectivity", *Proc. of SPIE*, Vol. 6127, 61270N (2006).

- W. Zhang, **H. Lim**, M. Taguchi, A. Quivy and M. Razeghi, "InAs quantum dot infrared photodetectors on InP by MOCVD", *Proc. of SPIE*, Vol. 6127, 61270M (2006).

- **H. Lim**, W. Zhang, S. Tsao, T. Sills, J. Szafraniec, K. Mi, B. Movaghar, and M. Razeghi, "Quantum Dot Photodetectors: Comparison Experiment and Theory", Phys. Rev. B **72**, 085332 (2005).

- M. Razeghi, W. Zhang, **H. Lim**, S. Tsao, J. Szafraniec, M. Taguchi and B. Movaghar, "Focal plane arrays based on quantum dot infrared photodetectors", *Proc. of SPIE*, Vol. 5838, pp.125-136 (2005).

- W. Zhang, **H. Lim**, M. Taguchi, S. Tsao, B. Movaghar, and M. Razeghi, "High Detectivity InAs Quantum-Dot Infrared Photodetectors Grown on InP by Metalorganic Chemical Vapor Deposition", Appl. Phys. Lett. 86, 191103 (2005).

- S. Tsao, K. Mi, J. Szafraniec, W. Zhang, **H. Lim**, B. Movaghar, and M. Razeghi, "High performance InGaAs/InGaP quantum dot infrared photodetector achieved through doping level optimization", *Proc. of SPIE*, Vol. 5732, pp. 334-341 (2005).

- W. Zhang, **H. Lim**, M. Taguchi, S. Tsao, J. Szafraniec, B. Movaghar, M. Razeghi, and M. Tidrow, "High performance InAs quantum dot infrared photodetectors (QDIP) on InP by MOCVD", *Proc. of SPIE*, Vol. 5732, pp. 326-333 (2005).

- M. Razeghi, **H. Lim**, S. Tsao, J. Szafraniec, W. Zhang, K. Mi, and B. Movaghar, "Transport and Photodetection in Self-Assembled Semiconductor Quantum Dots," Nanotechnology, Vol. 16, pp. 219-229 (2005).

- M. Razeghi, W. Zhang, **H. Lim**, S. Tsao, J. Jiang, "Quantum dot infrared photodetectors (QDIPs) by MOCVD and QDIP focal plane array" (**Postdeadline paper**), 2004 Conference on Lasers and Electro-Optics/Internal Quantum Electronics conference (CLEO/IQEC), May 16-21, 2004, San Francisco, CA.

- J. Jiang, K. Mi, S. Tsao, W. Zhang, **H. Lim**, T.O'Sullivan, T. Sills, M. Razeghi, G.J. Brown, and M.Z. Tidrow, "Demonstration of a 256x256 Middle-Wavelength Infrared

Focal Plane Array based on InGaAs/InGaP Quantum Dot Infrared Photodetectors (QDIPs)", Appl. Phys. Lett. 84, 2232 (2004).

- J. Jiang, S. Tsao, T. O'Sullivan, W. Zhang, **H. Lim**, T. Sills, K. Mi, M. Razeghi, G.J. Brown, and M.Z. Tidrow, "High Detectivity InGaAs/InGaP Quantum-Dot Infrared Photodetectors Grown by Low Pressure Metalorganic Chemical Vapor Deposition", Appl. Phys. Lett. 84, 2166 (2004).

- Z. Jiang, **H. Lim**, and V. Chandrasekhar and J. Eom, "Local thermometry technique based on proximity-coupled superconductor/normal-metal/superconductor devices", Appl. Phys. Lett. 83, 2190 (2004).

Conferences

- "High performance InGaAs/InGaP quantum dot infrared photodetector achieved through doping level optimization", SPIE Conference, January 22-27, 2005, San Jose.

- "High performance InAs quantum dot infrared photodetectors (QDIP) on InP by MOCVD", SPIE Conference, January 22-27, 2005, San Jose, CA.

- "Thermal imaging based on High-Performance InAs/InP Quantum-Dot Infrared Photodetector Operating at High Temperature", IEEE LEOS 2007, October 21-25, 2007, Lake Buena Vista, FL.

Awards

- Best Paper award of Microelectronics and Photonics Technologies in 25th Army Science Conference (Nov. 2006).